Morphology Control of Polymer Composites for Enhanced Microwave Absorption

by

Avi Bregman

A dissertation submitted in partial fulfillment
of the requirements for the degree of
Doctor of Philosophy
(Materials Science and Engineering)
in the University of Michigan
2020

Doctoral Committee:

Professor Alan I. Taub, Chair
Assistant Professor John Heron
Professor Eric Michielssen
Professor Max Shtein

Avi Bregman

avibreg@umich.edu

ORCID iD: 0000-0002-8788-6566

DEDICATION

It truly takes a village to accomplish anything worthwhile.

To my family who supported me unconditionally,

To my friends who never stopped encouraging me,

To my colleagues who constantly inspire and challenge me

I cannot every repay your love and kindness.

ACKNOWLEDGEMENTS

For experimental assistance, I probably need to thank every single lab and grad student at the University of Michigan. I would like to start with

I must start by acknowledging the person who convinced me to stay in graduate school (for better or worse) when I was on the verge of leaving. Dr. Taub, I am beyond appreciative for the mentorship you have given me every step of the way through graduate school. When my first project didn't pan out, you took a chance on this wacky idea I proposed to you that eventually became my thesis. Even though we both had zero knowledge of the field starting out, your enthusiasm, encouragement and ability to keep my focused when results didn't pan out exactly as planned, were invaluable in keeping me motivated. Your research guidance, and ability to keep me motivated when all seemed lost have been pivotal in my development as a researcher.

I am also grateful to my committee—Prof. John Heron, Prof. Eric Michielssen, and Prof. Max Shtein—for their insight and direction. For the early work developing the computational methods and learning the field of EMI shielding, I am especially thankful to Dr. Michielssen for his patience and expertise. I would also like to thank Dr. Heron and Dr. Shtein for extensive use of their resources throughout my grad school career.

Any grad student would also be remiss if they did not acknowledge the incredible staff working behind the scenes to make the whole operation run smoothly. There is probably no way I could have made it as far as I did without the continued and always helpful assistance from Keith McIntyre and Tim Chambers. They never hesitated to help me with problems big, medium, small and sometimes unnecessary. I also need to acknowledge Tim for putting up with me through two semesters of working directly with me as a GSI. I would also like to thank Shelley Fellers, Debbie Reynolds, Patti Vogel, and Renee Hilgendorf for all the administrative support they gave day in and day out. (even when I didn't turn in packing slips for months on end)

Within the Taub Group, it is impossible to imagine my grad school career without my first mentor, forever starting flag football QB, and Queen Mondays partner in crime. Wesley Chapkin, whether you know it or not, you were a daily inspiration to me during the time we overlapped. You always had time to answer my questions, help me on Raman, and do the crossword with me. I am forever grateful for your mentorship and guidance in those early years that helped me become a better grad student and researcher. To my fellow 2016 draft class (Caleb Reese and Maya Nath), although you made the very poor decision of going to work on metals projects, it has been such a pleasure working with you. My only wish is that the department would have been on board with a three-way joint thesis presentation so we all could have left together. Thanks for being there for me and listening to me complain ad nauseum.

To the rest of the Taub group new and old – Erika Salem, Anshul Singhal, Anita Luong, Amy Langhorst, Kanat Anurakparadorn, Yipeng He, Daney Zhang, Aaron Gladstein, and Air Randy Cheng—I will miss you guys more than you know. There doesn't exist a better lab group in the department NAY THE ENTIRE UNIVERISTY! TGFE.

Lastly, I need to acknowledge the people I have met while at the University of Michigan. From my very first day in Ann Arbor, I have constantly been surrounded by people that are the best of what humanity has to offer. To my official and unofficial roommates (looking at you Nym and Wendy), all the people I have shared miles with, the guys I spent probably too many hours hanging out in Zach's attic with, and the hundreds IM teams I played with in pursuit of an almost ethereal championship, I am indebted to you for the memories, experiences, and moments that will stay with me long after I leave Michigan.

TABLE OF CONTENTS

LIST OF FIGURES

LIST OF TABLES

LIST OF ACRONYMS AND SYMBOLS

AA = ascorbic acid

ABS = acrylonitrile butadiene styrene

AIBN = azobisisobutyronitrile

BM3D = black magic 3D

CB = carbon black

CF = cobalt ferrite

CNC = computer numeric control

CNF = carbon nanofiber

CNT = carbon nanotube

CPC = conductive polymer composite

DLP = digital light processing

EM = electromagnetic

EMI = electromagnetic interference

FEM = finite element modeling

FFF = fused filament fabrication

FTIR = Fourier transform infrared spectroscopy

GHz = gigahertz

GO = graphene oxide

HCL = hydrochloric acid

MWCNT = multiwall carbon nanotube

NRW = Nicolas-ross weir

P_0 = transmitted EM wave intensity

P_i = incident EM wave intensity

PANI = polyaniline

PC = polycarbonate

PCL = Polycaprolactone

PDMS = Polydimethylsiloxane

PEI = Polyetherimide

PEC = perfect electrical conductor

PLA = polylactic acid

PML = perfectly matched layer

PMMA = polymethyl methacrylate

PS = polystyrene

PU = polyurethane

PVP = poly (vinyl pyrrolidone)

rGO = reduced graphene oxide

RL = reflection loss (Eq 1.3)

SE = shielding efficiency (Eq 1.1)

SE_T = total shielding efficiency

SEM = scanning electron microscopy

TE = transverse electric

TM = transverse magnetic

UV = ultraviolet

XPS = x-ray photoelectron spectroscopy

XRD = x-ray diffraction

VNA = vector network analyzer

VSM = vibrating sample magnetometer

xGNP = graphene nanoplatelets

Z_{in} = characteristic material impedance (Eq 1.4)

ε’ = real permittivity

ε” = imaginary permittivity

ε_r = relative permittivity

θ = angle of incidence

σ = conductivity (Eq 3.1)

μ’ = real permeability

μ” = imaginary permeability

μ_r = relative permeability

ABSTRACT

As the number, use, and interconnectivity of wireless devices grows, the ever-present problem of electromagnetic interference (EMI) has grown exponentially. EMI can interrupt with normal device performance and degrade the quality of functions such as taking and receiving phone calls. Ordinarily, metal coatings, tapes, or plates are used to mitigate this problem due to their ability to reflect any incoming electro-magnetic (EM) radiation. However, reflection of incoming EM allows EMI to continue at neighboring devices or circuitry. To solve this problem, as well as concerns surrounding the weight, processability, and durability of metal EMI shields, researchers have turned to polymer composites as the next generation absorbing materials for EMI mitigation.

Polymer-conductive nanoparticle composite foams have shown promise as EMI absorbers due to the unique porous morphology that emerges during the foaming process. Inclusion of air in the material allows for higher degrees of EM penetration into the material where there are increased interactions with highly conductive cell walls and numerous air-filled pores. These two mechanisms lead to effective EM wave dissipation in a lightweight structure. The final morphology of the foamed material has a huge impact on the final shielding properties, but the relationship between foaming conditions and final morphology is highly variable and not easily predicted. This lack of predictive capability results in time and money intensive DOE material exploration.

Taking inspiration from polymer composite foams, we have developed a model guided approach to the manufacturing of polymer composite materials with periodic porous morphologies. This approach relies on using the material's intrinsic electromagnetic properties to perform geometric optimization in COMSOL. Simulations allow us to cut time and material costs in the development of new absorbers. Simulations also allow for the exploration of geometric parameters and configurations that are currently unachievable using modern foaming

processes. Furthermore, this approach is material and processing agnostic meaning it can be applied to any material system and can be processed using the most appropriate technique for a given geometry.

The viability of this approach was confirmed using a commercially available conductive nano-filled polymer composite 3D printing filament (Black Magic 3D) as well as a model system from literature composed of Graphene/Iron Oxide Nanoparticles. Using a modeled system containing a representative slab with measured or literature derived electromagnetic parameters, we introduced a single cubic/spherical pore and simulated the effect on reflection loss (RL). For highly conductive Black Magic 3D filament, there was minimal improvement in RL. For literature derived Graphene/Iron Oxide, a dramatic improvement in RL from -23 dB to -35 dB was observed for a spherical pore with a volume of 8.18 mm3. Initial results suggest that the addition of periodically placed air-filled pores within a conductive polymer composite can lead to lower reflection loss and higher absorption bandwidths.

In order to move forward with our simulation guided approach as an effective method for EMI shield development, it was necessary to experimentally validate our model. We did this using a poly-lactic acid/graphene nanoplatelet (PLA/xGNP) system. We fabricated solid plaques using ultrasonication followed by compression molding and used the measured electromagnetic parameters to simulate the shielding efficiency of PLA/xGNP modified with cylindrical pores of varying height. We used compression molding followed by CNC milling to fabricate PLA/xGNP with cylindrical pores and measured their shielding efficiency. We found agreement in the trends as well as location of maxima/minima between the experimentally measured data and simulated data. The validation of a model guided approach with experimental data opens the door for a more robust optimization of geometric parameters in porous EMI shields.

In addition to looking at the EMI shielding properties of an xGNP/PLA system, we also studied the EMI shielding properties of a polystyrene (PS)/reduced graphene oxide (rGO) system. Hot pressing of these materials leads to a segregated polymer composite structure with rGO fillers in the interfaces surrounding polystyrene domains. This can significantly lower the

percolation threshold as compared to the xGNP/PLA system and can help avoid problems associated with obtaining a homogenous dispersion. We studied the effect of rGO loading on the electromagnetic and EMI shielding properties of these materials. As the rGO volume fraction increased, there was a general increase in the shielding efficiency. We also studied the properties of PS/rGO structures functionalized with cobalt ferrite (CF) nanoparticles and found that there was an increase in shielding efficiency for certain compositions of PS/rGO/CF.

CHAPTER 1

Motivation and Background

1.1 Electromagnetic Interference Shielding

With the advent of massive telecommunication networks and the expansive development of wireless electronics operating in the gigahertz (GHz) range, “electromagnetic pollution” has risen to unprecedented levels [1]. Electromagnetic interference (EMI) arises when intended or spurious electromagnetic (EM) signals radiated by electrical/electronic circuits disturb the normal operation of surrounding equipment [2,3]. EMI shields and related absorbing coatings have been in use since World War II in order to reduce the degree of interference [4]. While EMI can occur for several different applications, of import for many commercial and military spaces are frequencies in the GHz range that relate to communications and radar.

When an incident EM wave encounters the front face of an EMI shield, there can either be reflection, transmission, absorption, and multiple reflections of the incident wave as shown in Figure 1.1. The EMI shielding efficiency (SE), reported as reduction of transmitted wave power, includes the shielding effects due to absorption, reflection, and multiple reflections. Due to multiple reflections inside of a shielding material, there can also be aftereffects like secondary reflection and secondary transmission.

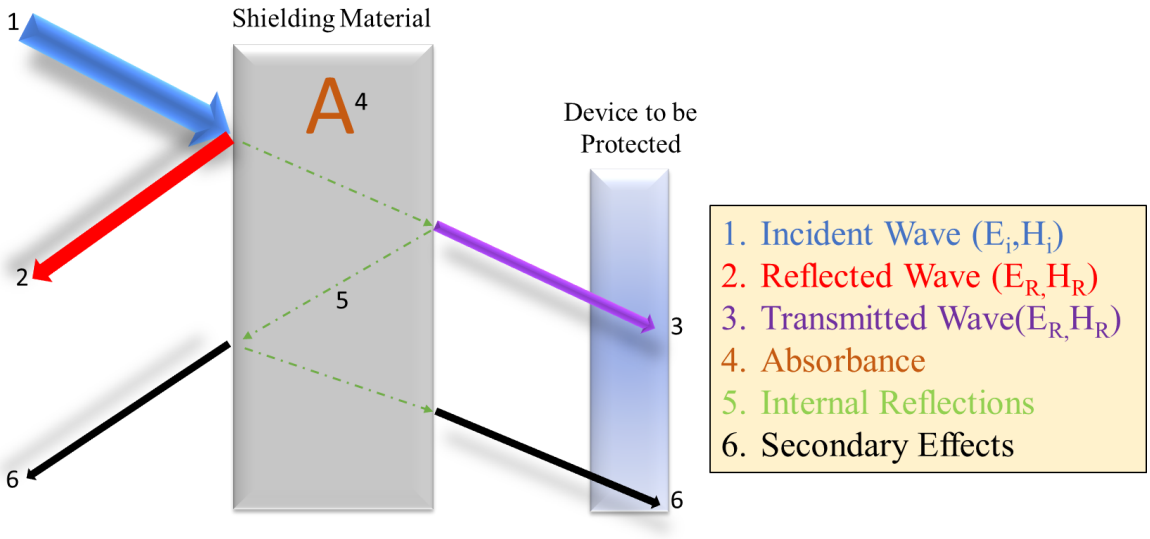

Fig 1.1 – Schematic depicting the outcomes of an incident electromagnetic (EM) wave upon interact with an EMI shielding material. The incident wave can be reflected, absorbed, transmitted through the shield, or be subject to secondary transmissions and reflections due to internal effects.

Depending on the application, the ability to stop EM transmission is referred to in two different ways. For certain applications, EMI shields are backed by air or another lossy material. In this case, the figure of merit is referred to simply as the SE and represents any power that is not transmitted through the shield.

For shielding materials, the SE can be written as:

(1.1) $SE = 10 \log \frac{P_i}{P_o}$

where P_i is the incident EM wave intensity and P_o is the intensity of the EM wave that penetrates through the material. The SE can be further broken down into the components of the wave that are reflected, absorbed, or subject to multiple reflections according to:

(1.2) $SE = SE_R + SE_A + SE_{MR}$

On the other hand, some applications require shielding materials to be placed on the surface of metal enclosures that behave like perfect electrical conductors (PEC). In this case, no EM power will transmit through the back of the shielding material and all reductions in incident power will come as a result of EM wave attenuation. This figure of merit is referred to as

reflection loss (RL). For these types of shields, we can us transmission line theory to write the RL as:

(1.3) $RL = 20log\left|\frac{Z_{in}-Z_0}{Z_{in}+Z_0}\right|$

Where Z_0 is the impedance of free space and Z_{in} is the characteristic impedance of the material defined by:

(1.4) $Z_{in} = Z_0\sqrt{\frac{\mu_r}{\varepsilon_r}}tanh\left\{i\left(\frac{2\pi f d}{c}\right)\sqrt{\mu_r\varepsilon_r}\right\}$

ε_r is the relative permittivity of the lossy material, μ_r is the relative permeability of the lossy material, *d* is the thickness of the lossy layer, *f* is the frequency of the incident EM wave, and *c* is the speed of light.

While they are used in different applications, RL and SE are both measured in decibels. For commercial applications a SE/RL of greater than 20 dB is needed and for military applications a SE/RL of greater than 30 dB is required [5]. The 20 dB cutoff is the level considered acceptable for human safety, and is the common threshold for commercial application, but military applications can require much higher thresholds due to the sensitive nature of the devices being protected [6].

Currently, the easiest way to protect devices and circuitry is to surround them with a metal barrier such as solid metals and wire meshes, metal-coated carbon fiber, metal-coated cloth, and metal-based coatings [7,8]. These mostly metallic materials exhibit very high shielding efficiencies and can meet most of the needs required for many applications. This high shielding efficiency comes as a result of the high reflectivity of metallic interfaces. However, EM waves do not exhibit large amounts of decay upon reflection; spurious waves that are not dissipated through absorption can continue to propagate and cause other problems in devices that are adjacent or otherwise. Combined with other issues such as poor wear and corrosion resistance, high rigidity, and non-uniform coating researchers have been exploring polymer composites (PC) for next generation EMI applications [9–12]. Bulk polymer materials are relatively inexpensive and can be easily processed but are mostly transparent to incoming EM waves.

1.2 Polymer Composites for EMI shielding

Composites refers to the combination of two or more materials to produce a new material with different properties. Polymer composites use polymer as the matrix while incorporating different kinds of fillers to improve the underlying matrix material. Polymer nanocomposites have been extensively studied for their unique mechanical [13–15], electrical [16–18], magnetic [19,20], and optical properties [21–23]. The small size, large surface area, of carbonaceous fillers such as carbon nanotubes (CNTs), carbon black (CB), carbon nanofibers, (CNF), graphene (G), and few-layered graphene nanoplatelets (GNPs) has been demonstrated to benefit the mechanical [24,25], thermal [26,27], and electrical/electromagnetic [28,29] properties of polymer composites.

For EMI shields, adding CNTs [30–32], CNFs [33], CB [34,35], and graphene [1,36,37] to polymer matrices has been shown to be an effective way to produce easily processible, low density, conductive polymer composite shields. These carbonaceous fillers have also demonstrated unique EMI shielding abilities owing to their ability to form conductive networks within the polymer matrix. In addition to advanced filler materials, researchers have also looked at the effect of using conductive polymers like PANI [38], PPy [39], or polyacetylene [40] as the matrix material. There are disagreements in the literature regarding the ideal composition for a conductive polymer composite for EMI shielding since it depends heavily on several factors including filler morphology, filler size, filler-matrix interactions, quality of filler dispersion, etc. In general, however, there is an increase in EMI SE with an increase in polymer composite conductivity due to increased loading.

Conductive polymer composites with carbonaceous fillers have demonstrated the ability to act as competent EMI shields for a variety of application as shown in Figure 1.2. Al- Saleh et al [36]. ran a comparative study that illustrated effective EMI shielding of up to 50 dB over the entire X-Band for a CNT/ Acrylonitrile butadiene styrene (ABS) composite. They also showed that ABS composites with similar loadings of CF and CB did not perform as well owing to lower aspect ratio. Song et al. demonstrated the effectiveness of ultra-thin EMI shields through the production of a 0.1mm thick graphene paper capable of achieving shielding efficiency of up to 46 dB [41].

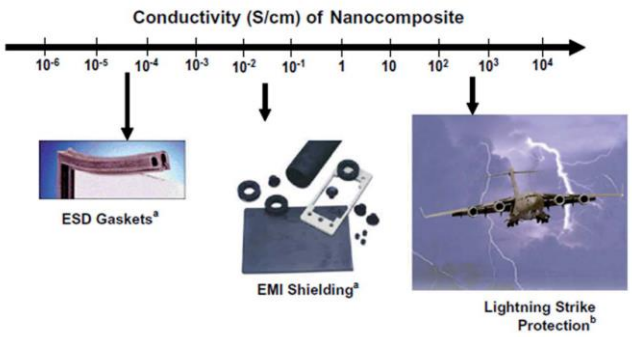

Fig 1.2 – Schematic illustrating the different application spaces for EMI shielding based on the conductivity of the nanocomposite material. High conductivity is needed for extreme applications like protection from lightning strikes, while lower conductivity is needed for static electrical discharge.

This research also demonstrated the ability to form Fabry-Pèrot cavity resonators by fabricating double-layered, symmetric structures with a layer of wax between two sheets of graphene paper; this arrangement increased the number of multiple reflections and constructive interference events leading to higher levels of EM absorption. Chizari et al. compared compression molding to 3D printing of conductive CNT/PLA composites and found that 3D printed EMI shields had significantly higher specific EMI shielding efficiency (~70 dB. vs ~37 dB g^{-1} cm^3). Introduction of modularity into the design process demonstrates the ability to fully optimizes structures to maximize shielding properties.[42]

1.3 Conductive Polymer Nanocomposites with Magnetic Components

The development of conductive, percolating networks is essential to the performance of EMI shield materials, but increases in conductivity leads to SE properties like that of metal shields i.e. high reflection-based SE. In order to keep conductivity low, but increases the absorption properties of polymer composites, it can be necessary to add a magnetic component. According to Poynting's theorem, there is a directional energy flux density of an EM wave (Poynting vector) that is defined as the cross product of the magnetic field vector and the electric field vector [43]. This means that attenuation of EM waves requires not only electronic contribution, but magnetic as well. Polymer matrices as well as carbonaceous filler are generally non-magnetic and do not make any magnetic contribution to EM wave attenuation.

Additionally, in order to have high attenuation, there needs to be a large degree of EM wave penetration into the material itself; low reflection at the front-face is a result of agreement between the material input impedance and the impedance of air. This impedance match comes

about from having a μ_r and ε_r that are close in value. For most conductive polymer nanocomposites, μ_r and ε_r are out of balance leading to most EM waves being reflected at the front face. Without contributions from an added magnetic material, it becomes harder to manage impedance mismatch.

Different strategies have been employed for the incorporation of ferromagnetic components into polymer composites for EMI shielding [5,44–50]. In these composites, the ferromagnetic nanoparticles not only reduce the front face impedance mismatch, but also increase absorption of any incident EM wave. Enhanced absorption comes as a result of ferromagnetic resonance as determined by the anisotropy coefficient, damping parameter, saturation magnetization, and particle shape [51]. Furthermore, many of these properties are affected by moving from bulk material to nanoparticle sizes. For example, the damping parameter due to surface effects increases as the particle diameter decreases and can even increase as much as an order of magnitude as compared to bulk material.[52] In addition, surface anisotropy is also inversely dependent on the particle size, particularly at diameters below hundred nanometers.[53] Nanosized ferromagnetic inclusions are also important for microwave absorbers since at dimensions will below the skin depth of the composite, EM waves are fully able to penetrate the particle. This entire particle contribution can be significant for particularly high magnetic saturation ferrites.

Mural et al.[49] used magnetic nickel nanoparticles decorated onto the surface of graphene oxide sheets embedded in a polyethylene/poly(ethylene oxide) blend. By adding small amounts of MWCNT to enhance conductivity, a minimum reflection loss of -70 dB at 17.1 GHz was achieved for a 6mm thick shield. Song et al.[46] explore free-standing graphene-based hybrid papers decorated with iron oxide nanoparticles. These papers demonstrated a high conductivity (50 S/cm) as well as a SE of 21 dB at a thickness of 0.2 mm making them highly competitive with thicker graphene-hybrid systems. Song et al.[47] explored EMI shielding using a graphene oxide/iron oxide nanoparticle hybrid filler in a wax matrix. By controlling the relative ratio of iron oxide nanoparticles to graphene oxide in the filler material, overall concentration of the filler itself, and the thickness of the composite, they demonstrated the ability to tune the position and minimum of the reflection loss peak. As was mentioned earlier, multiple reflections in which EM waves reflect at multiple interfaces in shielding materials can make significant

contributions to overall shielding ability [54]. The incorporation of magnetically functionalized fillers has been employed in a variety of polymer composite forms for EMI attenuation including single layers [55], multilayers [56,57], and other unique heterostructures including foams [58,59]. Of these various forms, foams have consistently demonstrated high broadband EMI absorption.

1.4 Use of Polymer Composite Foams for EMI Shielding

Polymer composite foams, characterized by their density, cell size and wall thickness. They can be physically or chemically foamed to achieve open or closed microstructures [58,60–62]. Various methods for polymer composite foaming have been reported in the literature including thermally induced phase separation [63],[64], water vapor induced phase separation [65],[66], coating and etching [67], physical foaming using supercritical gas [68],[69], and chemical foaming [70,71]. The wide variety of foaming approaches can lead to materials with increased strength [72], large surface area improvements [73], and other interesting properties that can be applied to a wide variety of applications including tissue engineering scaffolding, [74] batteries [75], and thermal conductivity enhancement [76]. Foams have also found a large degree of success in the realm of EMI shielding.

Polymer composite foams can be thought of as metamaterials composed of a polymer matrix, filler material, and air-filled pores. The inclusion of air-filled pores has two important effects relating to EMI shielding. First, ultra-high porosity foams exhibit low permittivity ensuring penetration of most incident radiation due to decreases in the interfacial impedance gap as explained in section 1.3 [77].

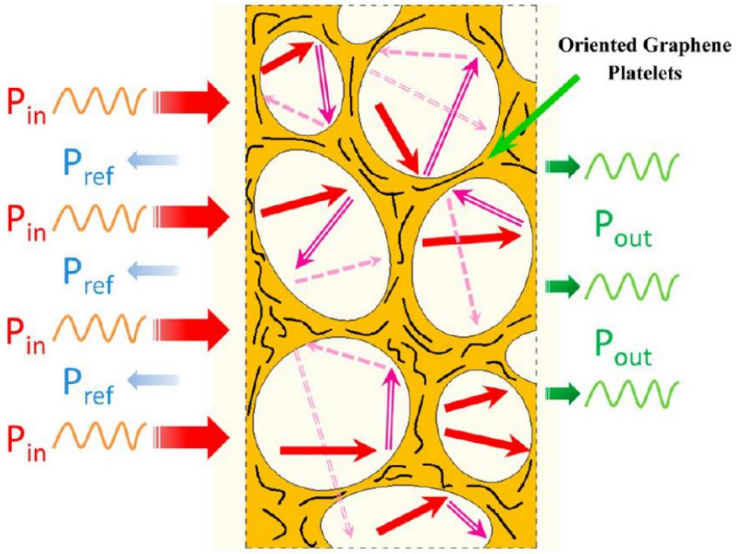

Fig 1.3 – Schematic description of microwave transfer across a PEI/graphene nanocomposite foam. Arrows inside of the pores are indicative of multiple scattering events that occur inside of the foam. Adapted from [65].

Second, upon penetration into the shielding material, the attenuation of EM waves is assisted by scattering between the cell walls and nanofillers as shown in Figure 1.3. Many scattering events makes it difficult for EM waves to escape before being dissipated as heat [65]. Table 1.1 illustrates the absorbing ability for a few different polymer composite foam systems. The absorbing power fraction is a clear indication that independent of the system, the primary shielding mechanism for polymer composites is absorption.

Table 1.1 EMI Shielding Abilities of Polymer Composite Foams

Polymer	Filler	Filler Content	SE_T (dB)	SE_A (Power Fraction)	Ref
PMMA	FLG	1.8 vol%	19	0.95	[68]
PS	MWCNT	7 wt%	20	0.18	[78]
PDMS	CDVG	0.8 wt%	23	0.83	[67]
PCL	MWCNT	0.25 vol%	60	0.87	[79]
PS	FGS	30 wt%	29	0.95	[80]
PEI	FLG	10 wt%	13	0.87	[65]

PMMA- poly (methyl methacrylate); PS – polystyrene; PDMS – polydimethylsiloxane; PCL – polycaprolactone; PEI – polyetherimide; FLG - few layer graphene; FGS – flaky graphene sheets

1.5 Limitations of Polymer Composite Foams for EMI Shielding

While polymer composite foams have high potential as ideal EMI shielding candidates, investigators have to undergo many experiments looking at how the final foam morphology is affected by changes in the foaming conditions (temp, time, pressure, blowing agent etc..) [81,82]. Gedler et al. found that the cell density could change by as much as three orders of magnitude depending on the foaming approach used for a 0.5 wt% GNP/PC composite foam. Soltani et al. performed extensive analysis on the impact on morphology of different foaming conditions for a PMMA/MWCNT composite and they found wide variation in the morphology depending on the foaming conditions used (Figure 1.4). For example, 5 wt% PMMA/MWCNT composites foamed with a depressurization rate of 1.16 bar/s at 80^{o}C were found to have an average cell size of 208.7 microns. By increasing the foaming temperature to 120^{o}C, and holding all other conditions constant, the average cell size grew to 320.8 um and the microporous network changed from closed to open.

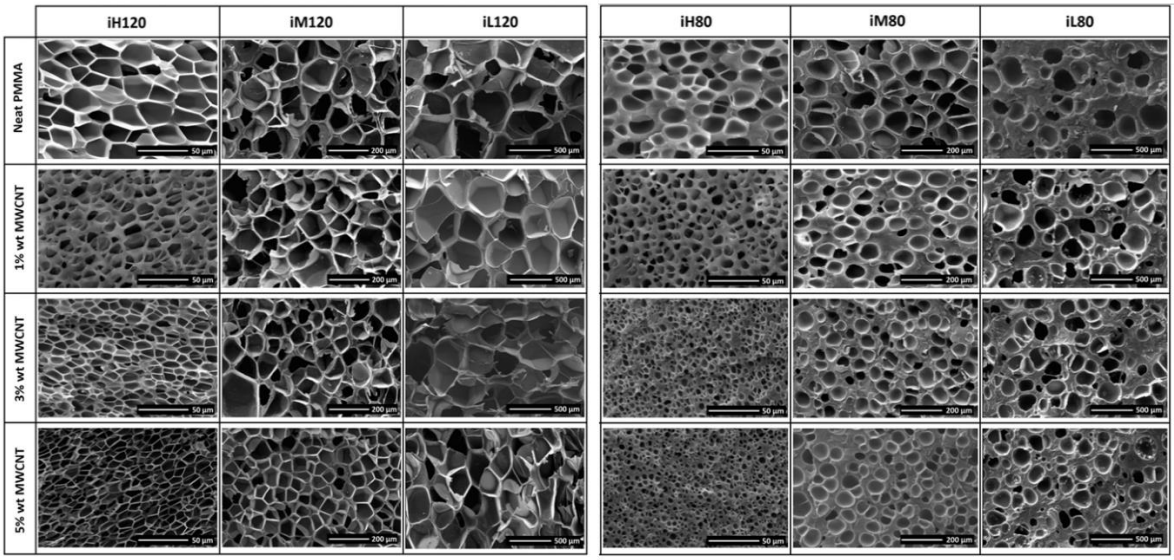

Fig 1.4 – Changes in morphology depending on the initial foaming conditions for PMMA/MWCNT composites. Different loadings of MWCNT are shown along the y axis. H, M, and L represent different foaming pressures and 120/80 represent the different foaming temperatures. Adapted from [83].

These changes in the final morphology can dramatically affect the final shielding properties of these composites. For instance, the transmitted power fraction nearly doubled when the foam temperature was changed from 80 ^{o}C to 120 ^{o}C for the 3 wt% PMMA/MWCNT composites shown in Fig 1.4. Even if the foaming conditions are kept constant, the type and

amount of filler can affect the final morphology. For instance, it was observed that variations in the ratio between GNP and MWCNT in a 3 wt% PMMA/GNP/MWCNT composite foam could change the difference in SE from 6 dB to as much as 36 dB [84].

1.6 Thesis Overview

As illustrated in chapter 1, there are many options when it comes to EMI shielding, depending on the application, however, there are currently limits to the application space as it pertains to cost and material performance. Figure 1.5 shows a schematic indicating the absorbance/gram of material vs. the potential cost of fabrication. Metal-based shields are the cheapest option but are limited in their ability to absorb incident EM radiation. Solid polymer composites and polymer composite foams display higher absorbances/g and have higher costs depending on the material/technique used. Although there are a small number of examples in literature for 3D printed EMI shields, they also have potential as absorbing materials.

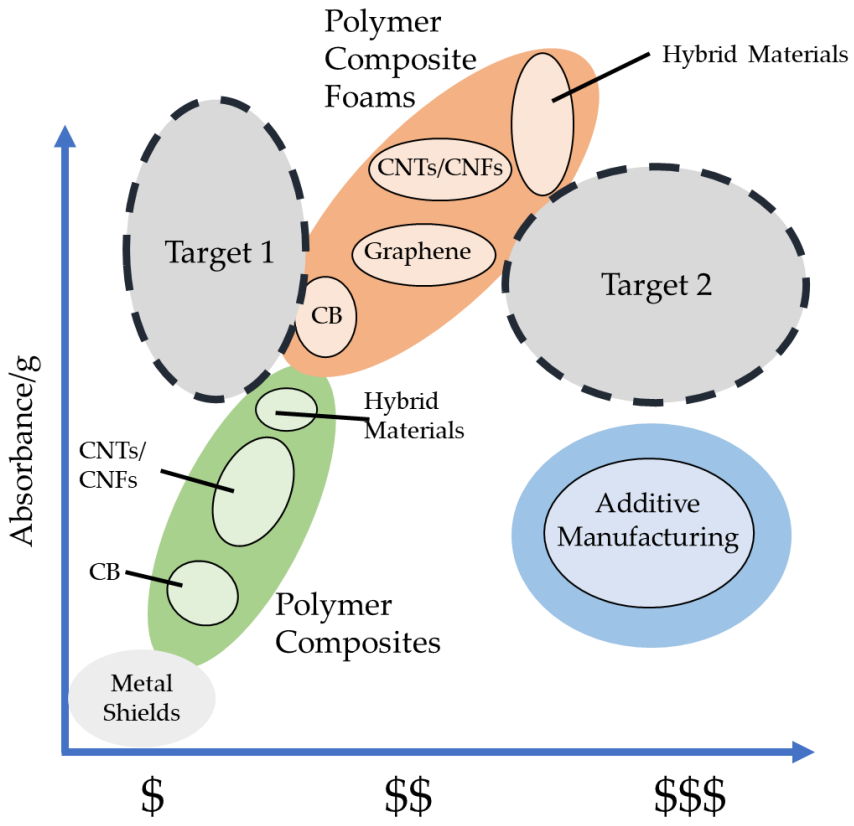

Fig 1.5 – Schematic displaying the absorbance/gram of material vs. potential cost separated by the fabrication technique. The target 1 and target 2 areas indicate movement towards higher performing EMI absorbers proposed in this thesis.

Overall, the proposed study intends to investigate the potential for polymer composites with periodic porous morphologies for EMI shielding. Additionally, we study a new material for microwave absorption with tunable electromagnetic properties in the context of our modeling approach. Through development and validation of a computational model, a more accurate understanding of how periodic morphologies affect overall shielding and absorption can be developed. This approach can help researchers optimize and speed up their design of microwave absorbers by eliminating trial-and-error approaches that consume time and money. We posit that increases in absorption can decreases costs while improving absorbance as compared to foams and solid polymer composites (Target area 1 in Fig 1.5). Additionally, this approach can be adapted to additive manufacturing approaches that will still be expensive but will improve performance as compared to current materials (Target area 2 in Fig 1.5).

In Chapter 2, the prospect of using periodically arranged pores as a proxy for foamed polymer composite EMI shields is introduced. This idea is studied in the context of a commercially available 3D printing filament as well as in the context of a microwave absorbing material from literature. Preliminary parametric studies reveal that the geometry of the pore as well as the size of the cell walls can have dramatic effects on the RL of microwave absorbing materials. In Chapter 3, a workflow for periodic porous EMI shields is developed and successfully validated for a series of xGNP/PLA composites containing cylindrical pores. The effects of xGNP aspect ratio on dielectric properties and EMI shielding properties is also explored. In Chapter 4, a novel absorber based on segregated structure polymer composites is developed and characterized. PS/rGO composites with and without CF nanoparticle functionalization are explored as potential microwave absorbers. These materials are also studied using the workflow described in Chapter 3 to look at the effects of geometric modification on their shielding properties. A summary of the contributions of this thesis as well as ongoing work and potential future directions are laid out in Chapter 5.

CHAPTER 2

Enhancement of Reflection Loss in Polymer Nanocomposites Through The Addition Of Periodically Placed Pores

2.1 Chapter Synopsis

A foam-inspired approach to polymer composite EMI shields has been developed. Research involving polymer composite foams has been limited due to difficulties in modeling and reported as the results of an empirical design of experiments [81,85–87]. An alternate approach utilizing the measurement of intrinsic complex electromagnetic parameters and, predictive modeling of absorbing periodic geometries in the COMSOL environment is presented. The viability of this approach was confirmed using a commercially available conductive nano-filled polymer composite 3D printing filament as well as a model system from literature. Initial results suggest that the addition of periodically placed air-filled pores within a conductive polymer composite can lead to lower reflection loss and higher absorption bandwidths.

2.2 Introduction

An emerging approach to absorbance dominated EMI shielding is the use of conductive polymer composite foams. As compared to non-porous materials, foams exhibit lower density, lower percolation thresholds, and higher EMI shielding efficiency (SE) that is largely dominated by absorption [88–90]. The porous morphology decreases the impedance mismatch between air and the shield allowing a larger portion of the incident EM wave to penetrate into the shield where it can be absorbed and dissipated [91]. However, foamed polymer composites have shielding characteristics that are highly dependent on the morphology of the finished foam, which is in turn highly sensitive to the specific conditions of the foaming process [81,92]. Developing optimized polymer foam composites is a complex process that requires the screening

of many different factors including material compositions, foaming temperature, foaming time, and depressurization rate, to name a few.

To address concerns about the development of new foamed materials, we explore the introduction of pre-designed periodic pores into a conductive polymer nanocomposite matrix using finite element modeling (FEM). This chapter also addresses the material requirements needed in terms of complex permittivity and complex permeability to properly synergize with artificial pore structures.

2.3 Experimental

2.3.1 Materials

3D printed samples were produced using commercially available Black Magic 3D© (BM3D) filament, which is a polylactic acid (PLA) based filament that has been mixed with 16 wt% carbon-based particles. A commercial pure PLA filament purchased from 3DX Tech was used to print pure PLA samples. 3mm thick 3D printed samples were produced using a Maker M3 Fused Filament Fabrication (FFF) 3D printer. (extruder temperature: 220 ^{o}C; table heating 50 ^{o}C; speed 40 mm/s; extrusion multiplier 1.1).

2.3.2 VNA Measurement and Electromagnetic Property Extraction

Two-port scattering parameter measurements of BM3D and PLA plaques were performed over the X-band (8-12 GHz) using an Anritsu MS4644B vector network analyzer (VNA) at room temperature and normal pressure. Measurements were performed in a rectangular waveguide with frequency dependent angles of incidence for the TE_{10} mode as shown in Figure 2.1. Rectangular samples with dimensions of 22.86 mm x 10.16 mm x 3mm were filed down to ensure a tight fit between the sample and the waveguide holder since small air gaps can lead to error in measurement.

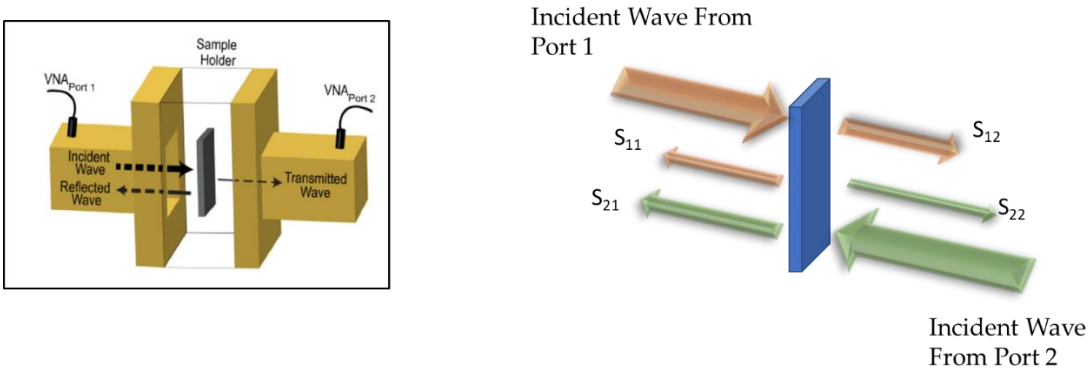

Fig 2.1 – The setup for VNA measurements includes a rectangular sample sandwiched between two rectangular waveguides (left). Based on incident waves from port 1 and port 2, the scattering parameter matrix can be extracted (right).

From scattering parameters, we can use the Nicolas-Ross Weir (NRW) method to extract the complex permittivity and complex permeability of our materials [93].

2.3.3 FEM Modeling With COMSOL

Finite Element Modeling was performed in COMSOL. The modeled geometry consists of a 3D periodic Cartesian lattice with a unit cell that contains arbitrarily shaped air-filled pores inside of a material with pre-defined frequency dependent electromagnetic parameters. COMSOL's Radio Frequency module is used to perform full field calculations of either a transverse electric (TE) or transverse magnetic (TM) incident wave that excites the structure from the top from a predefined angle of incidence (θ) (see Port 1 in Figure 2.1). Mesh refinement is used to maintain a minimum element quality of greater than 0.2 to ensure accurate results. The structure's S11, S12, and reflection loss (RL) are calculated over the X-Band with a sampling interval of 0.1 GHz. A characteristic unit cell is shown in Figure 2.2. The unit cell repeats periodically in the x-y plane and has finite thickness in the z-direction. The top of the cell is terminated by a perfectly matched layer (PML) to prevent secondary reflections, and the bottom of the cell is terminated either by a perfect electrically conducting (PEC) or a second port for study of non-PEC backed composites.

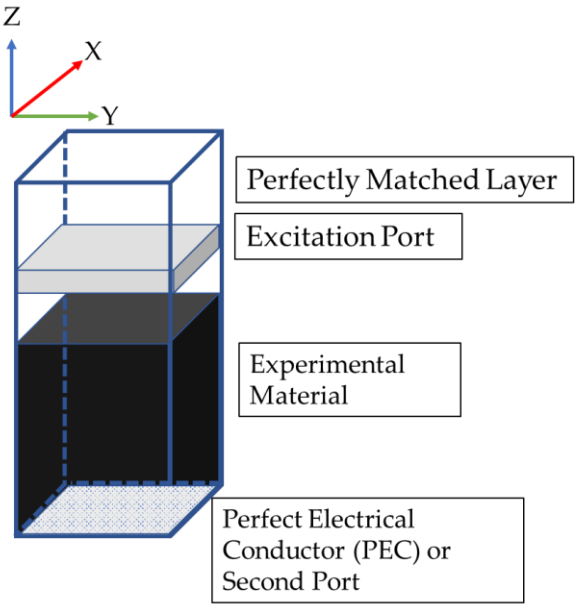

Fig 2.2 – Characteristic unit cell for simulations in COMSOL. The top of the cell is bounded by a perfectly matched layer (PML). The bottom of the cell is bounded with a perfect electrical conductor (PEC) for RL measurements and a second port for SE measurements. The unit cell is periodic in the X and Y directions and finite in the Z direction.

2.4 Results

To test our design methodology, we used commercially available BM3D and PLA filament. BM3D is a PLA based 3D filament that has a low bulk volume resistivity of 0.6 Ω.cm due to the addition of 16 wt% carbon content. As shown in Figure 2.3 the thermoplastic filament (A) contains a mixture of that graphene (B), carbon nanotubes (C), and carbon black (D). These images demonstrate a high degree of filler agglomeration this is expected due to high carbon content. This agglomeration leads to higher incidence of filler contact giving rise to a particularly low resistivity of 0.6 Ω cm. This agglomeration also contributes to poor mechanical properties as indicated by the brittleness of the filament. Agglomerated fillers also contribute to crack propagation and void formation.

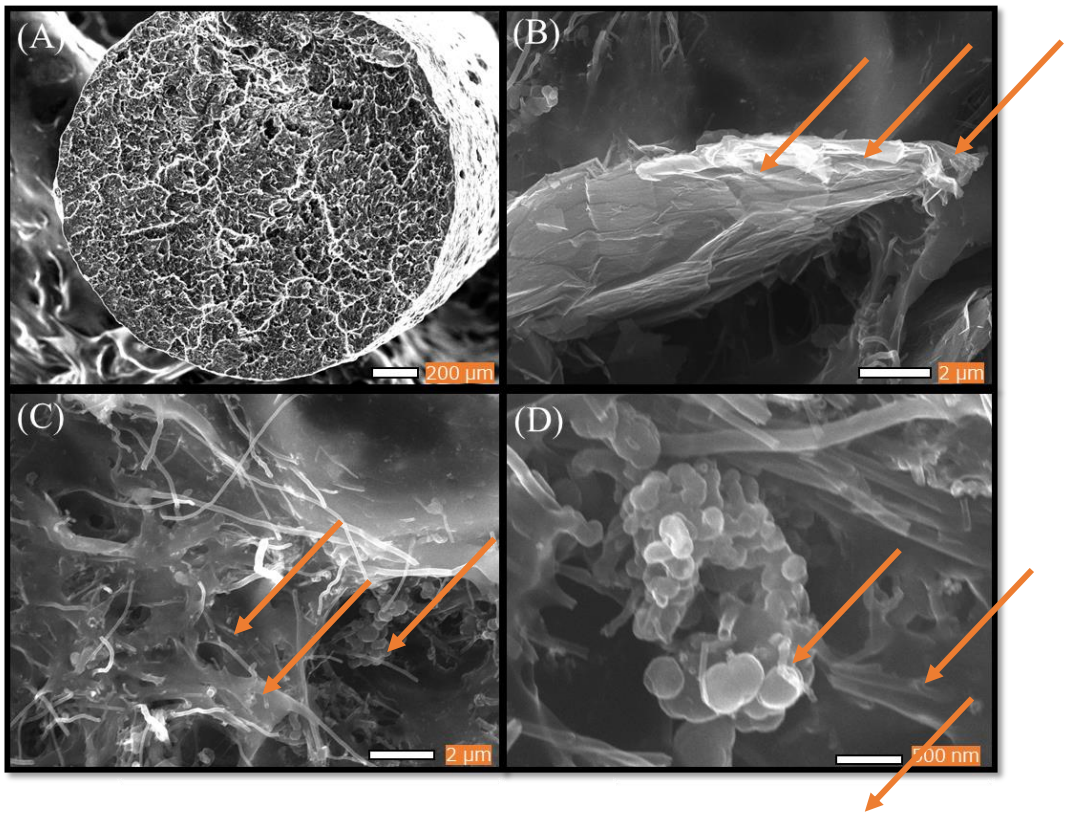

Fig 2.3 - SEM images of BM3D filament indicating the presence of carbonaceous filler. A cross section of the filament is shown in (A). Upon closer inspection, the filament is observed to contain graphene (B), carbon nanotubes (C) and carbon black (D).

Using a VNA, we measured the scattering parameters and extracted the complex permittivity and complex permeability using the NRW method. The results are shown in Figure 2.4.

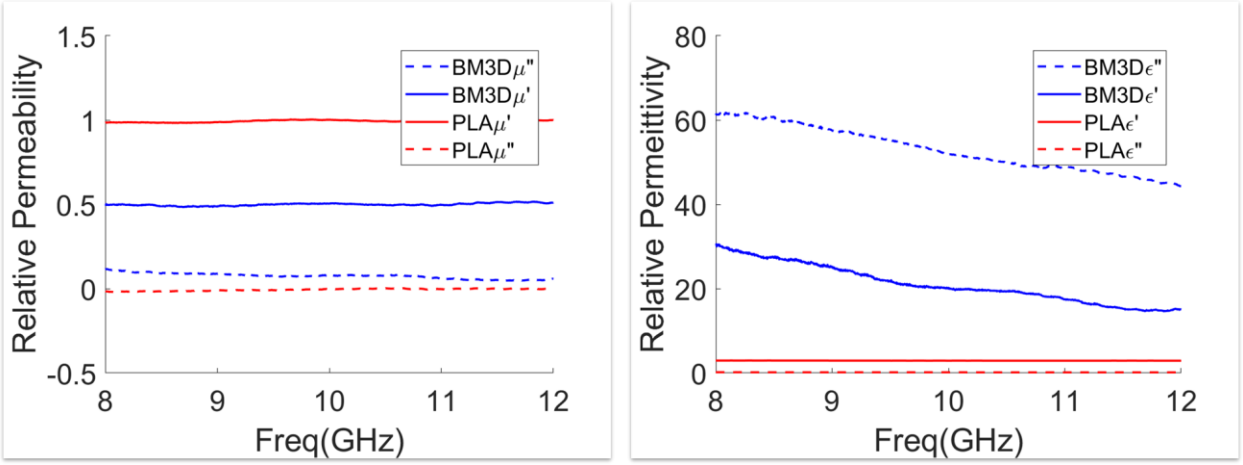

Fig 2.4 – The measured complex permittivity (left) and complex permeability (right) for BM3D and PLA using the NRW method.

The measured permittivity and permeability for PLA is in good agreement with literature values [94]. The complex permeability of PLA is what we would expect for a nonmagnetic material. The imaginary component of the permittivity, which correlates to dissipation of electrical energy within the polymer composite material, is high for BM3D. This indicates that there is a large amount of network formation within the material leading to high mobility of charge carriers and energy dissipation [95]. For BM3D, the real permeability lower than 1.0 can be attributed to the diamagnetic behavior of carbonaceous materials [96].

In foamed materials, much of the enhancement in shielding efficiency (SE) is attributed to the addition of porosity; the addition of pores reduces impedance mismatch with air and also increases the number of scattering events once the wave has penetrated into the bulk material [83]. However, the morphology of foams is highly sensitive to processing conditions. Furthermore, final foam morphologies cannot be predicted *a priori* and shielding properties are difficult to model due in part to the inhomogeneity of the foam morphology. Therefore, we use FEM simulations to predict the shielding properties of a homogenous metamaterial with a porous and periodic morphology using the extracted complex permittivity and permeability measurements.

Scattering parameter simulations are performed in COMSOL and final reflection loss (RL) is calculated according to equation 2.1.

(2.1) $RL = -20\log_{10}|S_{11}|$

Figure 2.5 depicts the change in RL upon addition of a single cubic pore to the center of a 3mm thick BM3D plaque and the effect of gradually increasing the pore volume. At normal incidence, the absorbing behavior of BM3D improves as the pore size increases. It is well known that dielectric mismatch causes reflection at interfaces, such as the one between BM3D and air. By modifying the morphology of our plaque by increasing the pore size, we are effectively decreasing the dielectric constant and making it closer to that of air. The introduction of the pore also increases the number of scattering events that can occur inside of the composite. This means that more incident microwave energy will be dissipated as heat. Because of its high conductivity, BM3D has limits as a material for absorption focused EMI shielding. Without a reduction in conductivity the impedance mismatch at the surface will still lead to reflection dominated shielding.

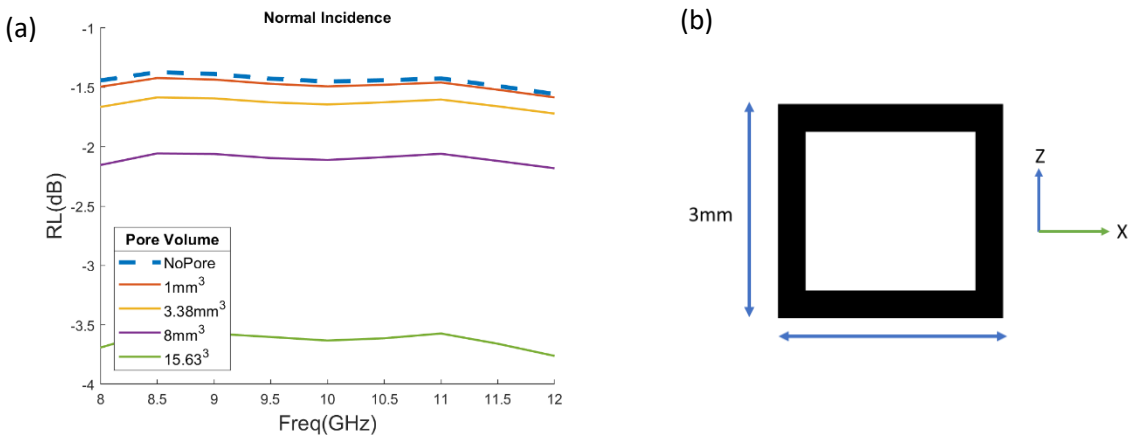

Fig 2.5 - Simulated change in RL at normal incidence of BM3D filament with a single cubic pore of changing volume (a). Cross-section indicating the placement of a cubic pore in a 3 mm thick samples (b).

For the design of an absorption dominated EMI shield, there are a few key material properties that need to be controlled such as the lowering of front face impedance mismatch, and the presence of dissipation pathways inside the material through the addition of magnetic or conductive fillers. The relative impedance of a material, Z, is given by equation 2.1 where μ_r and ε_r are the complex permeability and complex permittivity of the material.

$$(2.1)\ Z = \sqrt{\frac{\mu_r}{\varepsilon_r}}$$

For air, this value is 1. Materials that have relative impedances that are closer to 1 experience less front face reflection. To lower material impedance, one can use lower conductivity materials as well as the addition of magnetic components that increase the permeability. The addition of magnetic material can also increase the magnetic loss tangent, further contributing to the absorption of incident EM radiation.

To investigate the effect of simple geometric changes on RL for a low conductivity, magnetically enhanced material, we adapted literature values for the complex permittivity and permeability of a 30 wt% graphene/Fe_3O_4 paraffin wax composite [47]. Shown in Figure 2.6a and Figure 2.6b are the effects of adding either a cubic pore or a spherical pore to a 3mm thick composite layer. An unmodified 3mm thick sample achieves a minimum RL of -22.8 dB at 5.5 GHz. If we add a pore and isometrically change the pore volume, we see that the minimum RL not only decreases by as much as 13 dB, but the minimum peak shifts towards higher

frequencies. Additionally, as we add larger pores, the effective absorption bandwidth (RL ≤ 10 dB) increases from 2.4 to 6.3 GHz. The trend is similar for cubic and spherical pores.

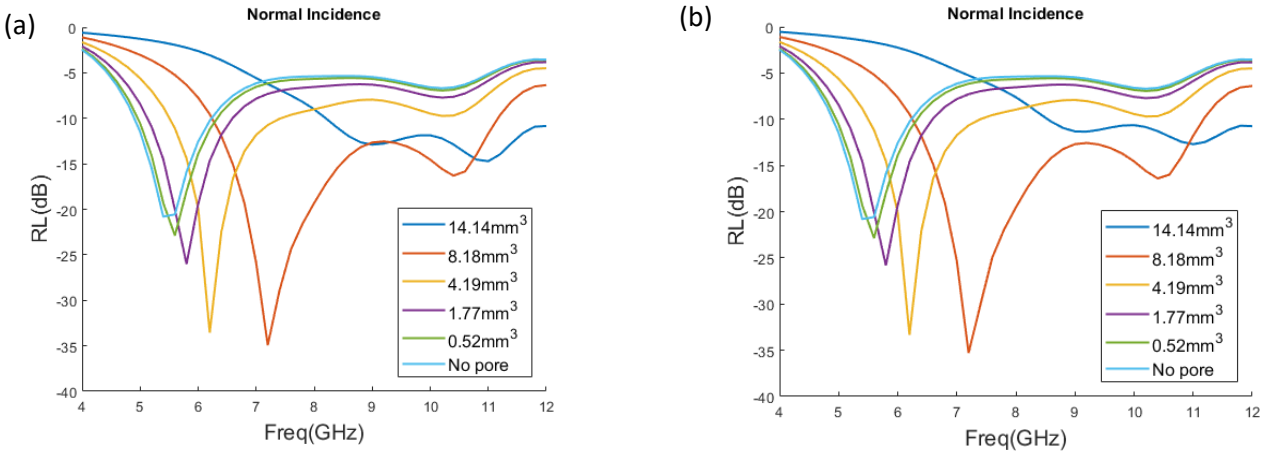

Fig 2.6 - Simulated change in RL at normal incidence of 3mm thick sample of a 30 wt% graphene/ Fe_3O_4 paraffin wax composite with a single cubic pore (a) and single spherical pore (b) as a function of pore volume.

To help understand the enhancement in RL seen in Fig 2.6 it is worth investigating the normal electric field distribution at certain frequencies of interest. Figure 2.7 shows a center slice of the normal electric field distribution for a 3mm x 3mm x 3mm unit cell with a single spherical pore (volume = 8.18 mm^3) positioned in the center. Metamaterial absorbers display enhanced absorption when geometries satisfy certain conditions that help to create resonant waves in the interior of the material [97]. The increases in RL that are see in Fig 2.7(a) are represented here by large increases in the electric field. At 4 GHz, there is very little enhancement of the electric field, which is illustrated in the fact that in Fig 2.7(a), the RL is -2 dB. At 7.25 GHz and 10.5 GHz however, we can see that there is significant enhancement of the electric field, particularly in the edges of the spherical pore in the x direction.

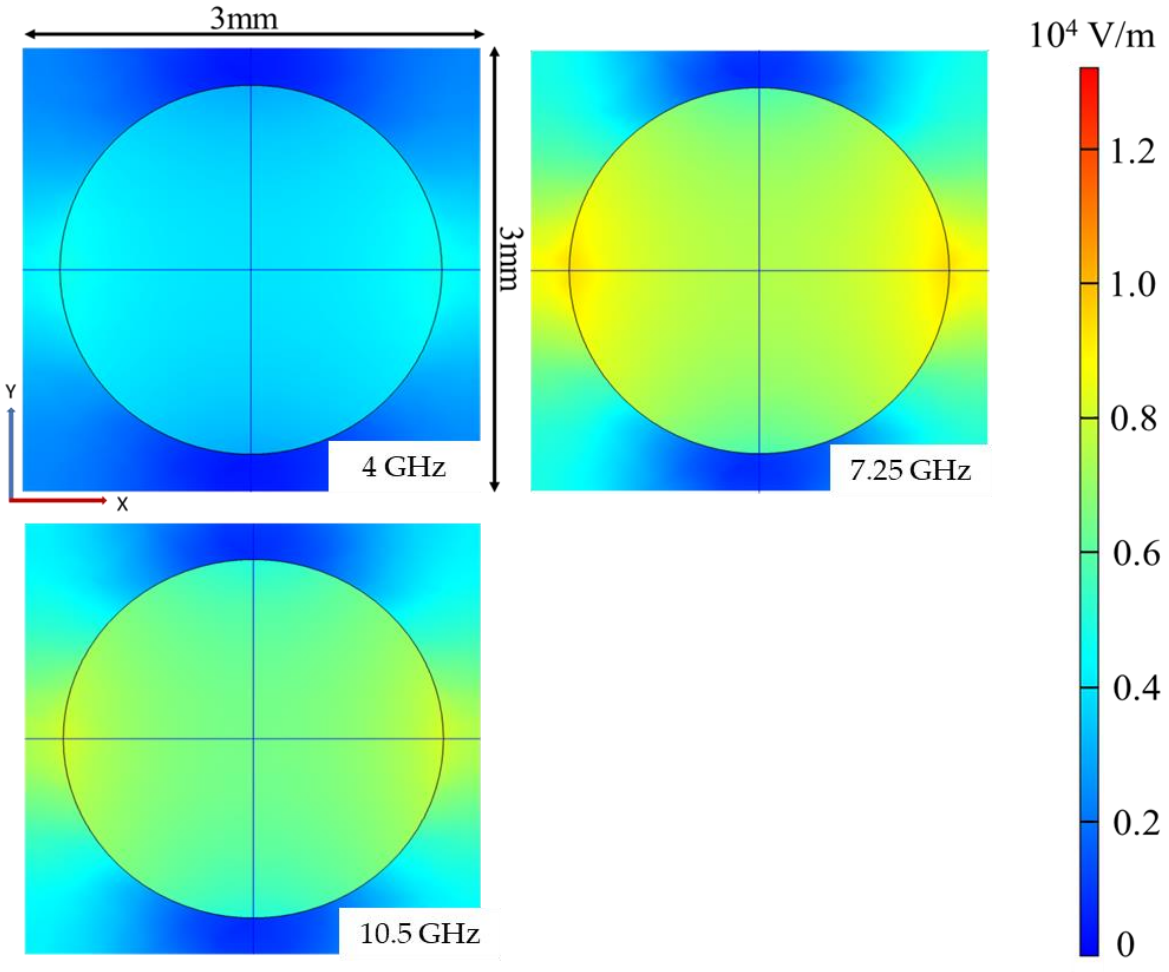

Fig 2.7 Top-down view of the center of a 3x3x3 mm unit cell with a single spherical pore (volume = 8.18 mm^3) positioned in the center. The material is subject to a normally incident electromagnetic wave at specific frequencies and the pictures are colored according to the strength of the normal electric field distribution. Results are shown for 4 GHz, 7.25 GHz, and 10.5 GHz.

Figure 2.8 shows the electric field distribution at the same frequencies as Fig 2.7, but for a single spherical pore with a volume of 1.77 mm^3. The composite with a smaller periodic pore displayed a worse RL than the larger pore, which can be seen in the lack of electric field enhancement. The normal electric field distribution is clearly very sensitive to the geometric arrangement of periodic pores.

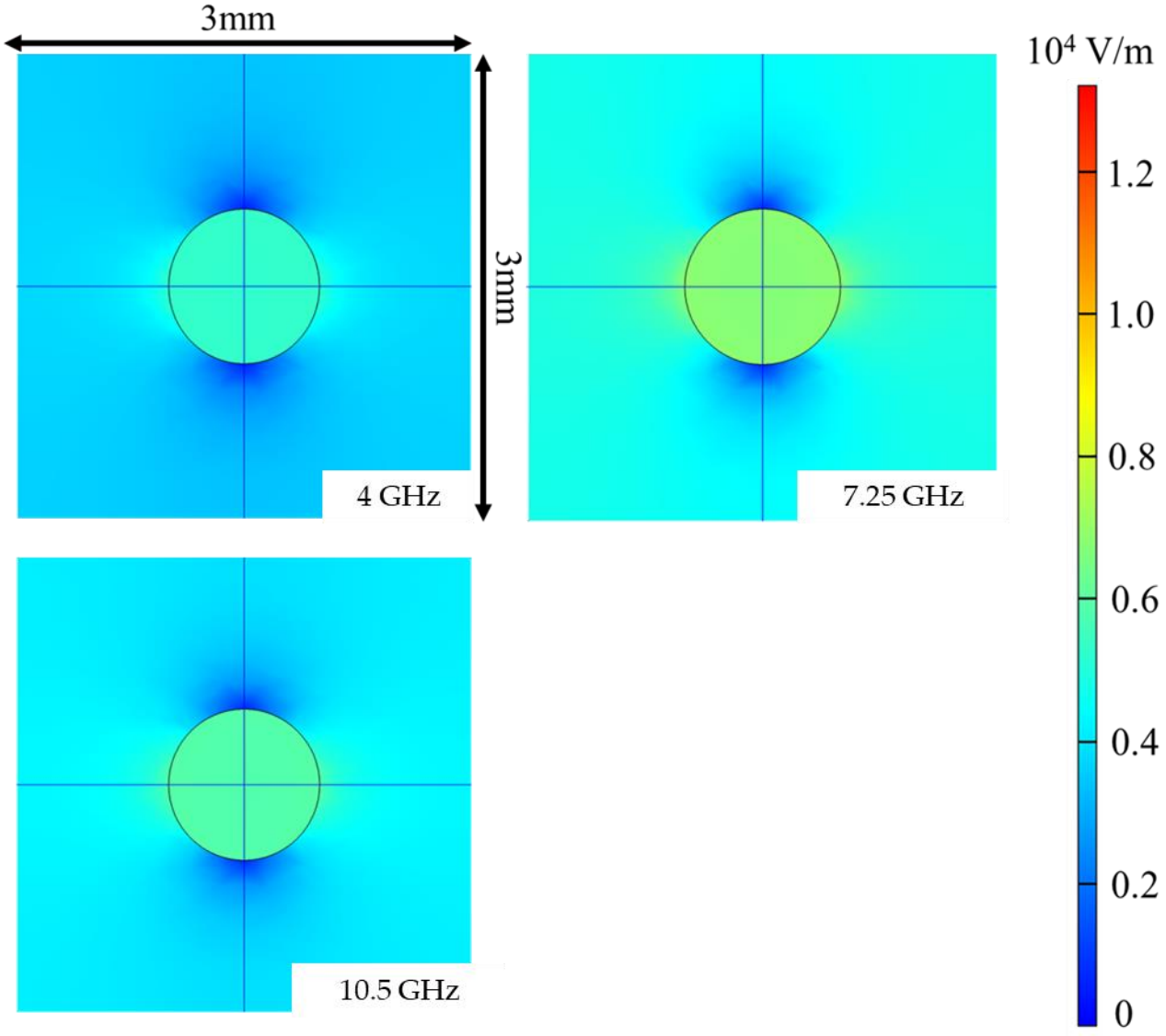

Figure 2.8 - Top-down view of the center of a 3x3x3 mm unit cell with a single spherical pore (volume = 1.77 mm^3) positioned in the center. The material is subject to a normally incident electromagnetic wave at specific frequencies and the pictures are colored according to the strength of the normal electric field distribution. Results are shown for 4 GHz, 7.25 GHz, and 10.5 GHz.

In addition to geometric variation in the pore shape, we also investigated the effect of changing the cell wall size for the unit cell described in Fig 2.6. We fixed the pore geometry as a sphere with a dimeter of 2.5 mm and changed the width or length of the unit cell along the x and y direction while keeping the other direction constant. This is equivalent to changing the spacing between pores. The calculated RL for these changes is shown in Figure 2.9. the pore. In Fig 2.9a we can see that the RL is insensitive to changes in the y-direction; the RL improves by a few dB.

On the other hand, modifications in the cell wall size in the x-direction has dramatic effects on the RL as shown in Fig 2.9b. By decreasing the spacing between neighboring pores, we can improve RL to as much as -51 dB.

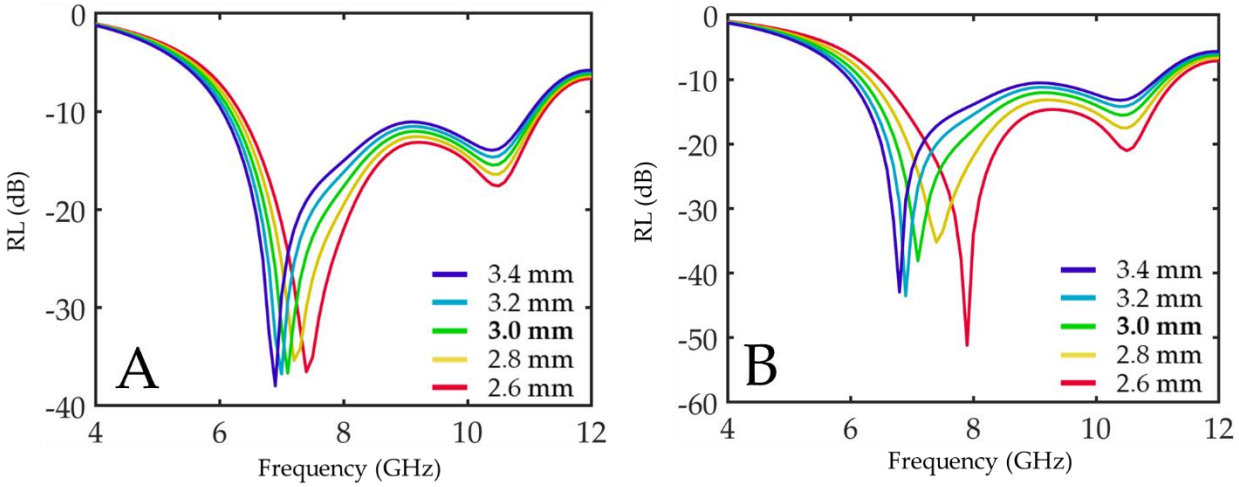

Fig 2.9 – Calculated RL a 3x3x3 mm slab of material with EM properties the same as the material in Fig 2.5. A single spherical pore with D = 2.5 mm has been placed in the center of the material. In (A) we have varied the size of the unit cell in the y direction while holding the x direction constant. In (B) we have varied the size of the unit cell in x-direction while keeping the y direction constant.

2.5 Discussion

The study of foamed materials for EMI shielding has been steadily growing in recent years. This work describes a methodology for optimizing the pore geometry based on the intrinsic material properties. The morphologies of foamed materials are achieved through a combination of temperature, pressure, filler type, and filler dispersion that is presented in each new system. When foaming is used, the products display high absorptive capability, but only after several lengthy optimization steps. Due to the importance of a well-controlled, repeatable, and less resource intensive method for EMI shield development, a high-throughput computational approach is highly desirable.

3D printing and compression molding are potentially versatile and facile methods to produce high-quality polymer composite EMI shields. Our three-step approach allows for model-guided optimization of the polymer composite foams. Monte-Carlo simulations combined with derivative free optimization techniques can effectively sample a much larger parameter space that is unavailable in a laboratory setting. The greater degree of control and repeatability that is

offered by different fabrication methods presents further advantages for future EMI shields since shape and size of pore morphology play important roles in EMI shielding technologies.

The preliminary results of this study show the strong dependence of pore geometry of the RL peak seen in Figs 2.5 and 2.6. In previous studies involving the effect of morphology on the shielding properties of polymer composite foams, an increase in material absorption has been associated with smaller pore morphologies [98]. Ling 2013 showed that as the pore size diameter decreased from 15.3 um to 9 um, there was a corresponding increase in SE of almost 20 dB. However, the decrease in pore size was the result of an increase in graphene loading from 1% to 10% [65]. This common trend seen in polymer composite foams is often used as a justification for pursuing materials with very small pore morphologies and high pore densities. However, it is also known that by simply increasing conductive filler content, independent of morphology, can also lead to an increase in SE.

Table 2.1- Max RL of Foamed Composites

Author	**Max RL (dB)**	**Average Pore Size (μm)**
Ling 2016 [65]	-13	N/A
Gavgani 2016 [99]	-23	1200
Kuang 2016 [100]	-25	52
Song 2016 [101]	20	N/A

In many polymer composite foams, an inverse relationship between the size of the pore diameter and the increase in SE is commonly reported [68,89]. Smaller pores, for a given volume, lead to a higher density of pores, and thus more scattering events. However, as compared to experimental results shown in Table 2.1, our model predicts that we can achieve a max SE of 35 dB with a spherical pore with diameter of 2.5mm. Our modeled shielding effect is higher than that of foamed and unfoamed materials in Table 2.1. The pore size is also on the order of millimeters instead of microns. This opens avenues for producing polymer composite EMI shields to higher throughput techniques that make up in speed what they lack in resolution.

In addition, the decrease in RL is not a monotonic trend, indicating that the effect of pore morphology requires a more complex investigation than simple parametric experimental or

computational studies. In foamed materials, the addition of larger pores showed a roughly monotonic decrease in RL up until 8.18 mm^3. However, increasing the pore volume to 14.14 mm^3 not only caused a dramatic shift in the position of resonance peaks, but also greatly increases the value of the RL. By exploring a truly continuous parameter space through a computational approach, one can arrive at optimal morphologies for EMI shielding.

2.6 Conclusions

With FEM software, we have shown that by adding periodically placed pores to polymer composites, we can improve RL. The improvements in RL were shown to be sensitive to pore shape, pore sizing, as well as the spacing between pores. This technique can is material agnostic and similar analyses can be applied to any material with a measurable complex permittivity and permeability. A simulation-guided approach is critical for the development of next generation EMI shielding materials.

CHAPTER 3

Validation of Model Guided EMI Shield Development

3.1 Chapter Synopsis

This chapter details the research done to successfully validate the model-based approach for the development EMI shields with periodic porous geometries presented in Chapter 2. A typical PLA/xGNP system was fabricated with xGNPs of various aspect ratio. After extracting their intrinsic electromagnetic properties, samples with cylindrical pores of various heights were fabricated. The shielding properties of these experimental samples were compared to simulations of materials with the same geometries. It was seen that the simulations could predict the trends in SE as well as the frequencies of minima and maxima for PLA/xGNP composites with different aspect ratio fillers. The validation of this modeling approach opens the door for material development and pore geometric optimization.

3.2 Introduction

In this study, we present a novel approach that relies on intrinsic electromagnetic properties to model the introduction of air-filled pores into conducting polymer composites to produce lightweight absorbers. Graphene nanoplatelet/poly-lactic acid (xGNP/PLA) composites with different aspect ratio fillers were characterized and their complex electromagnetic properties were extracted. Using these materials, we fabricated non-perfect electrical conductor (PEC) backed, periodic porous composites and explored the effect of pore geometry and filler aspect ratio on EMI shielding properties. Furthermore, we developed and experimentally verified a COMSOL model that will allow for rigorous, high-throughput optimization of absorbers with periodic porous geometries. Finally, we extend the modeling approach to explore the effect of pore addition on PEC-backed composites. With a fully validated computational model, new materials can be

quickly and thoroughly studied to produce fully optimized absorbers with periodic porous geometries.

3.3 Experimental

3.3.1 Composite Design Overview

Figure 3.1 shows the multistep design methodology for the design of optimized periodic porous EMI shields. In the first step (Figure 3.1 A), polymer composite plaque made of a dispersion of xGNP in PLA is produced and the complex electromagnetic parameters of the composite material are extracted using a Vector Network Analyzer (VNA). In the second step (Figure 3.1 B), the complex electromagnetic parameters are used to simulate the scattering parameters and reflection loss (RL) of periodic-porous composites using COMSOL 5.3a®. In this step, geometric parameters such as the shape of a pore, position of a pore, thickness of the sample, thickness of the cell wall, and the number of vertically stacked pores, are modulated to identify geometries that yield desirable EMI absorption. Following identification of optimized geometry, the final step (Figure 3.1 C) consists of using compression molding and Computer Numeric Control (CNC) milling to fabricate composite samples with and without pores. The performance of fabricated samples is verified using a VNA.

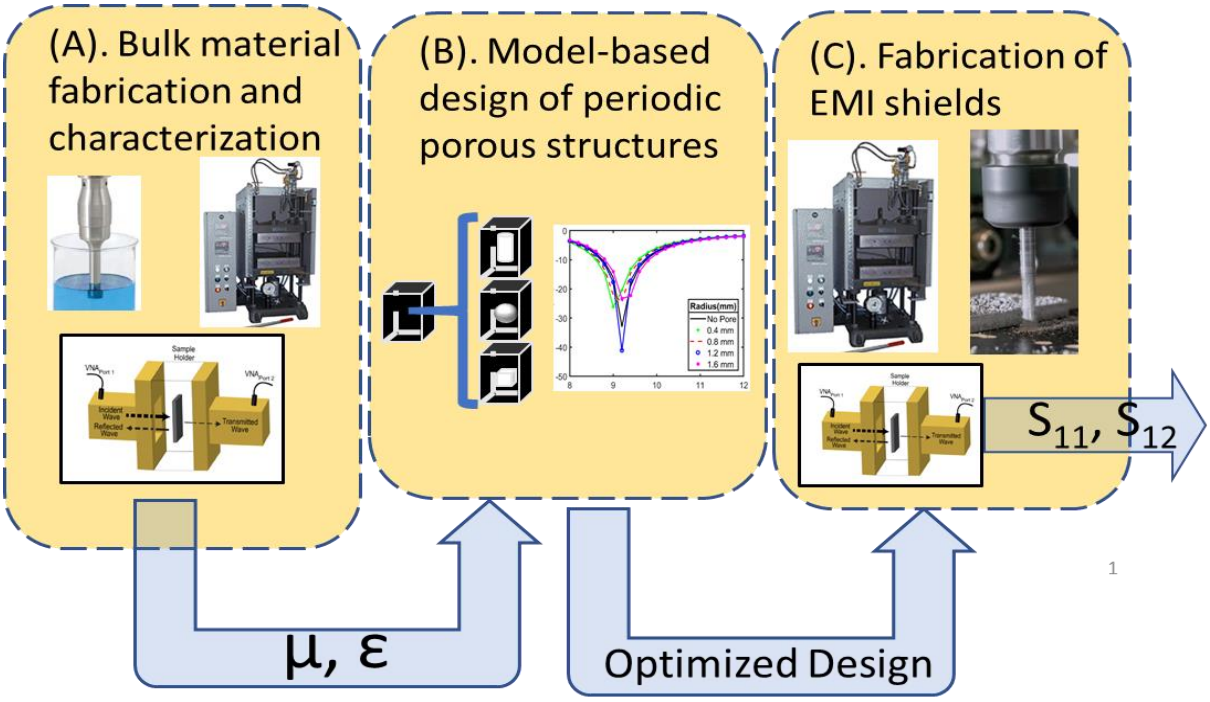

Fig 3.1 - Three step design methodology for new EMI shields. (**A**) Composite materials are fabricated through a combination of ultrasonication and compression molding. Complex electromagnetic properties are extracted using a VNA. (**B**) Measured complex electromagnetic parameters are used in the COMSOL environment to optimize periodic porous geometry. (**C**) Optimized geometries are fabricated using a combination of compression molding and CNC milling. Final EMI shielding properties are measured and tested once more in a VNA.

3.3.2 Materials

Graphene nanoplatelets (xGNPs) with three different aspect ratios, M25 (D = 25 μm, t = 9 nm), M15 (D = 15 μm, t = 9 nm), and C750 (D =2 μm, t = 9 nm), were obtained from XG Sciences. Ingeo 4043D PLA pellets were purchased from 3DX. PLA was selected as the matrix polymer because future studies involving fused deposition modeling are planned. Methylene chloride (DCM) was supplied by Fisher Scientific.

3.3.3 Material Fabrication and Characterization

We used a conventional solution process to prepare composite material for step 1 (Figure 3. 1 A) [102]. 5 wt % loading. M25 Grade xGNPs (500 mg) were added to DCM and ultrasonicated for 1 h using a QSonica 700 probe (Qsonica, Newton, CT, USA) tip ultrasonicator to achieve dispersion. The same amount of energy is used for all composites, so they are assumed to have the same relative degree of dispersion. Then PLA pellets were added to the DCM dispersion and mixed overnight using a stir bar. Next the mixture was ultrasonicated for another 1 h. Finally, the mixture

was cast into a large mold and left to dry overnight at ~110 °C. The resulting films were processed into smaller flakes using a grinder and compressed in a hot press at 230 °C and 20 MPa to obtain flat composite disks with a dimeter of 25 mm (Carver, Wabash, IN, USA). The aspect ratio of the xGNP was varied in the final composite.

The morphology of samples was observed using a JEOL 1500 scanning electron microscope (JEOL, Peabody, MA, USA). The samples were cryo-fractured in liquid nitrogen, and sputter coated with gold prior to visualization. The DC electrical conductivity of composites was determined using through thickness, two-point probe method on rectangular samples with a silver paint coating on each surface to ensure good electrical contact. A constant voltage of 5 V was applied to the samples and conductivity (σ) was calculated as

$$(3.1)\ \sigma = \frac{t}{\Omega w l}$$

where Ω is the measured electrical resistance, l is the length of the sample, w is the width of the sample, and t is the sample thickness. The EMI shielding effectiveness and complex electromagnetic parameters of xGNP/PLA composites were measured using an Anritsu MS4644B VNA (Anritsu, Atsugi, Japan). Prior to measurement, samples were cut and polished to achieve the desired cross-section for electromagnetic characterization using a standard X-band (8–12 GHz) waveguide setup (22.86 mm × 10.16 mm). A total of 1601 data points were taken in this frequency range for each sample. The permittivity and permeability of PLA composites were extracted from measured S-parameters using the Nicolson-Ross-Weir (NRW) method. [103,104]

For step 2 (Figure 3.1 B), Finite Element Modeling was performed in COMSOL. The modeled geometry consists of a 3D periodic Cartesian lattice with a unit cell that contains arbitrarily shaped air-filled pores inside of a material with pre-defined frequency dependent electromagnetic parameters. COMSOL's Radio Frequency module is used to perform full field calculations of either a TE or TM incident wave that excites the structure from the top from a predefined angle of incidence (θ) (Port 1). Mesh refinement is used to maintain a minimum element quality of greater than 0.2 to ensure accurate results. The structure's S11, S12, and reflection loss (RL) are calculated over the X-Band with a sampling interval of 0.1 GHz. A characteristic unit cell is shown in Figure 3.2. The unit cell repeats periodically in the x-y plane and has finite thickness in the z-direction. The top of the cell is terminated by a perfectly matched layer (PML) to prevent secondary

reflections, and the bottom of the cell is terminated either by a perfect electrically conducting (PEC) or a second port for study of non-PEC backed composites.

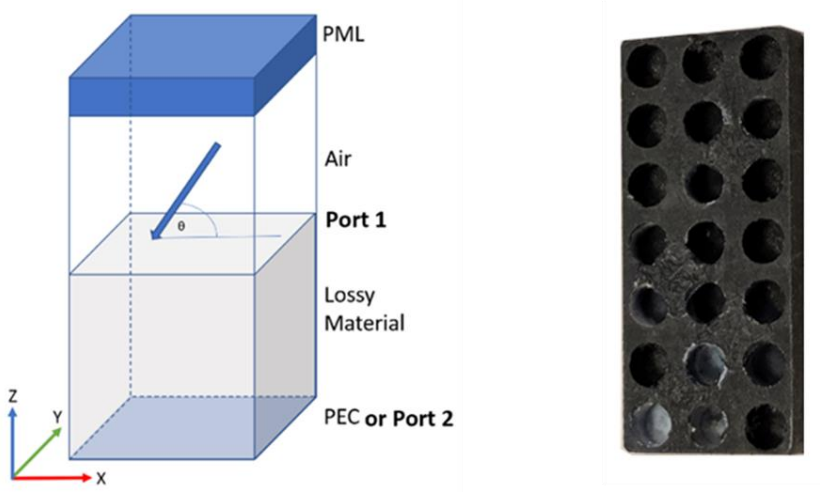

(**A**) (**B**)

Fig 3.2. - (**A**) Schematic of unit cell used in COMSOL simulations. The top of the cell is truncated with a perfectly matched layer (PML) to prevent reflections at the top boundary. EM waves with incident angle θ are generated from Port 1 and are incident upon a lossy material with predefined permittivity and permeability. The bottom of the cell is either backed by a perfect electrical conductor or a second port. The unit cell is periodic in the x/y direction and finite in the z direction. (**B**) A representative xGNP/PLA sample after being machined. The periodic porous array is milled on two separate halves which are then bonded together to form completely encapsulated pores.

To prepare samples for step 3, xGNP/PLA composites with a periodic array of cylindrical pores (Figure 3.2 B) are fabricated using a Tormach PCNC440 milling machine (Tormach, Waunakee, WI, USA) and their EMI shielding properties were characterized using a similar setup in step 2. Measured EMI shielding properties were compared to simulated values from step 2 for model validation.

3.4 Results and Discussion

3.4.1 Microstructure and Conductivity of xGNP/PLA Composites

Figure 3.3 shows representative SEM images of the cross section of xGNP/PLA composites with different aspect ratio fillers. We have observed a degree of agglomeration which is attributed to long solvent evaporation times giving fillers time to coalesce. There is also a degree of filler alignment that can be seen, particularly in Figure 3C. This can be ascribed to the compression molding that is used to form composite plaques. From the SEM image of C750/PLA (Figure 3B) we can clearly see that there is a large separation between filler material as compared to the other

composites. For this specimen we expect a decrease in the inter-nanostructure connections that will ultimately play an important role in the EMI shielding characteristics of the composite material.

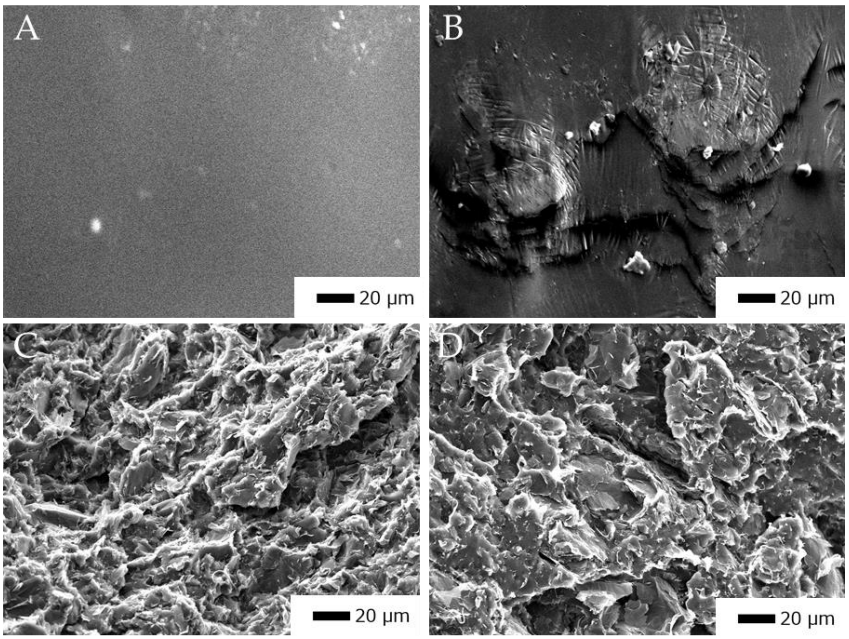

Fig 3.3 - Representative SEM images of (**A**) PLA (**B**) 5% C750/PLA (α = 222), (**C**) 5% M15/PLA (α = 1667), and (**D**) 5% M25/PLA (α = 2778) composites.

Table 1 shows the DC electrical conductivity of 5% xGNP/PLA composites with different aspect ratio xGNPs at room temperature. As the aspect ratio of the filler material increases, there is an increase in conductivity from 6×10^{-10} for C750 filler material to 1.5×10^{-1} for M25 filler material. It is well known that increases in aspect ratio decrease the percolation threshold, thus making it easier to form conductive networks [105]. In addition, the increase in maximum electrical conductivity also increases with higher aspect ratio [106].

Table 3.1. Measured conductivity of xGNP/PLA composites and the reported aspect ratio of xGNP filler material.

Material	**Conductivity (S/m)**	**Aspect Ratio**
PLA	10^{-13}	N/A
5% C750/PLA	6×10^{-10}	222
5% M15/PLA	3×10^{-4}	1667
5% M25/PLA	1.5×10^{-1}	2778

3.4.2 Complex Electromagnetic Properties of xGNP/PLA Composites

The permeability of PLA composites is not measurably affected by the addition of xGNP since there is no magnetic component in the filler material and any effects are likely due to measurement error. On the other hand, there is a measurable effect in the complex permittivity due to xGNP loading. The permittivity of neat polymers is usually low but can be enhanced through the addition of conductive filler material; the polarization of the matrix, polarization at matrix/filler interfaces, and the polarization of conductive filler material all make contributions to the final composite permittivity [107].

Figure 3.4 shows the experimentally derived real (ε') and imaginary (ε'') portions of the complex relative permittivity as a function of frequency for the xGNP/PLA composite plaques. The real part is related to the storage capacity of electric energy mainly due to the degree of polarization within the material [108]. The imaginary permittivity is the associated degree of energy dissipation from Joule heat generated during conductance and thermal energy due to relaxation loss mechanisms [109]. The real permittivity is sensitive to the type of xGNP filler. The real permittivity of unmodified PLA is ~2.8 across the entire frequency range and increases to ~17.6 for 5% M25 loading. Previous studies have shown that if the filler concentration is low, there is not a measurable effect on ε' with respect to frequency. In the case of our xGNP/PLA composites there is minimal frequency dependence in the X-Band. It is known that for ellipsoidal particles, the percolation threshold decreases with increasing aspect ratio [110]. Therefore, at a fixed loading, higher aspect ratio xGNP fillers will have more conducting pathways and display higher values for real permittivity due to increased capacitor like interactions between filler particles [111,112].

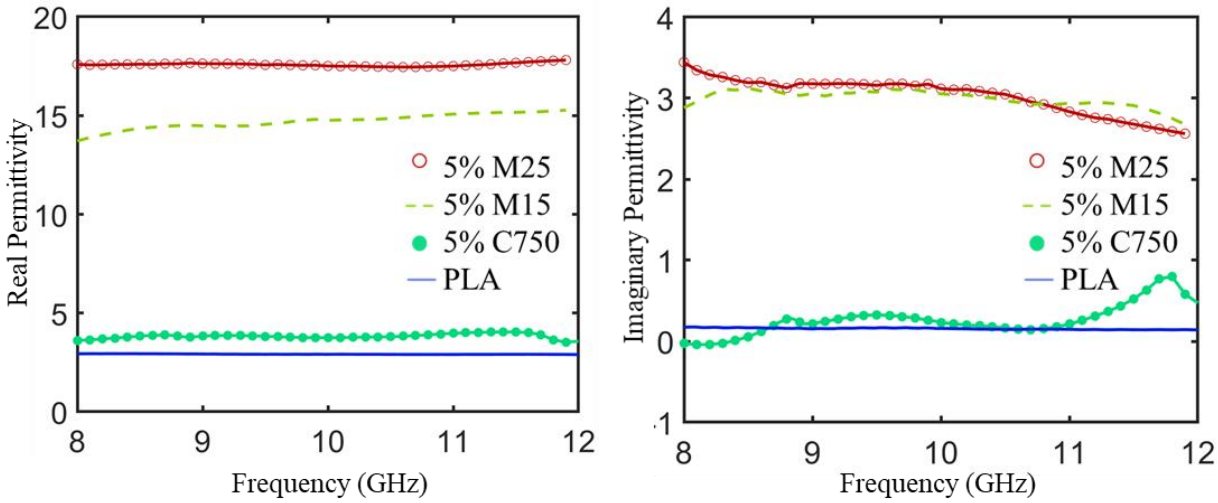

(**A**) (**B**)

Fig 3.4 - The real part (**A**) and imaginary part (**B**) of the complex permittivity for 5 wt % xGNP/PLA composites fabricated with different aspect ratio filler material. The properties of neat PLA are also displayed as reference.

With increasing aspect ratio of xGNP filler, there is also an increase in the imaginary part of the permittivity. This can be attributed to enhanced polarization loss and higher hopper conductivity due to enhanced filler interactions [113,114]. The 5% M25/PLA and 5% M15/PLA samples exhibit slightly decreasing ε'' with increasing frequency, but the 5% C750/PLA displays a distinct relaxation peak [115].

3.4.3 EMI Shielding Effectiveness of Non-PEC Backed xGNP/PLA Composite Plaques in a Waveguide

The effect of different grades of graphene in xGNP/PLA on EMI SE was investigated. EMI shielding refers to reflection and absorption of incident electromagnetic radiation by a material. The efficiency of a shielding material is dependent on the frequency of incident EM radiation, shield thickness, as well as the intrinsic electromagnetic properties of the material [116]. EM wave propagation in any medium is dependent on the impedance of the medium ($Z = \sqrt{(\mu/\varepsilon)}$) as well as the EM wave's velocity inside of that medium ($\upsilon = 1/\sqrt{\mu\varepsilon}$) [117]. When a traveling wave encounters an interface with different impedances on either side, there will be a change in wave velocity as well as partial reflection with the magnitude of this interaction determined by the difference in impedance between the two mediums [118]. Any changes in permittivity or permeability will impact a materials response to electromagnetic radiation, particularly if that

material is a nonconductive polymer matrix. The total EMI shielding effectiveness (SE_T) is defined as.

(3.2) $SE_T\ (dB) = -10\ log_{10}(|S_{12}|^2)$

The mechanisms of EMI shielding for a particular system can be explored through incident power balances defined by the fraction of incident power that is reflected (R = $|S_{11}|^2$ = $|S_{22}|^2$), transmitted, (T = $|S_{12}|^2$ = $|S_{21}|^2$), and absorbed (A = 1 – T − R). Figure 4.5 shows the SE_T and power balance for 3 mm thick PLA composites with different aspect ratio xGNPs measured in a waveguide over the X-Band. As illustrated in Figure 5A, SE_T increases with increasing xGNP aspect ratio over the entire frequency range with a minimum of 12 dB at 8 GHz for the M25/PLA composite. The observed trends and measured SE_T for xGNP/PLA composites resemble those of xGNP/PBAT composites with similar complex electromagnetic parameters [119]. For M15 and M25 composites, SE_T decreases with increasing frequency, which is a phenomenon that has been observed in other conductive polymer composites [120,121]. C750 and PLA exhibited minimal frequency dependence for SE_T in this frequency range. Yang et al. observed the *SE* of carbon-non fiber/polystyrene foams and found that at loadings of 10% and higher there was a dependence on frequency but did not see the same effect with lower loadings of carbon nanofiber [122].

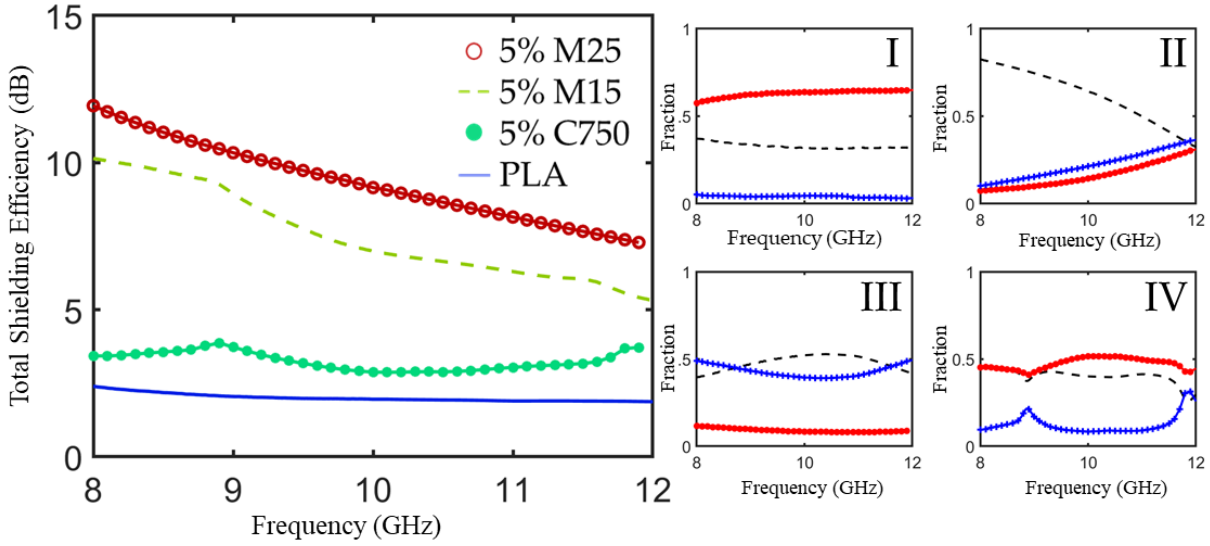

(**A**) (**B**)

Fig 3.5 - (**A**) Total shielding efficiency as measured in an X-band waveguide for xGNP/PLA composite plaques fabricated with different aspect ratio starting material. (**B**) Power balance for 5 wt % xGNP/PLA composite plaques loaded with (I) neat PLA, (II) M25, (III) M15, and (IV) C750. All plaques have a thickness of 3 mm.

The power balances for xGNP/PLA composites with different aspect ratio fillers are plotted in Figure 3.5 (B). For neat PLA composites, most of the incident EM radiation transmits through the material; there is a portion of the power that is reflected due to slight impedance difference with air, and almost no incident radiation is absorbed. For all grades of xGNP, the transmission coefficient is lower than that of neat PLA. Over the entire investigated range, higher aspect ratio xGNP fillers display low levels of transmission and high levels of reflection; as permittivity of nanocomposites increases without a change in permeability, the higher impedance mismatch at the interface leads to increased reflection. It can be concluded from these data that reflection is the primary shielding mechanism for xGNP/PLA composites in the X-band. This agrees with similar conductive polymer composites systems.

3.4.4 EMI Shielding Effectiveness of Non-PEC Backed PLA/xGNP Composites With Cylindrical Pores

For non-PEC backed shields, the pursuit of higher conductivity and higher impedance match is an ideal strategy for achieving high-performing, reflection-dominated EMI shields. However, high performing EMI absorbers rely on complementary effects between dielectric loss, magnetic loss, conductivity, and impedance matching [123,124]. Controlling impedance mismatch while simultaneously ensuring there are enough pathways for EM dissipation can be difficult. As previously discussed, one method for achieving this balance is using foamed composites. By introducing air in the form of a highly porous morphology, the SE_T of foamed composites can be greatly improved as compared to their non foamed counterparts due to decreased impedance mismatch at the surface as well as increased interactions at pore-matrix interfaces inside of the foam [66,125]. However, the inability to model the shielding efficiency of foamed materials a priori limits their development to trial and error experiments that are costly in terms of time and resources.

In order to control impedance matching we propose using an arrangement of periodic pores that can be explicitly determined beforehand. Because the pores are defined independently of materials processing, there is added flexibility that can be given in terms of the size, shape, and position of the pores. To demonstrate this point, the effect of adding cylindrical pores with a constant radius and varying height in a periodic layout was explored and the corresponding

geometries were modeled in COMSOL to demonstrate the ability to successfully model the structures.

Figure 3.6 shows the measured scattering parameters and power balance as measured in a waveguide for 4.6 mm thick 5 wt % M25/PLA composites with and without cylindrical pores of varying height. The trend for the modeled total shielding efficiency follows that of the experimental data illustrating the model's utility in guiding the selection of pore geometry. The non-porous composite exhibits a maximum SE_T of 10.9 dB at 11.6 GHz. With the addition of a single layer of periodic cylindrical pores, there is a monotonic decrease in SE_T as well as a gradual shift of minimum SE_T to higher frequencies with increasing pore height. The addition of pores also has a measurable effect on the power balance as shown in Figure 4.6b. As pore height increases there is a noticeable decrease in the reflection coefficient at lower frequencies as compared to the sample with no pores. This can be attributed to the increased impedance matching due to the addition of air to the sample. Increased interaction with conductive pathways as well as increased internal reflections at intra-composite interfaces leads to an increase in absorption coefficient over the entire frequency range for porous samples. There is a noticeable increase in the transmitted power fraction, with as much as 30% of incoming radiation transmitting for the sample with 4 mm pores. For this material, the addition of pores leads to higher absorbed power fractions, but lower SE_T as compared to non-porous samples. It is important to point out that the composition of the material, 5 wt % M25/PLA, has not been optimized for high shielding efficiency.

As mentioned above, optimization of foamed composites is limited by the lack of computational tools for modeling morphology as well as the SE due to unique foamed morphologies. To demonstrate the validity of a model guided approach to periodic porous geometries, we simulated these periodic structures in the COMSOL environment using the measured electromagnetic properties for 5% M25/PLA. Overlaid against the measured results in Figure 3.6, there is general agreement in the trends between the simulated and measured scattering parameters and power balance for cylindrical pore examples. The lack of absolute correlation can be attributed to differences between the model and the actual sample such as pore mismatch when aligning the two separate halves or precision errors that can occur during machining.

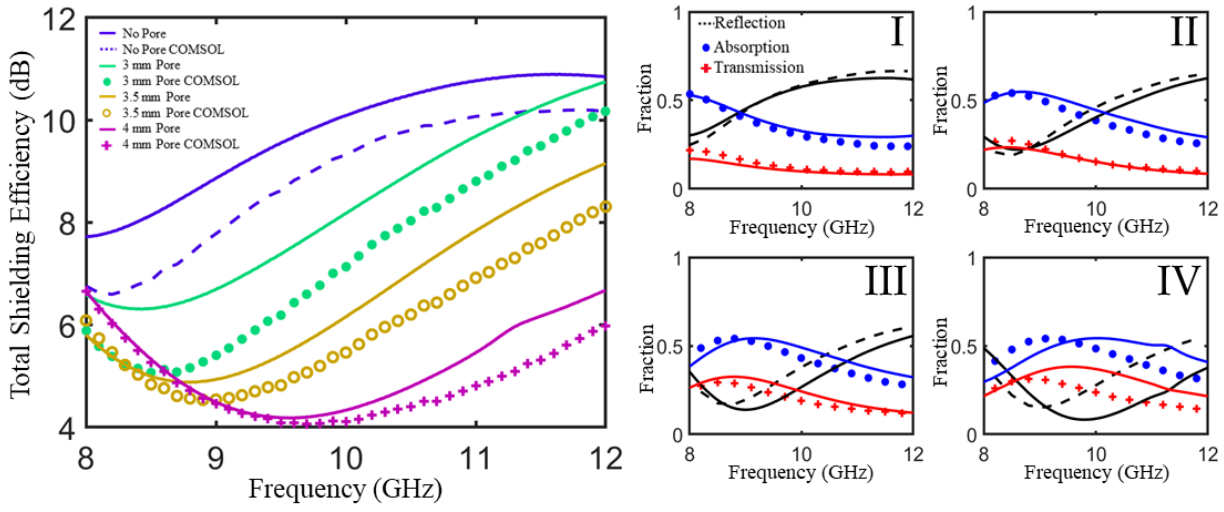

(**A**) (**B**)

Fig 3.6 - (**A**) Measured and simulated total shielding efficiency in an X-band waveguide for a 5% M25/PLA composite plaque with and without pores of varying height. (**B**) Measured and simulated power balance for a 5% M25/PLA composite plaque (I) without pores, (II) a cylindrical pore with a height of 3 mm, (III) a cylindrical pore with a height of 3.5 mm, and (IV) a cylindrical pore with a height of 4 mm. All plaques have a total thickness of 4.6 mm. All cylindrical pores have a diameter of 2.54 mm. Simulated data is depicted with symbols and experimental data is represented by solid lines of the same color.

This process was repeated for 5% M15/PLA composites and the resulting comparison between experimental and simulated scattering parameters and power balance is shown in Figure 3.7. It can again be seen that there is good agreement between the trends for experimental and simulated data. There is also a non-monotonic increase in SE_T with an increase in pore height for 5% M15/PLA samples that is worth noting because it shows that a modeling approach is an effective method for identifying non-monotonic trends.

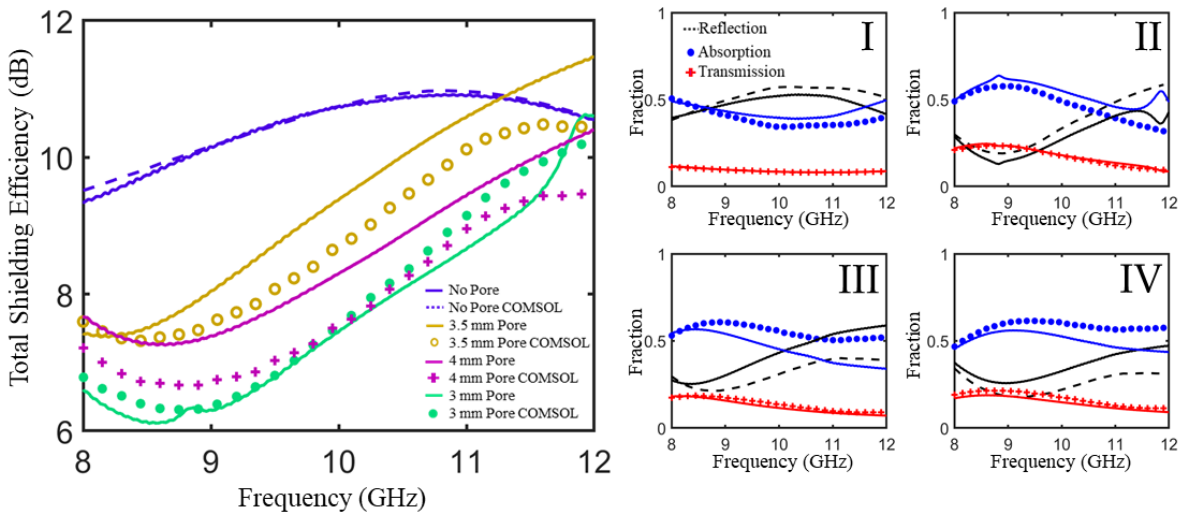

(A) **(B)**

Fig 3.7. (**A**) Measured and simulated total shielding efficiency in an X-band waveguide for a 5% M21/PLA composite plaque with and without pores of varying height. (**B**) Measured and simulated power balance for a 5% M15/PLA composite plaque (I) without pores, (II) a cylindrical pore with a height of 3 mm, (III) a cylindrical pore with a height of 3.5 mm, and (IV) a cylindrical pore with a height of 4 mm. All plaques have a total thickness of 4.6 mm. All cylindrical pores have a diameter of 2.54 mm. Simulated data is depicted with symbols and experimental data is represented by solid lines of the same color.

3.4.5 Reflection Loss of PEC-Backed xGNP/PLA Composites

In many applications involving EMI shields, the absorbing material is backed by highly reflective metallic casings. These types of casings are common in many applications, and as mentioned earlier, will mainly reflect any incident EM radiation. For this purpose, it is also informative to explore materials backed by a PEC instead of air, resembling a scenario in which an absorber is placed on top of a metallic casing. We showed in previous simulations that for a composite made of 30 wt % graphene/Fe3O4 paraffin wax composite, the addition of a single spherical pore with a radius of 1.25 mm could cause as much as a 13 dB increase in RL [126]. Figure 3.8 shows the results of COMSOL simulations demonstrating the effect of adding either a spherical pore (A) or a cylindrical pore (B) to a 4 mm thick sample with the complex electromagnetic properties of 5% M25/PLA. The addition of a single pore, when optimized, can have a pronounced effect on the RL; a single spherical pore with a radius of 1.2 mm can lower RL from −32 dB to −45 dB at a frequency of 9.2 GHz. The addition of cylindrical pores can also have a measured effect on RL, but there are subtle differences in the position of peaks as compared to the spherical pore. Particularly for a radius of 1.6 mm, the minimum peak position varies by almost

one GHz. The improvements in RL as well as the different effects of different geometries reinforces the need for model guided experimentation for EMI shielding materials.

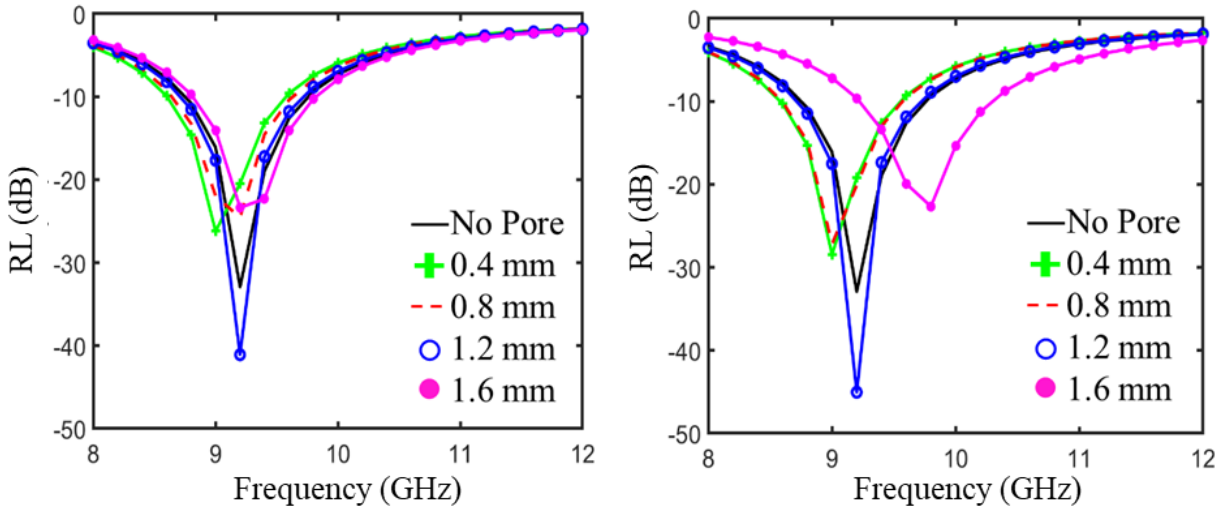

Fig 3.8 - Modeled reflection loss for 5%M25/PLA with thickness of 4 mm and modified with either a single spherical pore (**A**) or a cylindrical pore (**B**). Both plots show the effects of a changing radius. In the case of the cylindrical pore, the height is fixed at 1.8 mm.

3.5. Conclusions

The connection between experimental and simulated data for xGNP/PLA composites illustrates the promise of a modeling guided approach to pore addition starting from known electromagnetic parameters. The morphology, conductivity, and electromagnetic properties of xGNP/PLA composites with different aspect ratio xGNP fillers were explored. It was found that SE_T in the X-band improves with higher aspect ratio fillers at a fixed weight percentage. By analyzing the shielding coefficients, it was shown that reflectance is the dominant shielding mechanism due to large impedance mismatch at the front face. In addition, the effect of adding periodically arranged cylindrical pores on the EMI shielding properties was explored. The addition of pores had the desired effect of increasing absorption while decreasing reflection but increased the transmission as well. The porous geometries were simulated in COMSOL and the trends in shielding properties were found to be agreement with experimental data.

CHAPTER 4

Polymer Composites With Segregated Structures For EMI Shielding

4.1 – Chapter Synopsis

To work around problems related to high loading and filler dispersion, we investigated the use of polymer composites with a segregated structure for EMI shielding. We looked at the effect of filler loading on EMI SE as well as electromagnetic properties. In addition, we developed and characterized a novel segregated structure polymer composite with various additions of a magnetic component. The addition of a magnetic component was found to increase the overall SE, but at low magnetic loadings there was no marked improvement.

4.2. Introduction

As illustrated in chapter 3, the ability to effectively model periodic porous morphologies can open the path for fast and effective investigation of new metamaterial EMI absorbers. Keeping in mind that we have a tool for exploring geometry, there is a need to utilize this model in the context of materials more readily suited for EMI absorption. PLA/xGNP composites displayed minimal SE, even with the addition of pores, and required large weight percentages of xGNP filler. It is known that at high filler loadings, it is difficult to disperse xGNPs owing to strong Van Der Waals interactions that encourage filler agglomeration [127,128]. Furthermore, high filler loadings can lead to decreased mechanical properties resulting from filler agglomerates that act as stress concentrators [129]. To enhance our polymer composites EMI shielding abilities, it is important that we either improve our dispersing abilities or explore alternative routes for composite fabrication. One route that has potential is the fabrication of composites with segregated networks (Figure 4.1).

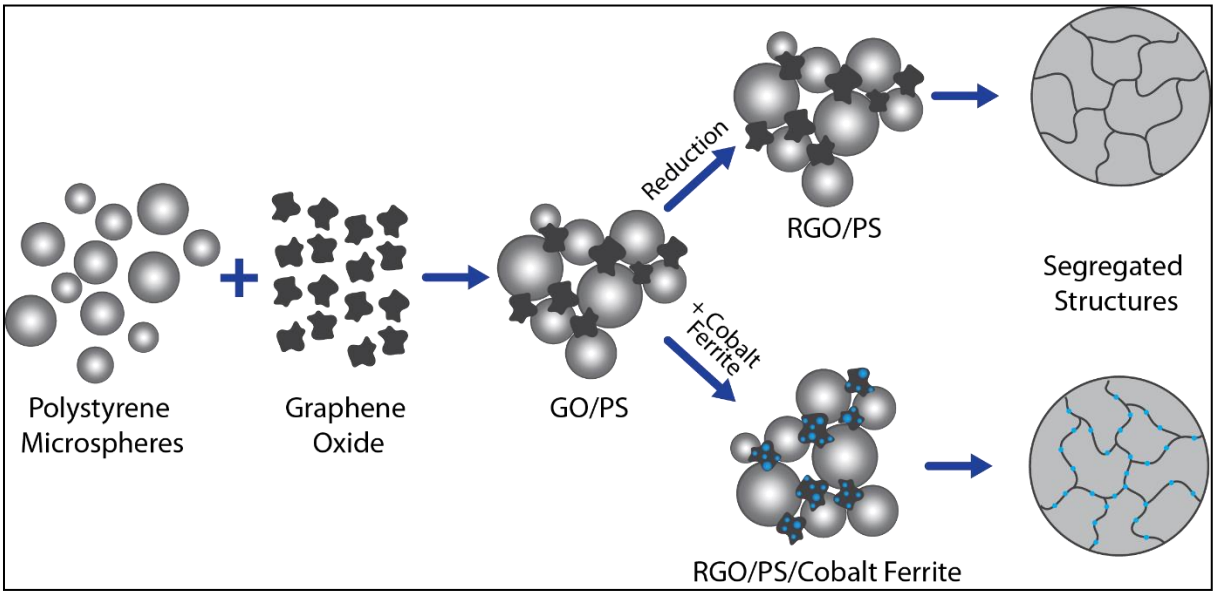

Fig 4.1 – Schematic showing the steps for the fabrication of PS/rGO or PS/rGO/CF composites. PS microspheres are first coated with graphene oxide (GO) then reduced with/without the presence of CF, then finally hot pressed to form segregated structures.

Polymer composites with segregated networks utilize processing methods that help to force highly conductive fillers like carbon black [130,131], carbon nanotubes [132,133], and graphene [134,135] into contact with one another. These conductive polymer composites (CPCs) have demonstrated improved electrical conductivity and lowered percolation thresholds when compared to CPCs with randomly dispersed filler material [136]. In a carbon black/polypropylene composite, the percolation threshold was lowered from 2.75 vol% to 0.37 vol% by incorporating a segregated structure [136]. A graphene/ABS composite with a segregated structure demonstrated a percolation threshold of 0.13 vol% [137]. Lower percolation thresholds, enhanced conductivity, and unique microstructures have led researchers to pursue these types of materials as EMI absorbers [138–140]. In segregated structures, the "skin" of closely packed polymer cells surrounded by conductive "membranes" make it difficult for EM waves to penetrate deep into the material as they are scattered and attenuated in a similar shielding mechanism to CPC foams.

In this study we investigate the effects of using a polystyrene/reduced graphene oxide (PS/rGO) nanocomposite with a segregated structure as an EMI shielding material. This material benefits from the low percolation threshold and high conductivity due to the segregated structure.

In addition to studying the effects of rGO loading on EMI properties, we also explore the effect of functionalizing the rGO surface with cobalt ferrite (CF) nanoparticles. This is the first time this material has been explored and characterized. A schematic illustrating the fabrication process is shown in Figure 4.1.

4.3 Experimental

4.3.1 Materials

M25 grade graphene nanoplatelets were received from xG Sciences. Sulfuric acid, phosphoric acid, potassium permanganate, hydrogen peroxide (30%), ethanol, styrene monomer, poly (vinyl pyrrolidone) (PVP, M_w = 40,000), azobisisobutyronitrile (AIBN), cobalt chloride hexahydrate, iron nitrate nonahydrate, and sodium hydroxide were purchased from Sigma Aldrich.

4.3.2 Preparation of GO

GO was prepared with M25 Graphene Nanoplatelets as the starting material using an improved Hummers Method [141]. In brief, M25 (1g) was added to a solution of phosphoric acid and sulfuric acid in a 1:9 volume ratio (13.3 mL: 120 mL) and chilled to 5 ^{o}C. Potassium permanganate (6g) was added slowly to the stirring solution, heated to 50 ^{o}C, and stirred overnight. Once the reaction was done, the solution took on a light purple coloration. The solution was poured over 400 mL ice and 3mL hydrogen peroxide, at which point there was a color change to bright yellow to indicate the end of the reaction. The solution was centrifuged at 4000 rpm for 4hrs followed by sequential washing and centrifuging with HCL, H_2O, and ethanol. The material was dried in a vacuum oven at 60 ^{o}C overnight to obtain GO powder.

4.3.3 Preparation of PS Microspheres

PS microspheres were prepared in a three-necked flask equipped with a condenser by dispersion polymerization under a nitrogen environment [142]. Purified styrene monomers (20.0g) with AIBN (0.3g) as a radical initiator were dissolved in ethanol (60.0g) containing PVP (2.0g) as a stabilizer. Nitrogen bubbling was applied for 20 minutes to clear the system of any residual oxygen. The mixture was stirred for 12 hrs at a temperature of 70 ^{o}C. The dispersed PS

microsphere were washed with ethanol and water to remove unreacted styrene and residual PVP. The remaining PS microspheres were dispersed in water.

4.3.4 Preparation of PS/rGO Composites

Typically, a solution of GO (1mg/mL) in water was prepared under sonication for 1hr. A specific amount of PS microspheres was added to the GO solution, sonicated for an additional 5 minutes and stirred for an additional 30 min. The brown-grey coagulation that forms indicates the binding of rGO to the PS microspheres. Ascorbic acid (AA) was added in a 1:100 rGO:AA ratio by weight and the temperature was raised to 95 ^{o}C and maintained for 4 hrs. The rGO/PS complex was vacuum filtered and washed with water until a pH of 7 was achieved. Collected material was dried overnight in a vacuum oven at 70 ^{o}C to remove any residual solvent. rGO/PS pucks were created by hot pressing at 120 ^{o}C and 10 MPA for 20 minutes.

4.3.5 Preparation of PS/rGO/CF Composites

rGO/PS solution was prepared as mentioned earlier. After reduction, Cobalt Nitrate Hexahadyrate and Iron Chloride Nonahydrate were added to the rGO/PS solution in a molar ratio of 1:2 Co^{2+}: Fe^{3+}. The solution was stirred for another 30 minutes and then the temperature was raised to 90 ^{o}C. At this point NaOH was added until pH 10 was reached and the temperature was maintained for 2 hrs to allow for nucleation and growth of cobalt ferrite nanoparticles on the rGO surface. After cooling to room temperature, the rGO/PS/CF material was collected using centrifugation followed by vacuum filtration and washing with ethanol and water to remove any unreacted metal salts. The leftover powder was dried overnight at 70 ^{o}C to remove any residual solvent. Composite pucks were hot pressed at 120 ^{o}C and 10 MPA for 20 minutes.

4.3.6. Characterization of PS/rGO and PS/rGO/CF Composites

The morphology of the composite before and after hot pressing was examined by SEM (JEOL 1500) under an acceleration voltage of 20 kV. FTIR spectra of composite powders were measured with a JASCO 4100 spectrometer in the range of 4000-400 cm^{-1} under transmittance mode. XPS measurements were carried out using monochromatic Al-Kα radiation to determine the change in oxygen content. Structural investigation upon the addition of CF were measured by XRD with Cu Kα radiation (λ = 0.15418 nm) under a voltage of 40 kV and a current of 20 mA using a Rigaku Miniflex 600. The volume conductivity of composite pucks was measured by a

four-probe method using a Cascade Microtech probe station. B-H curves were measured using a Lakeshore Cryotechnic 7400 vibrating sample magnetometer (VSM). The complex permeability and permittivity of materials were measured using a Keysight PNA-X Network Analyzer N5245A in the frequency range of 4-12 GHz. The samples were formed into toroidal shaped samples with an outer diameter of 7.0 mm and an inner diameter of 3.04 mm using a Tormach PCNC 1440 milling machine.

4.4 Results and Discussion

4.4.1. Validation of PS/rGO Composites With a Segregated Structure.

The material was characterized at different stages of the composite fabrication. Figure 4.2 shows SEM images of as synthesized PS microspheres. Owing to the PVP stabilizer, the microspheres do not agglomerate readily. The as synthesized microspheres are fairly polydisperese in size with dimateres ranging from 1-6 μm. As synthesized spheres easily form colloidal white dispersion in water under mild sonication and stirring.

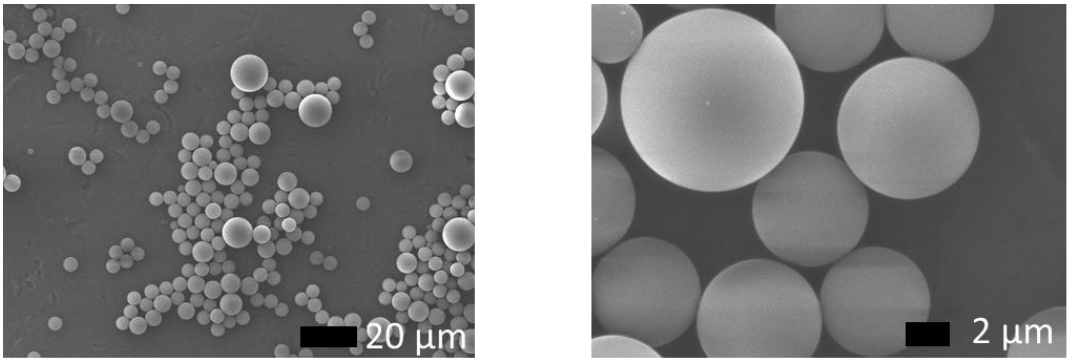

Fig 4.2 - SEM images depicting as synthesized PS microspheres. They display polydispersity with sizes ranging from 1-6 μm.

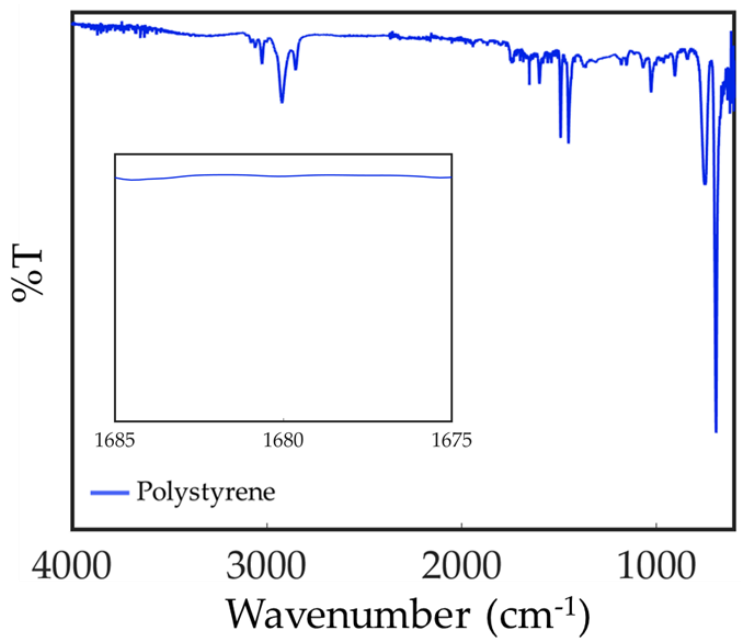

Fig 4.3 – FTIR spectra of as synthesized PS microspheres. Inset shows the dissapearance of the C=C styrene vinyl peak at 1683 cm^{-1} indictaing successful polymerization.

Successful synthesis of PS microspheres was also confirmed through FTIR spectroscopy as shown in Figure 4.3. This spectra displays all the characteristic peaks of styrene, but to confirm successful polymerization, we look for the dissapearance of the peak at 1683 cm^{-1} (Fig 4.3 inset) which corresponds to the C=C styrene vinyl peak [143]. The adsorption of GO sheets on PS microspheres is demonstrated by the SEM images in Figure 4.4 of PS/GO microspheres collected from the suspension made by dispersing GO sheets and PVP-grafted PS microspheres in water. Many PS microspheres are coated by GO sheets with some GO sheets between adjacent but separate microspheres. The chemical reduction by AA does not seem to affect this coating nature as indicated by Fig 4.4c.This is not surprising since the PVP mediated interatcion between GO and PS spheres should not be interrupted during mild chemical reduction [142]. Fig 4.4b shows FTIR transmittance data for PS, PS/GO, and PS/RGO. The change in the peak after reduction ~3500 indicates successful restoration of the sp^2 network in rGO. Further evidence for successful reduction is given by XPS data shown in Fig 4.4d that clealy shows a decrease in the O peak, but does not eliminate it completely [144].

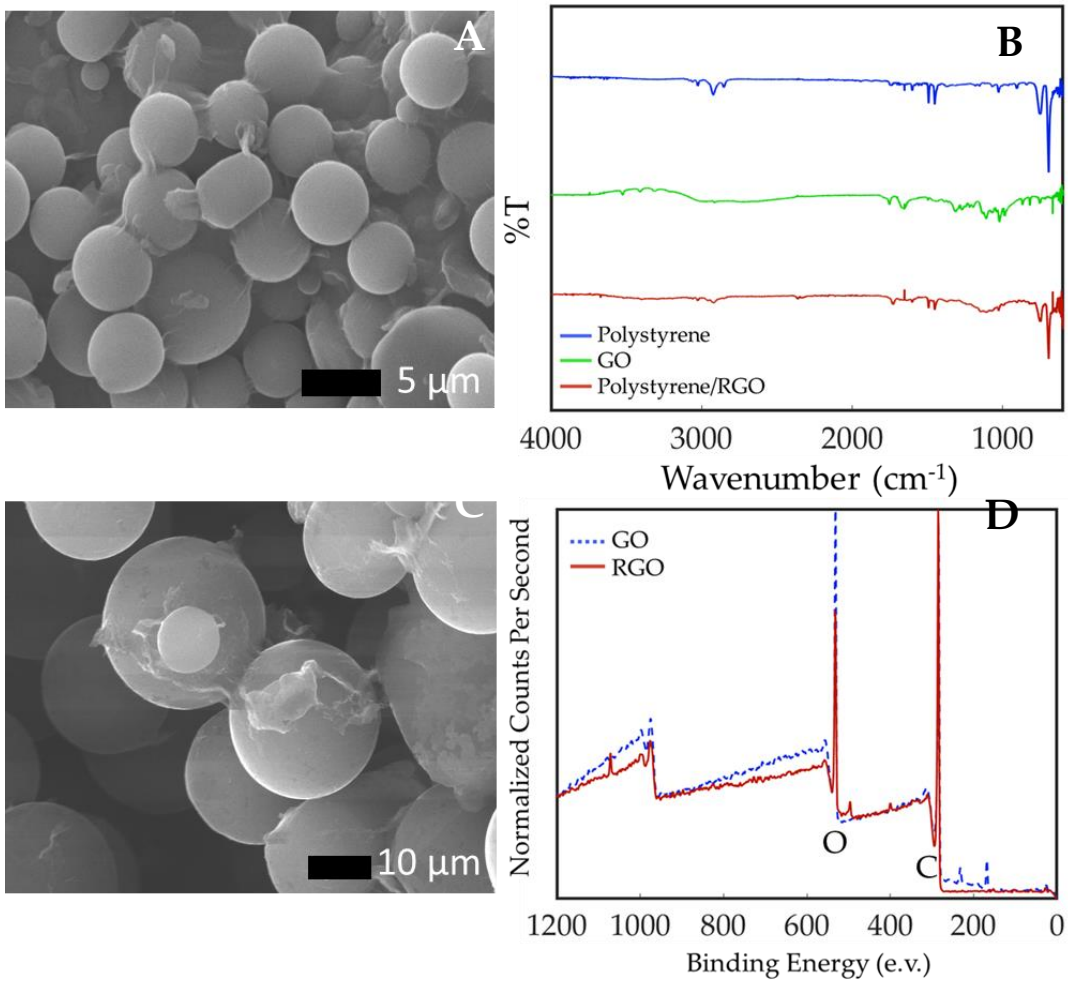

Fig 4.4 – (A) SEM image of GO coated PS microspheres. The wrinkled morphology indicates bonding between the microspheres and the GO sheets. (B) FTIR of PS, GO, and PS/rGO powders. (C) SEM image of rGO coated PS microspheres. (D) XPS spectra of GO and rGO powders indicating an adequate degree of GO reduction by AA has occurred.

After hot pressing we ultimately aim to generate a segregated network with conductive filler mterial occupying the space between polymer domains. Figure 4.5 shows SEM images of a cross section of 0.75 vol% rGO/PS composite after hot pressing. After hot pressing the composites present with a three-dimensional percolated microcellular structure with a polymer cell size of 2-5 µm.

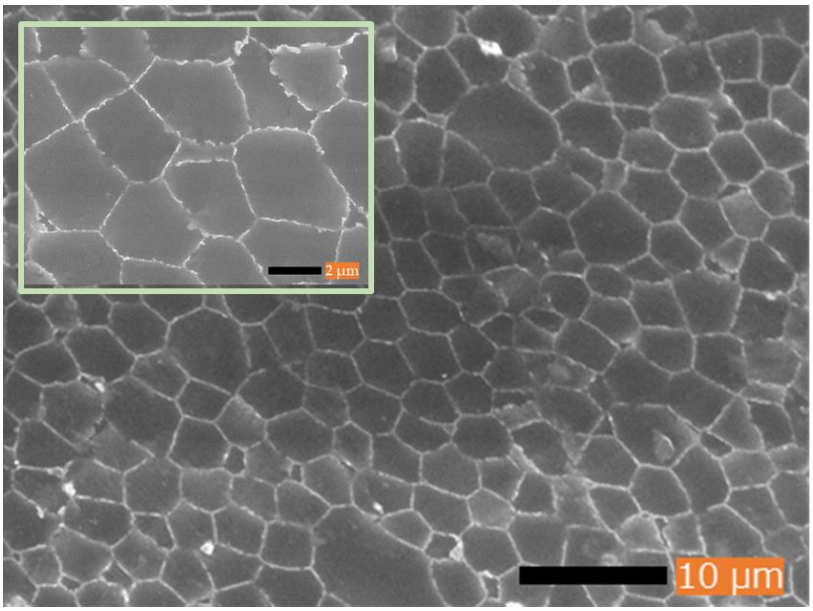

Fig 4.5 – SEM image of cross scetion of a 0.75 vol% PS/rGO composite. The formation of a segregated structure is indicated byt the dark polymer domains surrounded by bright concentrations of rGO filler in the interfaces.

The formaiton of conductive rGO networks is also confirmed through the conductivity of the PS/rGO composites. Figure 4.6 shows the electrical conductivity and percolation behavior as a function of rGO volume fraction. Even though this material does not exhibit a homogenouse microstructure, the clasical percolation theory still applies since we are still defining a critical volume fraction for an insulator/conductor transitions [145]. We use the classical peroclation power law to fit the eletrical data according to:

(4.1) $\sigma = \sigma_0(\phi - \phi_c)^t$

where σ is the conductivity of the composite, σ_0 is the proportionality constant related to the intrinsic conductivty of rGO filler, ϕ is the filler volume fraction, ϕ_c is the critical filler volume for percolation, and *t* is the crictical exponent that represents the dimensionality of the conductive network [146]. According to the fitting, our composites exhibit a percolation threshold of 0.04 vol%. In reality, the real percolation threshold is probably much higher since we label specimens by their loading pre-compression. A representative volume element of a segregated structure should contain a much larger volume fraction of filler material than the recorded percolation threshold. However, it is standard to practice to report percolation threshold of segregated structures using classical percolation theory and the pre-compression loading. We found our critical exponent to be 2.5, which is indicative of a three-dimensional conductive

network [147]. At a filler loading of 1 vol% the conductivity is 3.26 S/m. The conductivity increases to 6.13 S/m for 2 vol%, and 32.4 S/m for 4 vol%, which is adequate for many applications.

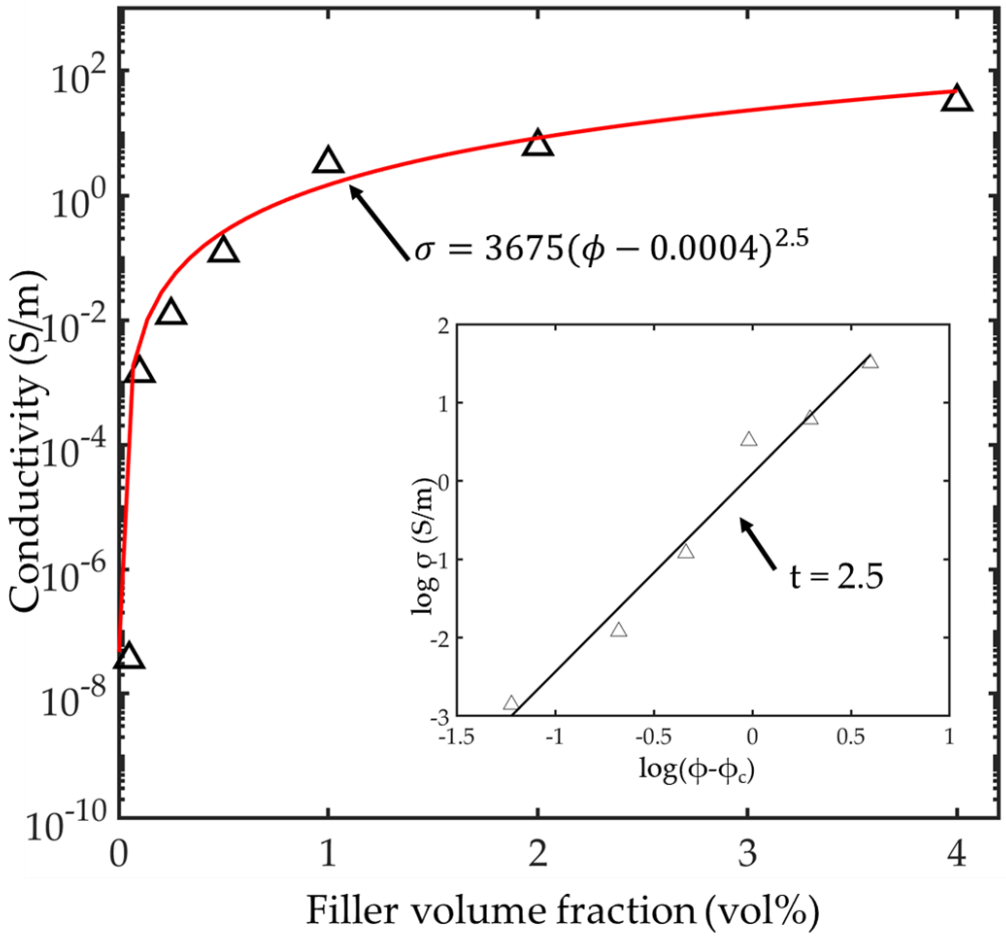

Fig 4.6 – The electrical conductivities of PS/rGO composites as a function of volume fraction. The inset shows a plot log(σ) vs. (ϕ-ϕ_c) for calculation of *t*.

4.4.2. Validation of PS/rGO/CF Composites with a Segregated Structure

During CF nanoparticle formation, metal salts associate with the surface of the rGO platelets and the addition of NaOH leads to direct co-precipitation [148]. Figure 4.7 shows SEM images of as synthesized PS/GO/CF and PS/rGO/CF complexes prior to hot pressing. The bumpy morphology on the surface of the PS spheres clearly indicates formation of nanoparticles on their surface when compared to the morphologies seen in non-functionalized PS/GO

materials. The nanoparticles are evenly distributed, but there does appear to be evidence of minor agglomeration in certain locations. The purity of CF nanoparticles was confirmed through XRD and EDX mapping.

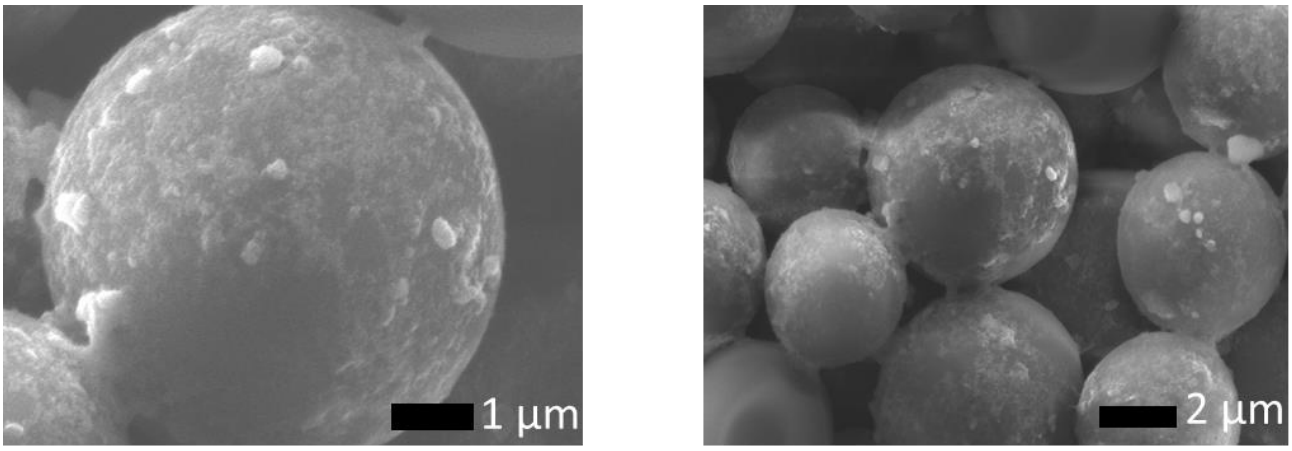

Fig 4.7 – SEM images of PS/GO/CF (left) and PS/rGO/CF (right). Wrinkled morphology connecting PS sphere indicates that GO/rGO wrapping is maintained. Bumpy morphology on top of GO/rGO is evidence of CF functionalization.

Figure 4.8 shows typical XRD spectra for bare PS microspheres, rGO/CF filler material, as well as the fully assembled PS/rGO/CF. The spectra for polystyrene shows a broad peak centered around 20º, which is in agreement with reported values for amorphous polystyrene materials [149]. The spectra for rGO/CF displays characteristic peaks for inverse spinel CF nanoparticles with peaks at 31º and 35.3º corresponding to the (220) and (311) planes [150]. The spectra for the fully assembled filler material display a large broad peak corresponding to PS. Because it is the most prevalent material in the filler, the signal for the other components is uncharacteristically weak. However, a close-up, shown in Figure 4.8., of the area between 30º to 40º reveals the presence of the strong (311) peak corresponding to CF nanoparticles.

Figure 4.9 shows SEM, back scattered electron (BSE), and EDX mapping for a cross section of a 1 vol% PS/rGO/CF composite after hot pressing. The SED image in Fig 4.8a. shows a similar morphology to Fig 4.5 corresponding to successful formation of a segregated network. A BSE image shown in Fig 4.8b the presence of bright areas corresponding to the interfacial areas of the composite, indicating the presence of heavy elements. EDX mapping shown in Fig 4.8c-e show that the elements in the interfaces correspond to Fe and Co. From these data we can

see that the hot pressing does not degrade the functionalization of the rGO surface and rGO/CF hybrid fillers remain present in the segregated network.

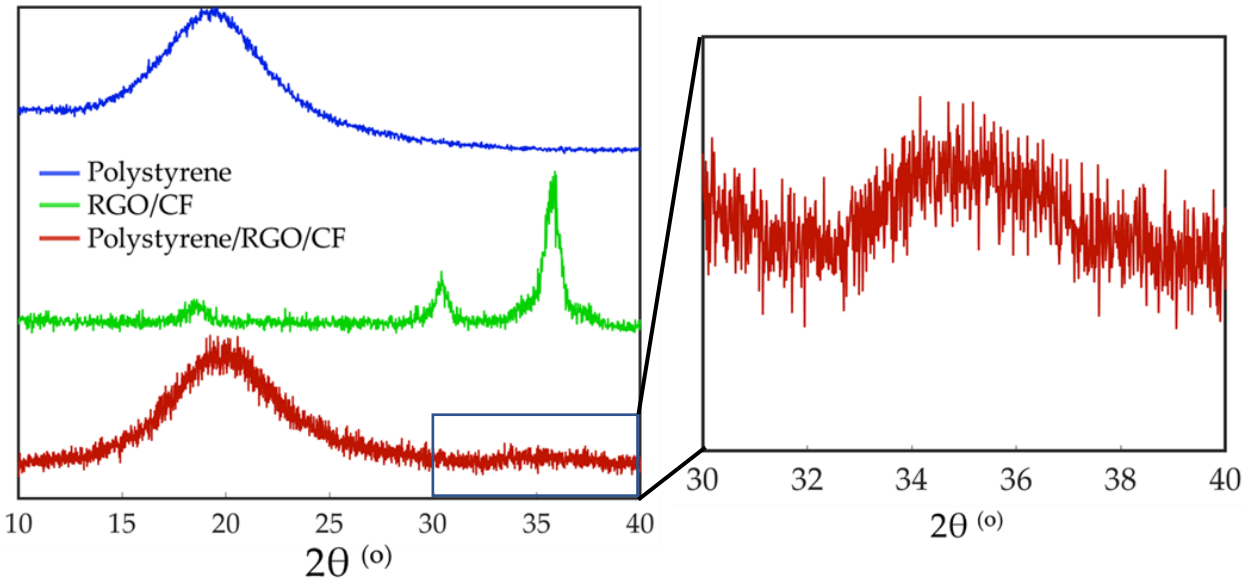

Fig 4.8 – XRD spectra of PS, rGO/CF, and fully assembled PS/rGO/CF composite material. The PS spectra displays a large amorphous peak. The rGO/CF spectra display characteristic peaks for CF at 31° and 35.3°. The spectrum for PS/rGO/CF displays a large amorphous peak showing the presence of PS. The CF peak at 35.3° can be seen in the close up of the PS/rGO/CF spectra.

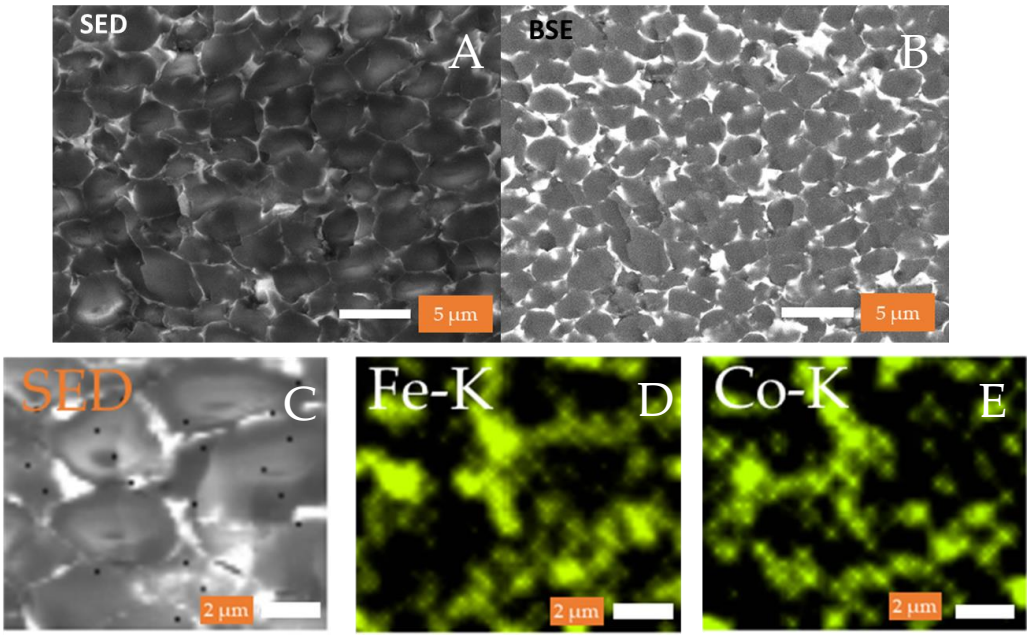

Fig 4.9 – SEM images of 1 vol% PS/rGO/CF cross sections viewed using (A) secondary electron detector as well as (B) BSE. Both images show the presence of a segregated network morphology. (C-E) Display EDS mapping of an interfacial area. The concentrated presence of Co and Fe atoms can be seen in the interfacial areas.

To study the effects of the loading of magnetic nanoparticles on the electrical and magnetic properties of segregated composites, four different composites of varying rGO and CF loading were prepared. The naming conventions, respective loadings, and as measured electrical conductivities are shown in Table 4.1. As compared to nonfunctionalized PS/rGO composites, PS/rGO/CF samples display lower electrical conductivities. This is most likely caused by insulating CF nanoparticles partially blocking conductive pathways provided by rGO [151]. By controlling the CF loading, we can effectively control the conductivity of segregated composites.

Table 4.1 – Naming convention and measured conductivity for PS/rGO/CF Composites

Sample Name	rGO Loading	rGO:CF Ratio	Conductivity (S/m)
2V12	2 vol%	1:2	3.38
2V21	2 vol%	2:1	2.21
Pt5V12	0.5 vol%	1:2	0.40
Pt5V21	0.5 vol%	2:1	0.014

The magnetic performance of the PS/rGO/CF composites was investigated by monitoring their magnetization with an applied magnetic field ranging from -600 to 600 Oe at room temperature. For comparison, the magnetization was normalized based on the total weight of the composite powder. As shown in Figure 4.10 the M_s of these materials is low, with the highest value corresponding to -0.55 memu/g for 2V21. It is interesting to note that 2V12 sample has a M_s that is approximately half that of 2V21. This is evidence that the correct relative concentrations of CF have been incorporated into the composite powder. The Pt521 and Pt512 samples display highly diamagnetic behavior. This is an indication that there is not enough CF to content to compete with the highly nonmagnetic PS matrix and rGO filler. For all of the composite materials, the moments are severely decreased as compared to similar systems [152–154].

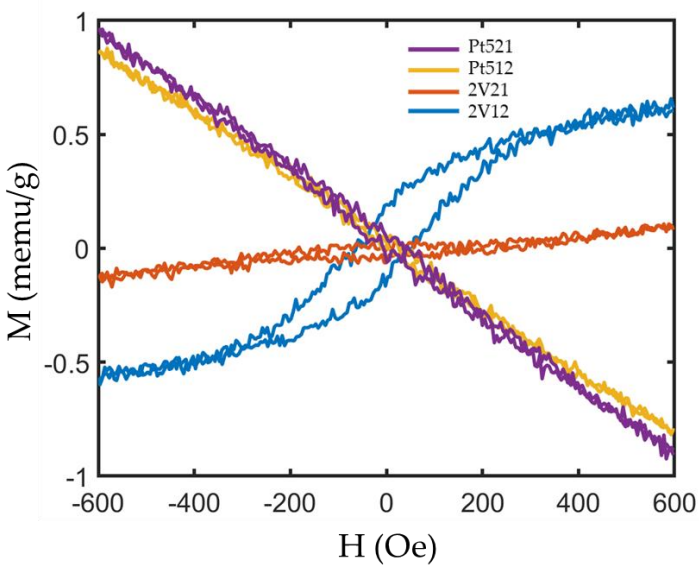

Fig 4.10 – Magnetic response of PS/rGO/CF composites with varied rGO and CF loadings. The composites with a loading of 0.5 vol% rGO display purely diamagnetic responses.

4.4.3 Electromagnetic Properties of PS/rGO and PS/rGO/CF Composites

Upon formation of the segregated structure, PS/rGO composites were measured on the VNA for investigation of the electromagnetic parameters in the 4-12 GHz range. The complex permittivity of the composites is plotted in Fig 4.11. There is an obvious increase in the values for the real and imaginary permittivity as the rGO loading moves past the conductive percolation threshold, which is in accordance with similar materials [155]. In this frequency range, the real and imaginary permittivity also exhibit a gradual decreasing trend as the frequency increases. This frequency dependence can be explained by Maxwell-Wagner Sillars polarization which occurs when there is an accumulation of charge carriers at any interface between materials. Charges on the rGO surface accumulate and lead to frequency sensitivity in the dielectric constant [156].

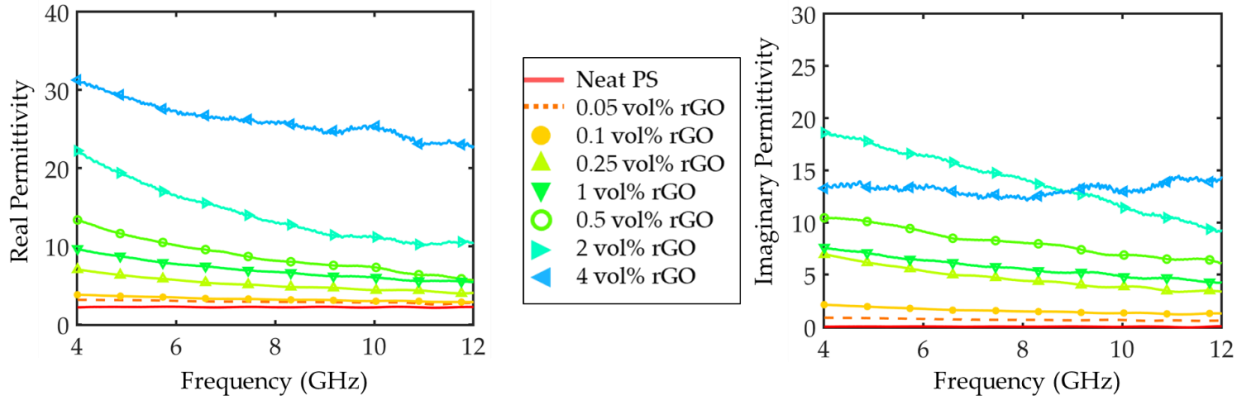

Fig 4.11 – Frequency dependent complex permittivity of PS/rGO composites with different rGO contents. Real permittivity is shown on the left and imaginary permittivity is shown on the right.

In addition to testing the PS/rGO samples, the complex electromagnetic properties of PS/rGO/CF composites were also investigated. Fig 4.12 shows the frequency dependence for the complex permeability and complex permittivity for PS/rGO/CF composites with 0.5 vol% rGO loading (A-D) and 2 vol% rGO loading (E-H). For both rGO loadings, it was found that the real permittivity decreases over the entire frequency range upon the addition of CF nanoparticles. This is most likely due to interruption of conductive network formation. As expected, the imaginary part of the permittivity decreased as CF loading increased. This is in accordance with Debye theory, which shows that the imaginary part of the permittivity decreases as conductivity decreases [157].

For the PS/rGO/CF composites with an rGO loading of 0.5 vol%, there is minimal change in the permeability. This is most likely due to the actual amount of CF present not enough to have an impact. This is also in line with the diamagnetic behavior for these composites shown in figure 4.9. As the rGO loading increases to 2vol%, and the CF loading increases, we begin to observe measurable changes in the complex permeability. As the CF content increases, the real permeability decreases, but the imaginary permeability increases.

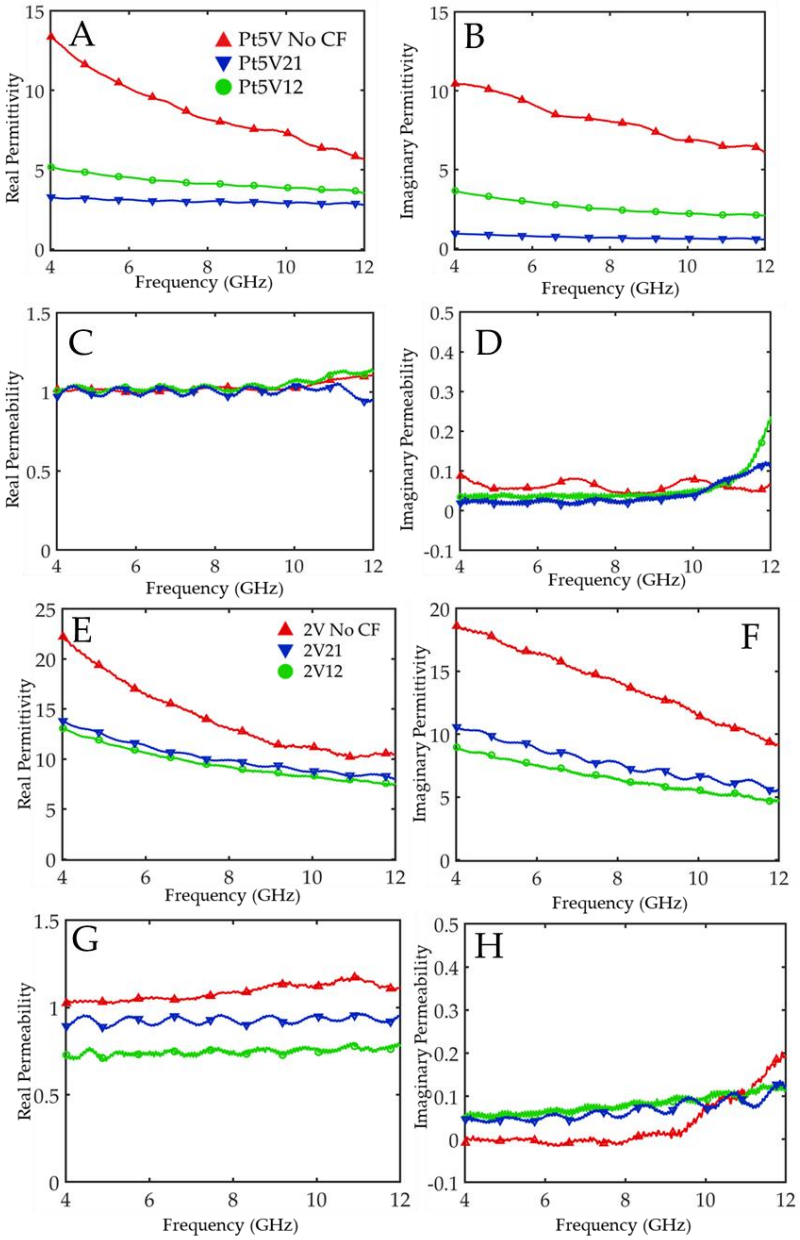

Fig 4.12 – Frequency dependent electromagnetic properties of PS/rGO/CF composites with 0.5 vol% rGO loading (A-D) and 2 vol% rGO loading (E-H).

4.4.4. EMI Shielding Properties of PS/rGO and PS/rGO/CF Composites

Figure 4.13 shows the variation of EMI SE over the range of 4-12 GHz for 4 mm thick PS/rGO segregated composites. There is an increase in EMI SE with concentration, except for 0.5 vol% PS/rGO. The maximum achieved EMI SE was 21.6 dB for the 4 vol% PS/rGO sample. It is interesting to note that the difference in measured SE is much smaller than the orders of magnitude difference observed in conductivity for the same samples (fig 4.6)

To better understand the shielding mechanisms of PS/rGO composites, the frequency dependent power fraction balance for PS/rGO composites as a function of rGO loading is shown in Figure 4.14. Like the PLA composites described in chapter 3, the neat polymer composites display almost no absorbed power, and a small fraction of reflected power that comes from slight changes in impedance. As the rGO loading increases, the transmitted power fraction decreases to almost zero over the entire frequency range at a loading of 4 vol% rGO. This is in direct to contrast to other conductive polymer systems which demonstrate increased reflected power balance as the filler content increases. It has been reported that the cell-like configuration of the PS domains surrounded by a dense layer of rGO can entrap incoming EM waves. Once an incident EM wave enters one of these PS cell domains, the wave will be scattered or experience many absorption events upon interaction with the conductive cell walls [158]. With correct impedance matching, a large portion of the EM wave can penetrate the material and be subject to these phenomena.

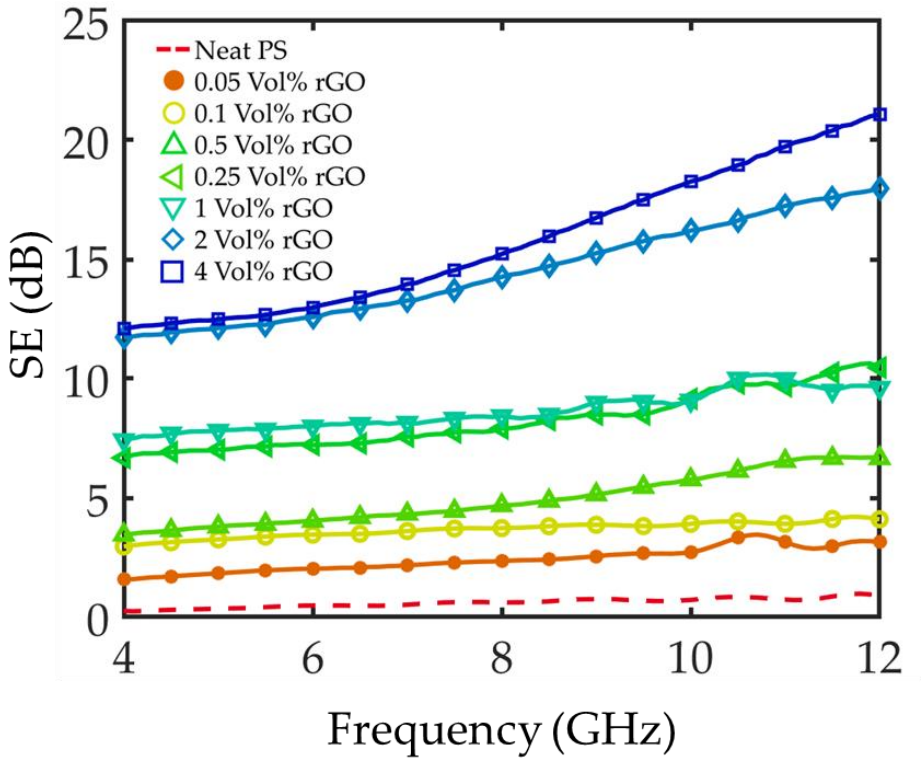

Fig 4.13 –Frequency dependent EMI SE for PS/rGO composites without CF nanoparticles. There is a general increase in SE as the rGO loading increases.

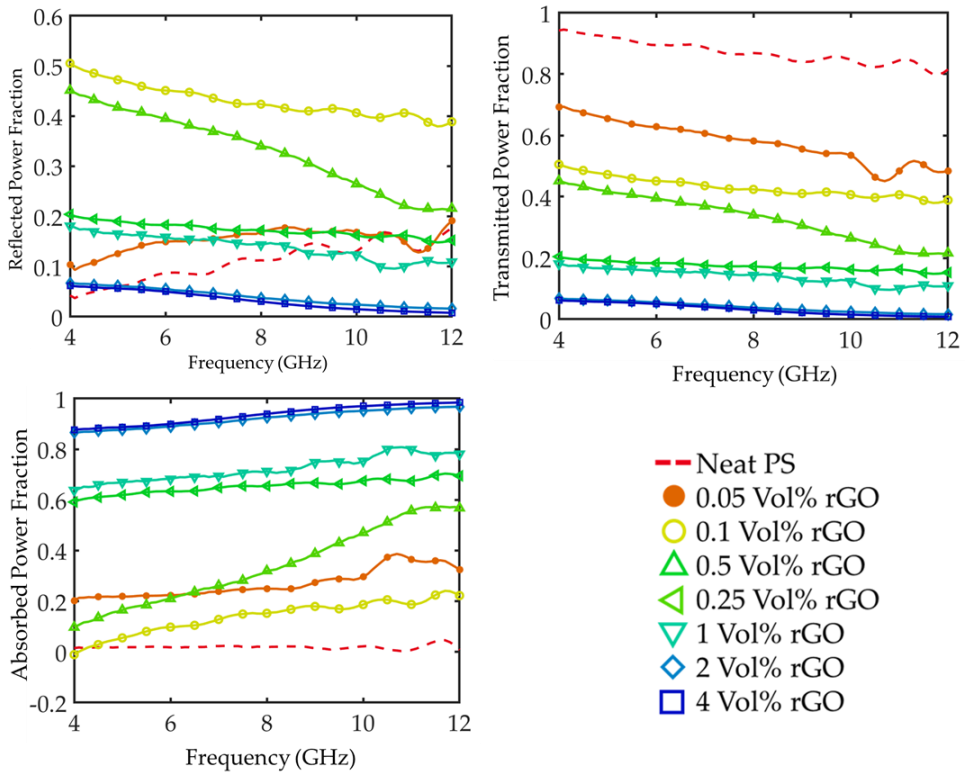

Fig 4.14 – The fraction of incident power that is (a) reflected (b) transmitted (c) and absorbed for PS/rGO segregated structure composite as a function of rGO loading

It is worth noting that even at 0.05 vol%, the transmitted power dropped by ~20%. The reflected power fraction and absorbed power fraction display nearly opposite behaviors at filler loadings of 0.1 vol% and higher. For 0.1 vol%, the reflected power fraction is between 50% at 4 GHz and 40% at 12 GHz and the absorbed power fraction is between 0% and 20% over the entire frequency range. As the loading increases, there is a gradual decrease in the reflected power fraction and a gradual increase in the absorbed power fraction. At a loading of 4 vol%. the reflected power fraction is nearly zero over the entire frequency range and the absorbed power fraction is nearly 100% over the entire frequency range.

Figure 4.15 shows the EMI SE for 4mm thick PS/rGO/CF composites measured over 4-12 GHz. Shown on this figure for comparison are the SE for 2 vol% and 0.5 vol% PS/rGO without CF. For the samples with a 0.5 vol% rGO loading, there is minimal frequency dependence over the measured range. For Pt5V21, there is a depression in EMI SE and a maximum of 3.2 dB is achieved as compared to 7.5 dB for Pt5V12 and 7.9 dB for Pt5V without CF. Based on their hysteresis curves (fig 4.9), the inclusion of CF nanoparticles in these samples

does not have a significant impact on the overall magnetic properties. Instead they serve to decrease the conductivity (and subsequently electric loss) and lower the SE. This is clear from the fact that the Pt5V21 has a much lower SE than the Pt5V12 sample.

For the samples with 2vol % rGO, there are more significant changes that occur upon the addition of CF. As compared to the 2V No CF sample, the 2V12 sample has lower Se over the entire frequency range. Like the Pt5V12 and Pt5V21 materials, there is not enough CF content to contribute in a positive way to SE. For increased CF content in the 2V21 sample, there can be seen an enhancement in SE over the entire frequency range, reaching a maximum of 25 dB, which is higher than even that of the 4 vol% PS/rGO. This suggests that the addition of magnetic nanoparticles can contribute positively to SE if the concentration is high enough to make up for losses in conductivity and electric loss.

To understand the shielding mechanisms PS/rGO/CF composites, the power fraction balance is shown in Figure 4.16. For PS/rGO/CF composites with a 0.5 vol% loading, there is a dramatic increase in the absorbed power fraction to almost 80% over the entire frequency range as the CF ratio increases. However, the SE of these composites is so low that it is difficult to claim definite improvement in their ability as absorbers. For the composites with 2 vol% rGO loading, as the CF loading ratio increases, there is a demonstrated increase in the reflected power fraction and a decrease in the absorbed power fraction as compared to the PS/rGO composites without CF loading. Although the main SE mechanism is still absorption over the entire frequency range, increases in reflection are most likely cause by a change in impedance mismatch at the front face due to the addition of CF.

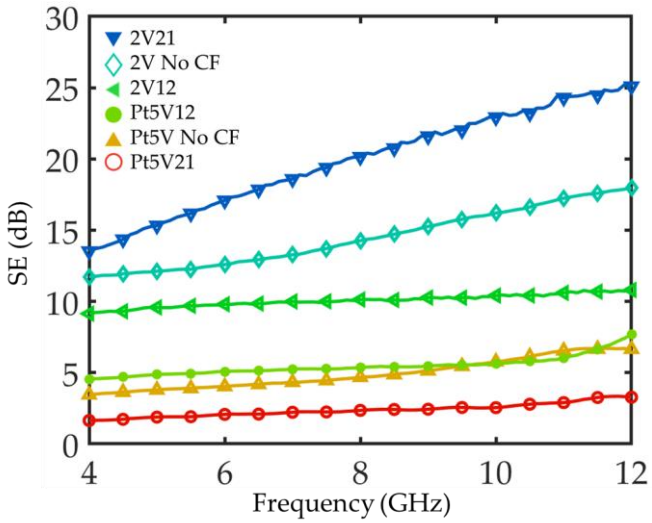

Fig 4.15 - Frequency dependent EMI SE for PS/rGO/CF composite samples with a thickness of 4mm. All samples measured under normal incidence over the entire frequency range.

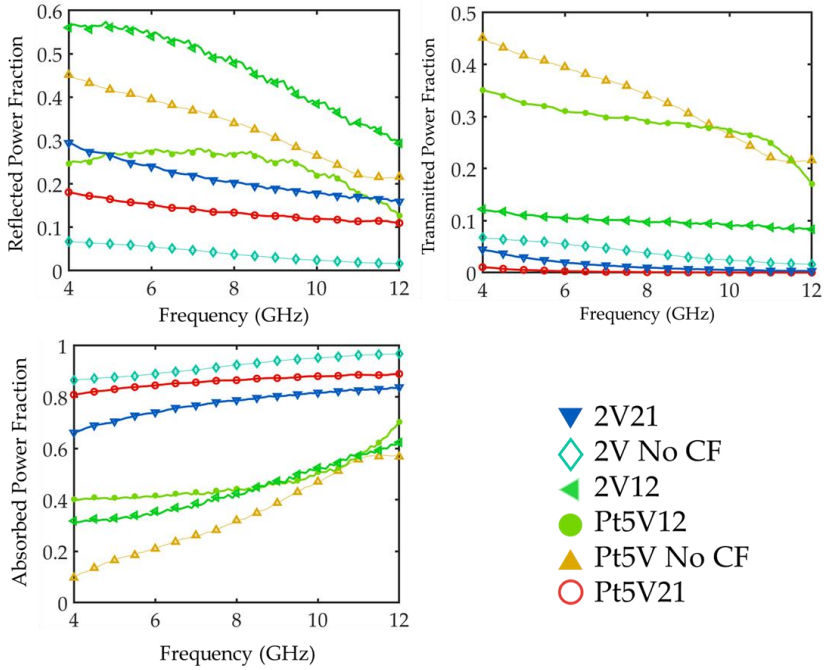

Fig 4.16 - The fraction of incident power that is (a) reflected (b) transmitted (c) and absorbed for PS/rGO/CF segregated structure composite as a function of rGO and CF loading,

Shown in Table 4.2 are reported Max SE for a variety of polymer composite systems with a magnetic component, as well as the reported magnetic component loading in wt%. For our best performing material, we report higher SE at similar filler loadings, and can even achieve comparable SE as composites with almost double the amount of magnetic material, as can be

seen for the PE/PEO/GO/MWCNT/Ni composite. Our approach requires processing optimization but is on par with other material in the literature.

Table 4.2 - SE properties of previously reported solid composites with a magnetic component

Material	Magnetic Loading (wt%)	Max SE (dB)	Ref
PANI/rGO/Fe_3O_4	10	7.5	[151]
PMMA/rGO/ Fe_3O_4	2	30	[159]
PE/PEO/GO/MWCNT/Ni	19	27	[49]
PS/CNF/CNT	0	22	[12]
PEI/ rGO/ Fe_3O_4	5	9.2	[89]
2V21 (PS/rGO/CF)	8	25	This Work

4.4.5 RL of PS/rGO and PS/rGO/CF Composites With and Without Spherical Pores

In addition to looking at the air-backed SE of PS/rGO composites, we also looked at their RL and the effects of adding pores on RL to see if we could further improve the absorbing properties of segregated structure composites. Shown in Table 4.3 is the maximum simulated RL for 4mm thick solid plaques composed of PS/rGO composites with various loadings of rGO. Neat PS is nearly 100% transmissive to incoming EM radiation and has a RL of almost zero across the entire frequency range. For materials with a high conductivity (2 and 4 vol% PS/rGO), there is a large impedance mismatch resulting in low RL. For 0.5 vol% however, there is a large RL of nearly -46 dB.

In the context of the previous chapters it is worth performing a brief investigation of the effect that spherical pores can have on the RL of segregated structure composites. To this end a parametric study was conducted, simulating a single spherical pore in the center of a 4 mm thick slab and varying the pore diameter from 1.6 to 3.2 mm. Table 4.3 shows the max RL of a non-porous slab as well as the max RL without pores for the same material. For the PS/rGO/CF materials, this limited study did not reveal geometries with exemplary RL, but for all the samples, there was some improvement in RL upon addition of a pore. This information provides us with the confidence that given more time and optimization steps, an ideal geometry could be found that takes advantage of the inherent segregated network in these materials.

Table 4.3-Max RL of 4mm thick PS/rGO and PS/rGO/CF composites with and without a single spherical pore

Material	Max RL without Pore (dB)	Max RL with Pore (dB)	Pore Diameter (mm)
PS	-1>	N/A	N/A
0.25 vol% PS/rGO	-13	-34	3.2
0.5 vol% PS/rGO	-46	-38	2.1
1 vol% PS/rGO	-11	-19	3.2
2 vol% PS/rGO	-6	-8	3.2
4 vol% PS/rGO	-6	-11	3.2
2V212	-8	-14	3.2
2V21	-8	-9	3.2
Pt5V12	-10	-31	1.6
Pt5V21	-8	-9	1.6

4.5 Conclusions

To work around problems concerning high filler loading and dispersibility, we investigated PS/rGO composites with a segregated structure as potential EMI shielding materials. It was found that PS/rGO composites exhibit remarkably low percolation thresholds and the conductivity can be easily controlled through the filler loading. These materials also demonstrated reasonable SE at low loadings. We also systematically explored the development of novel PS/rGO/CF systems with various loadings of rGO and CF. We found that at low rGO/CF loadings, the addition of CF interfered with the formation of conductive networking, and decreased overall SE. At higher loadings of rGO/CF it was found that the addition of CF also interfered with the formation of conductive networking, but the higher loading of CF had a positive effect on SE due to its magnetic contribution. Furthermore, we demonstrated that the RL of PS/rGO and PS/rGO can be enhanced with a periodic porous morphology. With this initial

material exploration, we have shown that CPCs with segregated structures are a viable option for EMI shields. Further optimization of material processing and conditions will be necessary for future EMI shield development.

CHAPTER 5

Conclusions and Future Work

Due to a high dependence of polymer composite foam morphology on initial foaming conditions (temperature, time, pressure, matrix, filler, etc..), it is hard to predict the final morphology of foamed composites without performing a large DOE. Difficulty in predicting final morphologies in these materials also leads to difficulty in predicting the final EMI shielding properties of these materials in any reliable fashion. This thesis sought to develop tools for the quick and reliable development of "foam-inspired" metamaterial- polymer composites with enhanced EMI shielding abilities.

Understanding that the EMI shielding properties of a material system are governed by its intrinsic electromagnetic parameters, we began analyses using the measured properties of highly conductive PLA based filament as well as the literature values for a hybrid composite system that contained a magnetic component. Using these electromagnetic parameters, we evaluated the addition of a single air-filled pore into the center of a unit cell with periodicity in the X and Y direction and a finite thickness in the Z direction. For a highly conductive material, there were minor improvements in absorptive ability; a highly conductive front face meant that most incident power was reflected. For a material with lower permittivity and a magnetic component, there was significant enhancement in absorption upon addition of a single pore. We found that there was a dependence on the distance between pores as well as the volume of the pore. This was interpreted as realization of resonant networks as confirmed by plotting the electric field distribution. An advantage of this approach over conventional foaming techniques is that we can quickly explore the effects of other geometric modifications.

Having established the prospect of enhancing EMI absorption through the addition of periodically placed pores, it was necessary to validate a modeling approach using measurements on plaques to confirm the validity of the approach. To achieve this goal, we fabricated a

PLA/xGNP composite system and analyzed its electromagnetic properties. We investigated the effect of filler aspect ratio on the electromagnetic parameters and found that there was a positive relationship between filler aspect ratio and complex permittivity for a fixed weight percentage. It was also observed that there was no significant change in the permeability upon the addition of nonmagnetic graphitic fillers. It was also observed that higher aspect ratio filler materials had higher conductivities, which agreed with classic percolation theory.

For the higher aspect ratio filler materials, we fabricated composite plaques with cylindrical pores placed in a periodic fashion and measured the resulting scattering parameters. When these same configurations were simulated, we found that there was agreement between experimental and simulation data in the trends as well as location of maxima/minima for scattering parameters. For this material system we observed that additions of pores degraded SE but demonstrated marked improvement in RL. This is a promising result since many applications will necessitate PEC backing.

An issue that limited our ability to move forward with xGNP composites was the lack of homogenous dispersion. Several techniques exist for qualitatively assessing the state of xGNP dispersion including zeta potential monitoring [160], rheological measurements [161,162], and Raman spectroscopy [163]. There exist other measurement methods, but they require extensive and laborious measurement (TEM) or are extremely limited in the in the concentrations that can be analyzed, as is the case with Dynamic Light Scattering. For future work that uses conventional dispersion methods, it will be important to confirm the existence of the degree of filler dispersion.

Due to concerns surrounding high filler loading, limited dispersion ability, and a desire to explore the effect of a magnetic component addition, the we explored PS/rGO segregated network polymer composites with and without CF nanoparticles. It was observed that successful fabrication of a segregated network could be achieved, which led to a remarkably low percolation threshold and high conductivities. For non-magnetically modified composites, the SE increased with increasing filler loading. Furthermore, the main shielding mechanism became increasingly dominated by absorption as the filler loading increased. Upon addition of magnetic CF nanoparticles, it was found that for low loadings of rGO, the CF addition had a minimal effect on overall SE. As the rGO and subsequently CF content increased, we observed a slight

increase in SE for a 2:1 CF: rGO ratio as compared to non-modified rGO. However, for this increased loading, the shielding mechanism began to shift from absorption to reflection. It will be necessary to engage in further material optimization to generate PS/rGO/CF composites with the correct rGO: CF ratio to achieve absorption dominated high SE.

While segregated composites are an interesting approach to EMI shielding, they have mechanical limitations that may prohibit their use in certain applications. The formation of segregated structures inevitably gives rise to agglomeration of filler material and prevention of diffusion between polymer granules which can significantly reduce the toughness and ductility of these materials [164]. To mitigate some of these problems, it has been suggested that using a secondary polymer as a carrier for conductive filler material can ease interfacial flaws between the main polymer matrix and filler [165]. Expanding on the work done in chapter 4, it would be useful to investigate the effects of using a secondary polymer as a bridging agent in PS/rGO/CF composites.

Based on the findings in this thesis, it appears that it is possible to design polymer composites with optimized geometries for enhanced microwave absorption applications. The ability to design structures based solely on intrinsic electromagnetic properties seems particularly useful for electronics industries that deal heavily in communication and wireless signaling. It is worth noting that many of the geometric studies in this thesis were composed solely of serial parametric scans over a limited set of geometric variables. This type of approach did yield geometries with improved properties, but the goal of a simulation guided approach is to accurately and rapidly explore a continuous result space while controlling a multitude of geometric and material parameters.

Geometric optimization of microwave absorbers has been done in the past but is often limited to evaluating thicknesses and multilayer combinations of different materials [166–169]. To perform an in-depth optimization, it will likely involve a two-step procedure. Due to the very large parameter space that can potentially be explored, the first step should be a Monte Carlo simulation that evaluates many points sampled at random from the parameter space and the most promising results will be carried over to a gradient-free or gradient based optimization for the second step. By choosing several points at random from the first, we can avoid arriving at local

minima in the second optimization. Ongoing work by members of my lab is currently looking into streamlining this approach and developing optimization workflows.

As mentioned in chapter 2, a geometric optimization that can successfully explore a large parameter space that includes pore shape, size, location, etc. could ultimately yield geometries that require unique fabrication approaches. One of the most promising approaches appears to be 3D printing of polymeric composites. In the current literature a variety of materials have been printed using fused deposition modeling including PU/PLA/GO [170], silicon rubber/CNF [171] and ABS/CB/CNT [34]. There has also been extensive development of conductive polymer composite inks for 3D printing using digital light projection (DLP) [172–174]. DLP is a promising approach, particularly for the printing of porous structures. Mu et al. demonstrated the ability to create complex porous structures using a combination of salt leaching and DLP [175]. These types of approaches often require unique set-ups as well as original ink formulations that can take significant amounts of time to perfect.

In addition to 3D printing, there are also opportunities to create complex porous geometries using mold casting. To move forward with mold casting, it will be necessary to utilize better dispersion methods for the creation of polymer composite materials with lower percolation thresholds and an additional magnetic component as compared to the PLA/xGNP materials in chapter 3. One approach with is to utilize *in-situ* polymerization. This technique can lead to composites with low percolation thresholds due to very strong filler-matrix interactions. The polymer coating, prior to polymerization, also helps to disrupt van-der Waals interactions between neighboring carbonaceous fillers. *In-situ* polymerization can also be done in the absence of solvents that can disrupt magnetic functionalization of fillers. Ultimately, a combination of material optimization and improved geometric optimization will be necessary for the creation of world-class absorbing material

BIBLIOGRAPHY

[1] Kong LB, Li ZW, Liu L, Huang R, Abshinova M, Yang ZH, et al. Recent progress in some composite materials and structures for specific electromagnetic applications. Int Mater Rev 2013;58:203–59. doi:10.1179/1743280412Y.0000000011.

[2] Drewniak J. PCB Design for Real-World EMI Control. Springer Science & Business Media; 2013.

[3] Ramahi O, Brench C. EMI/EMC computational modeling handbook. Springer Science & Business Media; 2012.

[4] Qin F, Brosseau C. A review and analysis of microwave absorption in polymer composites filled with carbonaceous particles. J Appl Phys 2012;111. doi:10.1063/1.3688435.

[5] Guo Z, Park S, Hahn HT, Wei S, Moldovan M, Karki AB, et al. Magnetic and electromagnetic evaluation of the magnetic nanoparticle filled polyurethane nanocomposites. J. Appl. Phys., vol. 101, American Institute of Physics; 2007, p. 09M511. doi:10.1063/1.2711074.

[6] Al-Saleh MH, Sundararaj U. Electromagnetic interference shielding mechanisms of CNT/polymer composites. Carbon N Y 2009;47:1738–46. doi:10.1016/j.carbon.2009.02.030.

[7] Casey KF. Electromagnetic shielding behavior of wire-mesh screens. IEEE Trans Electromagn Compat 1988;30:298–306.

[8] Yim Y-J, Park S-J. Electromagnetic interference shielding effectiveness of high-density polyethylene composites reinforced with multi-walled carbon nanotubese. J Ind Eng Chem 2015;21:155–7.

[9] Yousefi N, Sun X, Lin X, Shen X, Jia J, Zhang B, et al. Highly aligned graphene/polymer nanocomposites with excellent dielectric properties for high-performance electromagnetic interference shielding. Adv Mater 2014;26:5480–7. doi:10.1002/adma.201305293.

[10] Jagatheesan K, Ramasamy A, Das A, Basu A. Electromagnetic shielding behaviour of conductive filler composites and conductive fabrics ??? A review. Indian J Fibre Text Res 2014;39:329–42.

[11] Pawar SP, Biswas S, Kar GP, Bose S. High frequency millimetre wave absorbers derived from polymeric nanocomposites. Polym (United Kingdom) 2015;84:398–419. doi:10.1016/j.polymer.2016.01.010.

[12] Yang Y, Gupta MC, Dudley KL. Towards cost-efficient EMI shielding materials using carbon nanostructure-based nanocomposites. Nanotechnology 2007;18:345701. doi:10.1088/0957-4484/18/34/345701.

[13] Klüppel M, Möwes MM, Lang A, Plagge J, Wunde M, Fleck F, et al. Characterization and Application of Graphene Nanoplatelets in Elastomers 2016:1–42. doi:10.1007/12_2016_1.

[14] Zaldivar RJ, Adams P, Kim HI, Nokes JP. Mechanical enhancement of graphite nanoplatelet composites: Effect of matrix material on the atmospheric plasma-treated GnP reinforcement. J Compos Mater 2016;50:219–29. doi:10.1177/0021998315573285.

[15] Biswas S, Fukushima H, Drzal LT. Mechanical and electrical property enhancement in exfoliated graphene nanoplatelet/liquid crystalline polymer nanocomposites. Compos Part A Appl Sci Manuf 2011;42:371–5. doi:10.1016/j.compositesa.2010.12.006.

[16] Jin Y, Yu F, Kuppa VK. Three-fold improvement in the performance of all-polymer photovoltaic devices with graphene. Mater Lett 2015;156:161–4. doi:10.1016/j.matlet.2015.04.103.

[17] Barrau S, Demont P, Peigney A, Laurent C, Lacabanne C. Dc and ac conductivity of carbon nanotubes-polyepoxy composites. Macromolecules 2003;36:5187–94. doi:10.1021/ma021263b.

[18] Luo J, Ma Q, Gu H, Zheng Y, Liu X. Three-dimensional graphene-polyaniline hybrid hollow spheres by layer-by-layer assembly for application in supercapacitor. Electrochim Acta 2015;173:184–92. doi:10.1016/j.electacta.2015.05.053.

[19] Sun Y chun, Cui W yu, Li J long, Wu J zhu. In-situ growth strategy to fabrication of MWCNTs/Fe3O4with controllable interface polarization intensity and wide band electromagnetic absorption performance. J Alloys Compd 2019;770:67–75. doi:10.1016/j.jallcom.2018.08.106.

[20] Kim D., Zhang Y, Voit W, Rao K., Kehr J, Bjelke B, et al. Superparamagnetic iron oxide nanoparticles for bio-medical applications. Scr Mater 2001;44:1713–7. doi:10.1016/S1359-6462(01)00870-3.

[21] Gedler G, Antunes M, Velasco JI. Viscoelastic properties of polycarbonate-graphene nanoplatelets nanocomposite foams 2016. doi:10.1016/j.compositesb.2016.03.032.

[22] Wang H, Zhang H, Zhao W, Zhang W, Chen G. SCIENCE AND Preparation of polymer / oriented graphite nanosheet composite by electric field-inducement 2008;68:238–43. doi:10.1016/j.compscitech.2007.04.012.

[23] Li Q, Guo Y, Li W, Qiu S, Zhu C, Wei X, et al. Ultrahigh Thermal Conductivity of Assembled Aligned Multilayer Graphene/Epoxy Composite 2014.

[24] Wei J, Atif R, Vo T, Inam F. Graphene Nanoplatelets in Epoxy System : Dispersion , Reaggregation , and Mechanical Properties of Nanocomposites 2015;2015.

[25] Song Y, Yu J, Yu L, Alam FE, Dai W, Li C, et al. Enhancing the thermal , electrical , and mechanical properties of silicone rubber by addition of graphene nanoplatelets. JMADE 2015;88:950–7. doi:10.1016/j.matdes.2015.09.064.

[26] Mehrali M, Sadeghinezhad E, Latibari ST, Kazi SN, Mehrali M, Zubir MNBM, et al. Investigation of thermal conductivity and rheological properties of nanofluids containing graphene nanoplatelets. Nanoscale Res Lett 2014;9:1–12. doi:10.1186/1556-276X-9-15.

[27] Wang F, Drzal LT. Mechanical properties and thermal conductivity of graphene nanoplatelet / epoxy composites 2015:1082–93. doi:10.1007/s10853-014-8665-6.

[28] Sengupta R, Bhattacharya M, Bandyopadhyay S, Bhowmick AK. A review on the mechanical and electrical properties of graphite and modified graphite reinforced polymer composites. Prog Polym Sci 2011;36:638–70. doi:10.1016/j.progpolymsci.2010.11.003.

[29] Chandrasekaran S, Seidel C, Schulte K. Preparation and characterization of graphite nano-platelet (GNP)/epoxy nano-composite: Mechanical, electrical and thermal properties. Eur Polym J 2013;49:3878–88. doi:10.1016/j.eurpolymj.2013.10.008.

[30] Lin Z-I, Lou C-W, Pan Y-J, Hsieh C-T, Huang C-L, Huang C-H, et al. The effects of MWCNT length on the mechanical, crystallization and electromagnetic interference shielding effectiveness of PP/MWCNT composites. J Polym Res 2017;24:32. doi:10.1007/s10965-016-1121-3.

[31] Zhang XF, Dong XL, Huang H, Lv B, Lei JP, Choi CJ. Microstructure and microwave absorption properties of carbon-coated iron nanocapsules. J Phys D Appl Phys 2007;40:5383–7. doi:10.1088/0022-3727/40/17/056.

[32] Thomassin J-M, Jérôme R, Detrembleur C. Polymer/carbon nanotube composites for electromagnetic interference reduction. Phys Prop Appl Polym Nanocomposites 2010:563–87. doi:10.1533/9780857090249.3.563.

[33] Huang C-L, Lou C-W, Liu C-F, Huang C-H, Song X-M, Lin J-H. Polypropylene/Graphene and Polypropylene/Carbon Fiber Conductive Composites: Mechanical, Crystallization and Electromagnetic Properties. Appl Sci 2015;5:1196–210. doi:10.3390/app5041196.

[34] Schmitz DP, Ecco LG, Dul S, Pereira ECL, Soares BG, Barra GMO, et al. Electromagnetic interference shielding effectiveness of ABS carbon-based composites manufactured via fused deposition modelling. Mater Today Commun 2018;15:70–80. doi:10.1016/j.mtcomm.2018.02.034.

[35] Yang W, Song J, Chen J, Wen Y, Sun Y. Synergistic Conductivity and Electromagnetic Interference Shielding Effectiveness of Epoxy/Carbon Fiber and Epoxy/Carbon Black Composites via Mixing with Bamboo Charcoal. BioResources 2017;12:1288–99. doi:10.15376/biores.12.1.1288-1299.

[36] Al-Saleh MH, Saadeh WH, Sundararaj U. EMI shielding effectiveness of carbon based nanostructured polymeric materials: A comparative study. Carbon N Y 2013;60:146–56. doi:10.1016/j.carbon.2013.04.008.

[37] Agnihotri N, Chakrabarti K, De A. Highly efficient electromagnetic interference shielding using graphite nanoplatelet/poly(3,4-ethylenedioxythiophene)-poly(styrenesulfonate) composites with enhanced thermal conductivity. RSC Adv 2015;5:43765–71. doi:10.1039/C4RA15674A.

[38] R. Mohan R, Varma SJ, Sankaran J. Impressive electromagnetic shielding effects exhibited by highly ordered, micrometer thick polyaniline films. Appl Phys Lett 2016;108:154101. doi:10.1063/1.4945791.

[39] Huang CY, Wu JY, Tsao KY, Lin CL, Chang CP, Tsai CS, et al. The manufacture and investigation of multi-walled carbon nanotube/polypyrrole/EVA nano-polymeric composites for electromagnetic interference shielding. Thin Solid Films, vol. 519, 2011, p. 4765–73. doi:10.1016/j.tsf.2011.01.031.

[40] Naishadham K. Shielding effectiveness of conductive polymers. IEEE Trans Electromagn Compat 1992;34:47–50. doi:10.1109/15.121666.

[41] Song W-L, Fan L-Z, Cao M-S, Lu M-M, Wang C-Y, Wang J, et al. Facile fabrication of ultrathin graphene papers for effective electromagnetic shielding. J Mater Chem C Mater Opt Electron Devices 2014;2:5057–64. doi:10.1039/c4tc00517a.

[42] Chizari K, Arjmand M, Liu Z, Sundararaj U, Therriault D. Three-dimensional printing of highly conductive polymer nanocomposites for EMI shielding applications. Mater Today Commun 2017;11:112–8. doi:10.1016/j.mtcomm.2017.02.006.

[43] Sharif F, Arjmand M, Moud AA, Sundararaj U, Roberts EPL. Segregated Hybrid Poly(methyl methacrylate)/Graphene/Magnetite Nanocomposites for Electromagnetic Interference Shielding. ACS Appl Mater Interfaces 2017;9:14171–9. doi:10.1021/acsami.6b13986.

[44] Chen Y, Zhang H Bin, Huang Y, Jiang Y, Zheng WG, Yu ZZ. Magnetic and electrically conductive epoxy/graphene/carbonyl iron nanocomposites for efficient electromagnetic interference shielding. Compos Sci Technol 2015;118:178–85. doi:10.1016/j.compscitech.2015.08.023.

[45] Chen Y, Wang Y, Zhang H Bin, Li X, Gui CX, Yu ZZ. Enhanced electromagnetic interference shielding efficiency of polystyrene/graphene composites with magnetic Fe3O4 nanoparticles. Carbon N Y 2015;82:67–76. doi:10.1016/j.carbon.2014.10.031.

[46] Song WL, Guan XT, Fan LZ, Cao WQ, Wang CY, Zhao QL, et al. Magnetic and conductive graphene papers toward thin layers of effective electromagnetic shielding. J Mater Chem A 2015;3:2097–107. doi:10.1039/c4ta05939e.

[47] Song W-L, Guan X-T, Fan L-Z, Cao W-Q, Zhao Q-L, Wang C-Y, et al. Tuning broadband microwave absorption via highly conductive Fe3O4/graphene heterostructural nanofillers. Mater Res Bull 2015;72:316–23. doi:10.1016/j.materresbull.2015.07.028.

[48] Petcharoen K, Sirivat A. Dual responses of magnetite-graphene hybrid in polyurethane under magnetic and electric stimuli. Sensors Actuators, A Phys 2016;251:26–34. doi:10.1016/j.sna.2016.09.041.

[49] Mural PKS, Pawar SP, Jayanthi S, Madras G, Sood AK, Bose S. Engineering Nanostructures by Decorating

Magnetic Nanoparticles onto Graphene Oxide Sheets to Shield Electromagnetic Radiations. ACS Appl Mater Interfaces 2015;7:16266–78. doi:10.1021/acsami.5b02703.

[50] Baaziz W, Truong-Phuoc L, Duong-Viet C, Melinte G, Janowska I, Papaefthimiou V, et al. Few layer graphene decorated with homogeneous magnetic Fe3O4 nanoparticles with tunable covering densities. J Mater Chem A 2014;2:2690. doi:10.1039/c3ta14512c.

[51] Bregar VB, Properties AM. 2-Advantages of ferromagnetic nanoparticle composites in microwave absorbers.pdf 2004;40:1679–84.

[52] Dormann JL, Lucari F, Tronc E, Prené P, Jolivet JP, Fiorani D, et al. Thermal variation of the relaxation time of the magnetic moment of-Fe 2 O 3 nanoparticles with interparticle interactions of various strengths. 1996.

[53] Batlle X, Labarta A. Finite-size effects in fine particles: magnetic and transport properties. vol. 35. 2002.

[54] Lv L, Liu J, Liang C, Gu J, Liu H, Liu H, et al. An Overview of Electrically Conductive Polymer Nanocomposites toward Electromagnetic Interference Shielding. Eng Sci 2018:26–42. doi:10.30919/es8d615.

[55] Pardoen T, Bailly C, Thomassin J, Je C, Huynen I, Detrembleur C. Polymer / carbon based composites as electromagnetic interference (EMI) shielding materials. Mater Sci Eng R 2013;74:211–32. doi:10.1016/j.mser.2013.06.001.

[56] Song WL, Cao MS, Lu MM, Bi S, Wang CY, Liu J, et al. Flexible graphene/polymer composite films in sandwich structures for effective electromagnetic interference shielding. Carbon N Y 2014;66:67–76. doi:10.1016/j.carbon.2013.08.043.

[57] Lin J-H, Lin Z-I, Pan Y-J, Huang C-L, Chen C-K, Lou C-W. Polymer composites made of multi-walled carbon nanotubes and graphene nano-sheets: Effects of sandwich structures on their electromagnetic interference shielding effectiveness 2016. doi:10.1016/j.compositesb.2015.11.014.

[58] Mittal V. Polymer Nanocomposite Foams. vol. 1990. 2013. doi:10.1201/b15572.

[59] Gedler G, Antunes M, Velasco JI, Ozisik R. Electromagnetic shielding effectiveness of polycarbonate/graphene nanocomposite foams processed in 2-steps with supercritical carbon dioxide. Mater Lett 2015;160:41–4. doi:10.1016/j.matlet.2015.07.070.

[60] Sauceau M, Fages J, Common A, Nikitine C, Rodier E. New challenges in polymer foaming: A review of extrusion processes assisted by supercritical carbon dioxide. Prog Polym Sci 2011. doi:10.1016/j.progpolymsci.2010.12.004.

[61] Antunes M, Velasco JI. Multifunctional polymer foams with carbon nanoparticles. Prog Polym Sci 2014;39:486–509. doi:10.1016/j.progpolymsci.2013.11.002.

[62] Okolieocha C, Raps D, Subramaniam K, Altst??dt V. Microcellular to nanocellular polymer foams: Progress (2004-2015) and future directions - A review. Eur Polym J 2015;73:500–19. doi:10.1016/j.eurpolymj.2015.11.001.

[63] Tanaka T, Eguchi S, Saitoh H, Taniguchi M, Lloyd DR. Microporous foams of polymer blends of poly(L-lactic acid) and poly(ε-caprolactone). Desalination 2008;234:175–83. doi:10.1016/j.desal.2007.09.084.

[64] Tan L-C, Zhou W-H, Huang Y-L, Chen Y-W. Sequential Structure, Crystallization, and Properties of Biodegradable Poly(ethylene Terephthalate-Co-Ethylene Oxide-Co-Lactide) Copolyester 2014. doi:10.1080/00222348.2014.901870org/10.1080/00222348.2014.901870.

[65] Ling J, Zhai W, Feng W, Shen B, Zhang J, Zheng WG. Facile preparation of lightweight microcellular polyetherimide/graphene composite foams for electromagnetic interference shielding. ACS Appl Mater Interfaces 2013;5:2677–84. doi:10.1021/am303289m.

[66] Shen B., Li Y, Yi D., Zhai W., Wei X., Zheng W. Microcellular graphene foam for improved broadband

electromagnetic interference shielding. Carbon N Y 2016;102:154–60. doi:10.1016/j.carbon.2016.02.040.

[67] Chen Z, Xu C, Ma C, Ren W, Cheng HM. Lightweight and flexible graphene foam composites for high-performance electromagnetic interference shielding. Adv Mater 2013;25:1296–300. doi:10.1002/adma.201204196.

[68] Zhang H Bin, Yan Q, Zheng WG, He Z, Yu ZZ. Tough graphene-polymer microcellular foams for electromagnetic interference shielding. ACS Appl Mater Interfaces 2011;3:918–24. doi:10.1021/am200021v.

[69] M Jacobs LJ, Kemmere MF, F Keurentjes JT. Cutting-edge research for a greener sustainable future Sustainable polymer foaming using carbon dioxide Bhaskar et al. Debromination of flame retardant plastics with microwave irradiation Sustainable polymer foaming using high pressure carbon dioxide: a r 2008;10. doi:10.1039/b801895b.

[70] Matuana LM, Faruk O, Diaz CA. Cell morphology of extrusion foamed poly(lactic acid) using endothermic chemical foaming agent. Bioresour Technol 2009;100:5947–54. doi:10.1016/j.biortech.2009.06.063.

[71] Wu Y, Wang Z, Liu X, Shen X, Zheng Q, Xue Q, et al. Ultralight Graphene Foam/Conductive Polymer Composites for Exceptional Electromagnetic Interference Shielding. ACS Appl Mater Interfaces 2017;9:9059–69. doi:10.1021/acsami.7b01017.

[72] Min Z, Yang H, Chen F, Kuang T. Scale-up production of lightweight high-strength polystyrene/carbonaceous filler composite foams with high-performance electromagnetic interference shielding. Mater Lett 2018;230:157–60. doi:10.1016/j.matlet.2018.07.094.

[73] Chen C, Xi J, Zhou E, Peng L, Chen Z, Gao C. Porous Graphene Microflowers for High-Performance Microwave Absorption. Nano-Micro Lett 2018;10:26. doi:10.1007/s40820-017-0179-8.

[74] Bužarovska A. Preparation and characterization of poly(ε-caprolactone)/ZnO foams for tissue engineering applications. J Mater Sci 2017;52:12067–78. doi:10.1007/s10853-017-1342-9.

[75] Huang J, Lin Y, Yu J, Li D, Du J, Yang B, et al. N-doped foam flame retardant polystyrene derived porous carbon as an efficient scaffold for lithium-selenium battery with long-term cycling performance. Chem Eng J 2018;350:411–8. doi:10.1016/J.CEJ.2018.06.010.

[76] Wang X, Wu P. Melamine foam-supported 3D interconnected boron nitride nanosheets network encapsulated in epoxy to achieve significant thermal conductivity enhancement at an ultralow filler loading. Chem Eng J 2018;348:723–31. doi:10.1016/J.CEJ.2018.04.196.

[77] Zhang Y, Huang Y, Zhang T, Chang H, Xiao P, Chen H, et al. Broadband and tunable high-performance microwave absorption of an ultralight and highly compressible graphene foam. Adv Mater 2015;27:2049–53. doi:10.1002/adma.201405788.

[78] Yang Y, Gupta MC, Dudley KL, Lawrence RW. Novel carbon nanotube - Polystyrene foam composites for electromagnetic interference shielding. Nano Lett 2005;5:2131–4. doi:10.1021/nl051375r.

[79] Thomassin JM, Pagnoulle C, Bednarz L, Huynen I, Jerome R, Detrembleur C. Foams of polycaprolactone/MWNT nanocomposites for efficient EMI reduction. J Mater Chem 2008;18:792–6. doi:10.1039/b709864b.

[80] Yan D-X, Ren P-G, Pang H, Fu Q, Yang M-B, Li Z-M. Efficient electromagnetic interference shielding of lightweight graphene/polystyrene composite. J Mater Chem 2012;22:18772. doi:10.1039/c2jm32692b.

[81] Gedler G, Antunes M, Borca-Tasciuc T, Velasco JI, Ozisik R. Effects of graphene concentration, relative density and cellular morphology on the thermal conductivity of polycarbonate-graphene nanocomposite foams. Eur Polym J 2016;75:190–9. doi:10.1016/j.eurpolymj.2015.12.018.

[82] Wang L, Yang X, Jiang T, Zhang C, He L. Cell morphology, bubbles migration, and flexural properties of non-uniform epoxy foams using chemical foaming agent. J Appl Polym Sci 2014;41175:1–9. doi:10.1002/app.41175.

[83] Soltani Alkuh M, Famili M, Mokhtari Motameni Shirvan M, Moeini M. The relationship between electromagnetic absorption properties and cell structure of poly(methyl methacrylate)/multi-walled carbon nanotube composite foams. Mater Des 2016;100:73–83. doi:10.1016/j.matdes.2016.03.075.

[84] Zhang H, Zhang G, Tang M, Zhou L, Li J, Fan X, et al. Synergistic effect of carbon nanotube and graphene nanoplates on the mechanical, electrical and electromagnetic interference shielding properties of polymer composites and polymer composite foams. Chem Eng J 2018;353:381–93. doi:10.1016/j.cej.2018.07.144.

[85] Mar Bernal M, Pardo-Alonso S, Solórzano E, Lopez-Manchado MÁ, Verdejo R, Rodriguez-Perez MÁ. Effect of carbon nanofillers on flexible polyurethane foaming from a chemical and physical perspective. RSC Adv 2014;4:20761. doi:10.1039/c4ra00116h.

[86] Venkatasubbu GD, Ramakrishnan V, Sasirekha V, Ramasamy S, Kumar J. Influence of particle size on the phonon confinement of TiO_2 nanoparticles. J Exp Nanosci 2014;9:661–8. doi:10.1080/17458080.2012.689018.

[87] Gedler G, Antunes M, Velasco JI. Effects of graphene nanoplatelets on the morphology of polycarbonate-graphene composite foams prepared by supercritical carbon dioxide two-step foaming. J Supercrit Fluids 2015;100:167–74. doi:10.1016/j.supflu.2015.02.005.

[88] Kumar R, Singh AP, Chand M, Pant RP, Kotnala RK, Dhawan SK, et al. Improved microwave absorption in lightweight resin-based carbon foam by decorating with magnetic and dielectric nanoparticles. RSC Adv 2014;4:23476. doi:10.1039/c4ra01731e.

[89] Shen B, Zhai W, Tao M, Ling J, Zheng W. Lightweight, multifunctional polyetherimide/graphene@Fe3O 4 composite foams for shielding of electromagnetic pollution. ACS Appl Mater Interfaces 2013;5:11383–91. doi:10.1021/am4036527.

[90] Gedler G, Antunes M, Velasco JI, Ozisik R. Enhanced electromagnetic interference shielding effectiveness of polycarbonate/graphene nanocomposites foamed via 1-step supercritical carbon dioxide process. Mater Des 2016;90:906–14. doi:10.1016/j.matdes.2015.11.021.

[91] Dhakate SR, Subhedar KM, Singh BP. Polymer nanocomposite foam filled with carbon nanomaterials as an efficient electromagnetic interference shielding material. RSC Adv 2015;5:43036–57. doi:10.1039/C5RA03409D.

[92] Gedler G, Antunes M, Velasco JI. Effects of graphene nanoplatelets on the morphology of polycarbonate-graphene composite foams prepared by supercritical carbon dioxide two-step foaming. J Supercrit Fluids 2015;100:167–74. doi:10.1016/j.supflu.2015.02.005.

[93] Nicolson a. M, Ross GF. Measurement of the Intrinsic Properties of Materials by Time-Domain Techniques. IEEE Trans Instrum Meas 1970;19:377–82. doi:10.1109/TIM.1970.4313932.

[94] Huber E, Mirzaee M, Bjorgaard J, Hoyack M, Noghanian S, Chang I. Dielectric property measurement of PLA. 2016 IEEE Int Conf Electro Inf Technol 2016:0788–92. doi:10.1109/EIT.2016.7535340.

[95] Sarvi A, Sundararaj U. Electrical permittivity and electrical conductivity of multiwall carbon nanotube-polyaniline (MWCNT-PANi) core-shell nanofibers and MWCNT-PANi/ polystyrene composites. Macromol Mater Eng 2014;299:1013–20. doi:10.1002/mame.201300406.

[96] Gupta S, Moayed N Al, Khan U, Obol M, Afsar M. Complex Permittivity and Permeability of Single- and Multi-walled Carbon Nanotubes at High Microwave Frequencies and Quantifying Microwave Absorption *. Transform 2007:1–2.

[97] Li W, Liu Q, Wang L, Zhou Z, Zheng J, Ying Y, et al. Low frequency and broadband metamaterial absorber with cross arrays and a flaked iron powder magnetic composite. AIP Adv 2018;8. doi:10.1063/1.5010821.

[98] Zakiyan SE, Azizi H, Ghasemi I. Effect of cell morphology on electrical properties and electromagnetic interference shielding of graphene-poly(methyl methacrylate) microcellular foams. Compos Sci Technol 2018;157:217–27. doi:10.1016/j.compscitech.2018.02.002.

[99] Gavgani JN, Adelnia H, Zaarei D, Moazzami Gudarzi M. Lightweight flexible polyurethane/reduced ultralarge graphene oxide composite foams for electromagnetic interference shielding. RSC Adv 2016;6:27517–27. doi:10.1039/C5RA25374H.

[100] Kuang T, Chang L, Chen F, Sheng Y, Fu D, Peng X. Facile preparation of lightweight high-strength biodegradable polymer/multi-walled carbon nanotubes nanocomposite foams for electromagnetic interference shielding. Carbon N Y 2016;105:305–13. doi:10.1016/j.carbon.2016.04.052.

[101] Zhang K-L, Zhang J-Y, Hou Z-L, Bi S, Zhao Q-L. Multifunctional broadband microwave absorption of flexible graphene composites. Carbon N Y 2018;141:608–17. doi:10.1016/j.carbon.2018.10.024.

[102] Noh YJ, Joh HI, Yu J, Hwang SH, Lee S, Lee CH, et al. Ultra-high dispersion of graphene in polymer composite via solvent free fabrication and functionalization. Sci Rep 2015;5. doi:10.1038/srep09141.

[103] Weir WB. Automatic Measurement of Complex Dielectric Constant and Permeability. Proc IEEE 1974;62:33–6. doi:10.1109/PROC.1974.9382.

[104] De Paula AL, Rezende MC, Barroso JJ. Modified Nicolson-Ross-Weir (NRW) method to retrieve the constitutive parameters of low-loss materials. SBMO/IEEE MTT-S Int Microw Optoelectron Conf Proc 2011:488–92. doi:10.1109/IMOC.2011.6169293.

[105] Taherian R. Experimental and analytical model for the electrical conductivity of polymer-based nanocomposites. Compos Sci Technol 2016;123:17–31. doi:10.1016/j.compscitech.2015.11.029.

[106] Taipalus R, Harmia T, Zhang M., Friedrich K. The electrical conductivity of carbon-fibre-reinforced polypropylene/polyaniline complex-blends: experimental characterisation and modelling. Compos Sci Technol 2001;61:801–14. doi:10.1016/S0266-3538(00)00183-4.

[107] Ameli A, Jung PU, Park CB. Electrical properties and electromagnetic interference shielding effectiveness of polypropylene/carbon fiber composite foams. Carbon N Y 2013;60:379–91. doi:10.1016/j.carbon.2013.04.050.

[108] Xu W, Wang GS, Yin PG. Designed fabrication of reduced graphene oxides/Ni hybrids for effective electromagnetic absorption and shielding. Carbon N Y 2018;139:759–67. doi:10.1016/j.carbon.2018.07.044.

[109] Cao M, Han C, Wang X, Zhang M, Zhang Y, Shu J, et al. Graphene nanohybrids: Excellent electromagnetic properties for the absorbing and shielding of electromagnetic waves. J Mater Chem C 2018;6:4586–602. doi:10.1039/c7tc05869a.

[110] De Bellis G, Tamburrano A, Dinescu A, Santarelli ML, Sarto MS. Electromagnetic properties of composites containing graphite nanoplatelets at radio frequency. Carbon N Y 2011;49:4291–300. doi:10.1016/j.carbon.2011.06.008.

[111] Bansala T, Joshi M, Mukhopadhyay S, Doong R-A, Chaudhary M. Electrically conducting graphene-based polyurethane nanocomposites for microwave shielding applications in the Ku band. J Mater Sci 2016. doi:10.1007/s10853-016-0449-8.

[112] Anwar Z, Kausar A, Rafique I, Muhammad B. Advances in Epoxy/Graphene Nanoplatelet Composite with Enhanced Physical Properties: A Review. Polym Plast Technol Eng 2015;2559:03602559.2015.1098695. doi:10.1080/03602559.2015.1098695.

[113] Pu N-W, Gong Y-J, Huang S-Y, Ger M-D, Liu Y-M, Wu C-H, et al. Remarkable microwave absorption performance of graphene at a very low loading ratio. Compos Part B Eng 2017;114:395–403. doi:10.1016/j.compositesb.2017.02.016.

[114] Arjmand M, Mahmoodi M, Park S, Sundararaj U. An innovative method to reduce the energy loss of conductive filler/polymer composites for charge storage applications. Compos Sci Technol 2013;78:24–9. doi:10.1016/j.compscitech.2013.01.019.

[115] Yan L, Liu J, Zhao S, Zhang B, Gao Z, Ge H, et al. Coaxial multi-interface hollow Ni-Al2O3-ZnO nanowires tailored by atomic layer deposition for selective-frequency absorptions. Nano Res 2017;10:1595–

607. doi:10.1007/s12274-016-1302-8.

[116] Adohi B, Haidar B, Costa L, Laur V, Brosseau C. Assessing the role of graphene content in the electromagnetic response of graphene polymer nanocomposites. Eur Phys J B 2015;88. doi:10.1140/epjb/e2015-60328-6.

[117] Nasouri K, Shoushtari AM, Mojtahedi MRM. Theoretical and experimental studies on EMI shielding mechanisms of multi-walled carbon nanotubes reinforced high performance composite nanofibers. J Polym Res 2016;23. doi:10.1007/s10965-016-0943-3.

[118] Yang Y, Gupta MC, Dudley KL, Lawrence RW. Conductive carbon nanofiber-polymer foam structures. Adv Mater 2005;17:1999–2003. doi:10.1002/adma.200500615.

[119] Li J, Kim JK. Percolation threshold of conducting polymer composites containing 3D randomly distributed graphite nanoplatelets. Compos Sci Technol 2007;67:2114–20. doi:10.1016/j.compscitech.2006.11.010.

[120] Kashi S, Gupta RK, Baum T, Kao N, Bhattacharya SN. Dielectric properties and electromagnetic interference shielding effectiveness of graphene-based biodegradable nanocomposites. Mater Des 2016;109:68–78. doi:10.1016/j.matdes.2016.07.062.

[121] Dhawan S, Ohlan A, Singh K. Designing of Nano Composites of Conducting Polymers for EMI Shielding. Adv. Nanocomposites - Synth. Charact. Ind. Appl., 2012. doi:10.5772/14752.

[122] Chen LF, Ong CK, Neo CP, Varadan V V., Varadan VK. Measurement and Materials Characterization. 2004. doi:10.1002/0470020466.

[123] Al-Saleh MH. Electrical and electromagnetic interference shielding characteristics of GNP/UHMWPE composites. J Phys D Appl Phys 2016;49:195302. doi:10.1088/0022-3727/49/19/195302.

[124] Shao C, Dai W, Zhang X, Zou Y, Zhang B, Wu Q, et al. Synthesis of core–shell Fe3O4@ppy/graphite nanosheets composites with enhanced microwave absorption performance. Mater Lett 2018;239:136–9. doi:10.1016/j.matlet.2018.12.001.

[125] Ameli A, Jung PU, Park CB. Electrical properties and electromagnetic interference shielding effectiveness of polypropylene/carbon fiber composite foams. Carbon N Y 2013;60:379–91. doi:10.1016/j.carbon.2013.04.050.

[126] Bregman A, Taub A, Michielssen E. Computational design of composite EMI shields through the control of pore morphology. MRS Commun 2018;8:1153–7. doi:10.1557/mrc.2018.171.

[127] Silva AA, Stein R, Campos D, Indrusiak T, Soares BG, Barra GMO. Conducting Materials Based on Epoxy/Graphene Nanoplatelet Composites With Microwave Absorbing Properties: Effect of the Processing Conditions and Ionic Liquid. Front Mater 2019;6. doi:10.3389/fmats.2019.00156.

[128] Chiou YC, Chou HY, Shen MY. Effects of adding graphene nanoplatelets and nanocarbon aerogels to epoxy resins and their carbon fiber composites. Mater Des 2019;178. doi:10.1016/j.matdes.2019.107869.

[129] Atif R, Inam F. Reasons and remedies for the agglomeration of multilayered graphene and carbon nanotubes in polymers. Beilstein J Nanotechnol 2016;7:1174–96. doi:10.3762/bjnano.7.109.

[130] Bao Y, Xu L, Pang H, Yan DX, Chen C, Zhang WQ, et al. Preparation and properties of carbon black/polymer composites with segregated and double-percolated network structures. J Mater Sci 2013;48:4892–8. doi:10.1007/s10853-013-7269-x.

[131] Miriyala SM, Kim YS, Liu L, Grunlan JC. Segregated networks of carbon black in Poly(vinyl acetate) latex: Influence of clay on the electrical and mechanical behavior. Macromol Chem Phys 2008;209:2399–409. doi:10.1002/macp.200800384.

[132] George N, Bipinbal PK, Bhadran B, Mathiazhagan A, Joseph R. Segregated network formation of multiwalled carbon nanotubes in natural rubber through surfactant assisted latex compounding: A novel technique for multifunctional properties. Polymer (Guildf) 2017;112:264–77.

doi:10.1016/j.polymer.2017.01.082.

[133] Li W, Wang M, Huang T, Zhang N, Yang J, Wang Y. Constructing a segregated carbon nanotube network in polyamide-based composites towards high dielectric constant and low loss. Mater Lett 2019. doi:10.1016/j.matlet.2019.03.004.

[134] Li C, Yang Z, Tang Z, Guo B, Tian M, Zhang L. A scalable strategy for constructing three-dimensional segregated graphene network in polymer via hydrothermal self-assembly. Chem Eng J 2019:300–8. doi:10.1016/j.cej.2019.01.142.

[135] Lin Y, Liu S, Peng J, Liu L. Constructing a segregated graphene network in rubber composites towards improved electrically conductive and barrier properties. Compos Sci Technol 2016;131:40–7. doi:10.1016/j.compscitech.2016.05.012.

[136] Gong T, Peng SP, Bao RY, Yang W, Xie BH, Yang MB. Low percolation threshold and balanced electrical and mechanical performances in polypropylene/carbon black composites with a continuous segregated structure. Compos Part B Eng 2016;99:348–57. doi:10.1016/j.compositesb.2016.06.031.

[137] Gao C, Zhang S, Wang F, Wen B, Han C, Ding Y, et al. Graphene networks with low percolation threshold in abs nanocomposites: Selective localization and electrical and rheological properties. ACS Appl Mater Interfaces 2014;6:12252–60. doi:10.1021/am501843s.

[138] Feng D, Xu D, Wang Q, Liu P. Highly stretchable electromagnetic interference (EMI) shielding segregated polyurethane/carbon nanotube composites fabricated by microwave selective sintering. J Mater Chem C 2019;7:7938–46. doi:10.1039/c9tc02311a.

[139] Yu WC, Zhang GQ, Liu YH, Xu L, Yan DX, Huang HD, et al. Selective electromagnetic interference shielding performance and superior mechanical strength of conductive polymer composites with oriented segregated conductive networks. Chem Eng J 2019:556–64. doi:10.1016/j.cej.2019.05.074.

[140] Cui CH, Yan DX, Pang H, Xu X, Jia LC, Li ZM. Formation of a Segregated Electrically Conductive Network Structure in a Low-Melt-Viscosity Polymer for Highly Efficient Electromagnetic Interference Shielding. ACS Sustain Chem Eng 2016;4:4137–45. doi:10.1021/acssuschemeng.6b00526.

[141] Zhu K, Zhang Y, Qiu H, Meng Y, Gao Y, Meng X, et al. Hierarchical Fe 3 O 4 microsphere/reduced graphene oxide composites as a capable anode for lithium-ion batteries with remarkable cycling performance. J Alloys Compd 2016;675:399–406. doi:10.1016/j.jallcom.2016.02.214.

[142] Long G, Tang C, Wong KW, Man C, Fan M, Lau WM, et al. Resolving the dilemma of gaining conductivity but losing environmental friendliness in producing polystyrene/graphene composites via optimizing the matrix-filler structure. Green Chem 2013;15:821–8. doi:10.1039/c3gc37042a.

[143] Hermán V, Takacs H, Duclairoir F, Renault O, Tortai JH, Viala B. Core double-shell cobalt/graphene/polystyrene magnetic nanocomposites synthesized by in situ sonochemical polymerization. RSC Adv 2015;5:51371–81. doi:10.1039/c5ra06847a.

[144] Mohamadi M, Kowsari E, Haddadi-Asl V, Yousefzadeh M. Fabrication, characterization and electromagnetic wave absorption properties of covalently modified reduced graphene oxide based on dinuclear cobalt complex. Compos Part B Eng 2019;162:569–79. doi:10.1016/j.compositesb.2019.01.032.

[145] Pang H, Xu L, Yan DX, Li ZM. Conductive polymer composites with segregated structures. Prog Polym Sci 2014. doi:10.1016/j.progpolymsci.2014.07.007.

[146] Grunlan JC, Mehrabi AR, Bannon MV, Bahr JL. Water-Based Single-Walled-Nanotube-Filled Polymer Composite with an Exceptionally Low Percolation Threshold. Adv Mater 2004;16:150–3. doi:10.1002/adma.200305409.

[147] Jurewicz I, Worajittiphon P, King AAK, Sellin PJ, Keddie JL, Dalton AB. Locking carbon nanotubes in confined lattice geometries - A route to low percolation in conducting composites. J Phys Chem B 2011;115:6395–400. doi:10.1021/jp111998p.

[148] Warner TE. Cobalt Ferrite CoFe2O4 by a Coprecipitation Method. Synth. Prop. Mineral. Important Inorg. Mater., Chichester, UK: John Wiley & Sons, Ltd; 2011, p. 109–23. doi:10.1002/9780470976012.ch8.

[149] Xuemei, H. Hao Y. Fabrication of Polystyrene/Detonation Nanographite Composite Microspheres with the Core/Shell Structure via Pickering Emulsion Polymerization. J Nanomater 2013;2013:8.

[150] Sharifi I, Shokrollahi H, Doroodmand MM, Safi R. Magnetic and structural studies on CoFe 2 O 4 nanoparticles synthesized by co-precipitation, normal micelles and reverse micelles methods. J Magn Magn Mater 2012;324:1854–61. doi:10.1016/j.jmmm.2012.01.015.

[151] Mathew J, Sathishkumar M, Kothurkar NK, Senthilkumar R, Sabarish Narayanan B. Polyaniline/Fe3O4-RGO Nanocomposites for Microwave Absorption. IOP Conf. Ser. Mater. Sci. Eng., vol. 310, 2018. doi:10.1088/1757-899X/310/1/012138.

[152] Bateer B, Zhang J, Zhang H, Zhang X, Wang C, Qi H. Easily Dispersible NiFe2O4/RGO Composite for Microwave Absorption Properties in the X-Band. J Electron Mater 2018;47:292–8. doi:10.1007/s11664-017-5756-6.

[153] Ambikeswari N, Manivannan S. Superior magnetodielectric properties of room temperature synthesized superparamagnetic cobalt ferrite – graphene oxide composite. J Alloys Compd 2018;763:711–8. doi:10.1016/j.jallcom.2018.05.275.

[154] Jiao W, Shioya M, Wang R, Yang F, Hao L, Niu Y, et al. Improving the gas barrier properties of Fe3O4/graphite nanoplatelet reinforced nanocomposites by a low magnetic field induced alignment. Compos Sci Technol 2014;99:124–30. doi:10.1016/j.compscitech.2014.05.022.

[155] Zeraati AS, Arjmand M, Sundararaj U. Silver Nanowire/MnO2 Nanowire Hybrid Polymer Nanocomposites: Materials with High Dielectric Permittivity and Low Dielectric Loss. ACS Appl Mater Interfaces 2017;9:14328–36. doi:10.1021/acsami.6b14948.

[156] He F, Lau S, Chan HL, Fan J. High dielectric permittivity and low percolation threshold in nanocomposites based on poly(vinylidene fluoride) and exfoliated graphite nanoplates. Adv Mater 2009;21:710–5. doi:10.1002/adma.200801758.

[157] Micheli D, Apollo C, Pastore R, Marchetti M. X-Band microwave characterization of carbon-based nanocomposite material, absorption capability comparison and RAS design simulation. Compos Sci Technol 2010;70:400–9. doi:10.1016/j.compscitech.2009.11.015.

[158] Zhang Y, Huang Y, Zhang T, Chang H, Xiao P, Chen H, et al. Broadband and tunable high-performance microwave absorption of an ultralight and highly compressible graphene foam. Adv Mater 2015;27:2049–53. doi:10.1002/adma.201405788.

[159] Sharif F, Arjmand M, Moud AA, Sundararaj U, Roberts EPL. Segregated Hybrid Poly(methyl methacrylate)/Graphene/Magnetite Nanocomposites for Electromagnetic Interference Shielding. ACS Appl Mater Interfaces 2017;9:14171–9. doi:10.1021/acsami.6b13986.

[160] Johnson DW, Dobson BP, Coleman KS. A manufacturing perspective on graphene dispersions. Curr Opin Colloid Interface Sci 2015;20:367–82. doi:10.1016/j.cocis.2015.11.004.

[161] Ivanov E, Velichkova H, Kotsilkova R, Bistarelli S, Cataldo A, Micciulla F, et al. Rheological behavior of graphene/epoxy nanodispersions. Appl Rheol 2017;27. doi:10.3933/APPLRHEOL-27-24469.

[162] Canales J, Fernández M, Peña JJ, Eugenia Muñoz M, Santamaría A. Rheological methods to investigate graphene/amorphous polyamide nanocomposites: Aspect ratio, processing, and crystallization. Polym Eng Sci 2015;55:1142–51. doi:10.1002/pen.23985.

[163] Shojaee SA, Zandiatashbar A, Koratkar N, Lucca DA. Raman spectroscopic imaging of graphene dispersion in polymer composites. Carbon N Y 2013;62:510–3. doi:10.1016/j.carbon.2013.05.068.

[164] Zhang K, Li G-H, Feng L-M, Wang N, Guo J, Sun K, et al. Ultralow percolation threshold and enhanced electromagnetic interference shielding in poly(l -lactide)/multi-walled carbon nanotube nanocomposites

with electrically conductive segregated networks. J Mater Chem C 2017;5:9359–69. doi:10.1039/C7TC02948A.

[165] Pang H, Yan D-X, Bao Y, Chen J-B, Chen C, Li Z-M. Super-tough conducting carbon nanotube/ultrahigh-molecular-weight polyethylene composites with segregated and double-percolated structure † n.d. doi:10.1039/c2jm34793h.

[166] Santhosi BVSRN, Ramji K, Rao NBRM. Optimization of double layered graphene-based microwave absorber in X—band using Pareto genetic algorithm. Mater Res Express 2019;6:105610. doi:10.1088/2053-1591/ab398f.

[167] El-Hakim HA, Mahmoud KR. Design of compact multi-layer microwave absorber for ultra-wide band applications thru shaping and RAM technologies. J Instrum 2019;14:P09006–P09006. doi:10.1088/1748-0221/14/09/p09006.

[168] Padhy S, De A, Debata RR, Meena RS. Design, Characterization, and Optimization of a Multilayer U-type Hexaferrite-Based Broadband Microwave Absorber. IEEE Trans Electromagn Compat 2018;60:1734–42. doi:10.1109/TEMC.2018.2805364.

[169] Singh S, Sinha A, Zunke RH, Kumar A, Singh D. Double layer microwave absorber based on Cu dispersed SiC composites. Adv Powder Technol 2018;29:2019–26. doi:10.1016/j.apt.2018.05.008.

[170] Chen Q, Mangadlao JD, Wallat J, De Leon A, Pokorski JK, Advincula RC. 3D printing biocompatible polyurethane/poly(lactic acid)/graphene oxide nanocomposites: Anisotropic properties. ACS Appl Mater Interfaces 2017;9:4015–23. doi:10.1021/acsami.6b11793.

[171] Huang P, Xia Z, Cui S. 3D printing of carbon fiber-filled conductive silicon rubber. Mater Des 2017. doi:10.1016/j.matdes.2017.12.051.

[172] Lin D, Jin S, Zhang F, Wang C, Wang Y, Zhou C, et al. 3D stereolithography printing of graphene oxide reinforced complex architectures. Nanotechnology 2015;26:434003. doi:10.1088/0957-4484/26/43/434003.

[173] Gonzalez G, Chiappone A, Roppolo I, Fantino E, Bertana V, Perrucci F, et al. Development of 3D printable formulations containing CNT with enhanced electrical properties. Polymer (Guildf) 2017;109:246–53. doi:10.1016/J.POLYMER.2016.12.051.

[174] Mu Q, Wang L, Dunn CK, Kuang X, Duan F, Zhang Z, et al. Digital light processing 3D printing of conductive complex structures. Addit Manuf 2017;18:74–83. doi:10.1016/j.addma.2017.08.011.

[175] Mu X, Bertron T, Dunn C, Qiao H, Wu J, Zhao Z, et al. Porous polymeric materials by 3D printing of photocurable resin. Mater Horiz 2017;4:442–9. doi:10.1039/C7MH00084G.